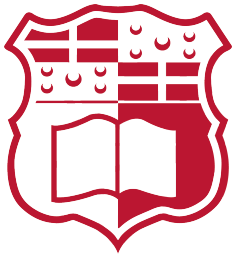

# Design and fabrication of a 3D-printed anthropomorphic heart model to investigate myocardial perfusion


**Miguel Micallef**

Supervised by Mr Sam Agius

Department Medical Physics

Faculty of Health Sciences

University of Malta


**September, 2024**

*A dissertation submitted in partial fulfilment of the requirements for the degree of Master of Science in Medical Physics.*




WWW.UM.EDU.MT

*First edition, October 18, 2024*

*To my family*

*Whose unwavering support along my academic journey made it all possible.*

# Acknowledgements

I would like to express my heartfelt gratitude to the following individuals:

First and foremost, my family. I would not be where I am today without their constant sacrifice, unwavering support, and encouragement.

Secondly, to Karl and Martina. I am immensely grateful for the countless study sessions and memories outside of university which we shared throughout these five years. Our friendship made every challenge easier, and there was never a dull moment thanks to you both.

I also extend my sincere thanks to my partner, Donnah, for the encouragement and unwavering support throughout this year. I am deeply appreciative of all you've done.

My sincere thanks go to Mr. Sam Agius, my project supervisor. Your expertise and guidance have been indispensable in shaping this research, and I am truly grateful for your mentorship.

I would like to acknowledge Katrin, a Master's student in Medical Physics from Germany, whose internship in Malta brought invaluable insights to this study. Her advice and willingness to brainstorm new ideas were instrumental in the progress of this research.

My deepest gratitude goes to Mr. Andre Grech, my A-level physics teacher, for igniting and nurturing my passion for physics. Your mentorship has had a profound and lasting impact on my educational journey.

I am especially grateful to Prof. Carmel J. Caruana, head of the department, for giving me the opportunity to explore the intersection of 3D printing and Medical Physics—your guidance opened new and exciting pathways in my academic pursuits.

My appreciation extends to the Physics Department's Electromagnetics Group, particularly Dr. Julian Debono and Mr. Jonathan Farrugia, for their assistance with the department's 3D printer and their guidance throughout.

L-Università ta' Malta

**FACULTY/INSTITUTE/CENTRE/SCHOOL** Health Science

## DECLARATIONS BY POSTGRADUATE STUDENTS

**(a) Authenticity of Dissertation**

I hereby declare that I am the legitimate author of this Dissertation and that it is my original work.

No portion of this work has been submitted in support of an application for another degree or qualification of this or any other university or institution of higher education.

I hold the University of Malta harmless against any third party claims with regard to copyright violation, breach of confidentiality, defamation and any other third party right infringement.

**(b) Research Code of Practice and Ethics Review Procedures**

I declare that I have abided by the University's Research Ethics Review Procedures. Research Ethics & Data Protection form code FHS-2024-00009.

As a Master's student, as per Regulation 77 of the General Regulations for University Postgraduate Awards 2021, I accept that should my dissertation be awarded a Grade A, it will be made publicly available on the University of Malta Institutional Repository.

# Abstract

**Background**

The demand for custom medical phantoms has driven advancements in 3D-printing within nuclear medicine. This study focused on fabricating a 3D-printed anthropomorphic left ventricular heart phantom for myocardial perfusion imaging (MPI) and evaluating its performance on SPECT and MyoSPECT systems.

**Objectives**

The main objectives were: (1) Identify optimal 3D-printing materials/parameters for a waterproof phantom, (2) Compare MyoSPECT and traditional SPECT imaging, and (3) Assess the best dose protocols for clinical imaging.

**Research Methodology**

A heart phantom was designed using Fused deposition modeling (FDM) with PETG, post-processed for waterproofing, and imaged with SPECT/MyoSPECT at varying doses. Statistical analysis was performed to compare imaging quality.

**Results**

The study found that PETG provided the best results for producing watertight phantoms. The MyoSPECT system outperformed conventional SPECT, particularly at lower doses, showing superior imaging quality and defect detectability. Statistical analysis also revealed differences in certain heart segments

**Conclusions and Recommendations**

This study demonstrates the potential of 3D-printed phantoms in nuclear medicine. MyoSPECT offers better imaging. Recommendations include integrating 3D printing for personalized phantoms and optimizing dose protocols. Future research should explore advanced 3D-printing methods and thoracic phantom simulations.

*Keywords: 3D-printing, 3D-printed phantom, SPECT, MyoSPECT, nuclear medicine, myocardial perfusion imaging (MPI), PETG, fused deposition modelling (FDM)*

# Contents

# List of Figures

# List of Tables

# List of Abbreviations

**MPI** Myocardial Perfusion Imaging . . . . . 3

**NM** Nuclear Medicine . . . . . 1

**CAD** Coronary Artery Disease . . . . . 7

**FDM** Fused deposition modeling . . . . . vi

**SLS** Selective laser sintering . . . . . 3

**SLA** Stereolithography . . . . . 3

**PMT** Photomultiplier Tubes . . . . . 11

**CZT** Cadmium Zinc Telluride . . . . . 15

**BMI** Body Mass Index . . . . . 22

**SPECT/CT** Single Photon Emission Computed Tomography with integrated Computed Tomography . . . . . 11

# 1

# Introduction to the Study

## 1.1 | Introduction

This chapter presents the problem statement, background and context, objectives, scope, summary of research methodology, ethical considerations and relevance of the study

## 1.2 | Problem Statement

Current commercially available phantoms are often expensive, non-anthropomorphic, and do not accurately represent patient anatomy, leading to unrealistic diagnostic and therapeutic decisions. This research aims addressing this issue through the incorporation of 3D-printing techniques. Furthermore, it attempts to address this problem with the cheapest and most accessible 3D-printing technology, the FDM technique. With the main aim of the research being to produce a watertight left ventricular cardiac phantom which requires little to no post-processing techniques. Thus, identifying the methodology required to simply print and use any phantom required in the Nuclear Medicine (NM) department

The other problem this research is trying to address is to qualitatively and quantifiably address the difference between SPECT systems and the cardiac dedicated MyoSPECT system. Through a direct comparison of the two machines when imaging the same phantom with the same level of

activity on both machines.

## 1.3 | Background and Context

Recent advancements in 3D-printing technology have enabled the field of medical physics to create customizable and anatomically accurate phantoms for various applications. A comparative review was conducted between the works of Kiss et al. (2022), Jasmat (2022), and Green and Grice (2022), each of whom developed different variations of 3D-printed cardiac phantoms for use in nuclear medicine. Despite their distinct approaches, these studies laid the groundwork for the current research, with the work of Kiss et al. (2022) being particularly influential. This study used and improved upon Kiss et al. (2022)'s phantom to achieve the objectives set out in this research. Additionally, to develop a waterproof 3D-printed phantom without requiring post-processing, techniques from the 3D printing of microfluidic structures were integrated, as no existing FDM-based 3D-printed phantom met this criterion.

## 1.4 | Objectives of the Study

The study aims to:

1. Determine the best 3D printing materials and parameters to fabricate a phantom suitable for use in the NM department.
2. Utilize 3D printing technology to fabricate a watertight anthropomorphic left ventricle of the heart. This phantom should require little to no post-processing steps and techniques.
3. Collaborate with another 3D printing research group member in the Department of Medical Physics to create an obese thoracic phantom.
4. Compare the 3D printed-phantom with the NM department's current cardiac phantom and with other phantoms found in literature.
5. Evaluate the improvement of the MyoSPECT system over the conventional SPECT

6. Use the phantom to evaluate the optimal dose which sustains the required image quality whilst minimizing radiation exposure to the patient.

## 1.5 | Scope of the Study

The study was delimited to the development and evaluation of 3D-printed cardiac phantoms for nuclear medicine applications, focusing specifically on the imaging capabilities of SPECT and MyoSPECT systems. The research did not extend to the assessment of other imaging modality for Myocardial Perfusion Imaging (MPI). This would have been conducted through the use of the PET/CT.

The study only utilsed FDM based 3D printers. Other 3D printing technologies, such as Stereolithography (SLA) or Selective laser sintering (SLS), which can produce finer details and potentially more precise phantoms, were not explored.

While the study evaluated novel post-processing techniques for waterproofing, it did not explore a full range of post-processing options available. Other methods, such as chemical smoothing or advanced surface treatments, were not considered.

The study was limited to the imaging capabilities of SPECT and MyoSPECT systems in a single institution. Differences in equipment calibration, maintenance, or operator technique across various healthcare facilities could lead to variability in imaging results that were not accounted for in this study.

## 1.6 | Research Methodology

This research employed a mixed-methods approach, combining quantitative analysis of imaging data with qualitative assessments of print quality and usability. The study involved the fabrication and testing of multiple 3D-printed cardiac phantoms using FDM technology. Parameters such

as printing material, layer height, and post-processing techniques were systematically varied to identify optimal conditions for producing waterproof phantoms.

## 1.7 | Ethical Considerations

This study has been approved by the University Research Ethics Committee of the University of Malta. No patient data was used, and all experiments were conducted using phantoms, ensuring that no human subjects were involved. Ethical guidelines were followed to ensure the instructed use of the complex machinery found in the NM department and the safe handling and disposal of radioactive materials during imaging procedures.

## 1.8 | Relevance of the Study

The relevance of the study for the various stakeholders is as follows:

- **Patients** - The development of accurate and customisable 3D-printed phantoms enhances diagnostic accuracy and allows for more personalized treatment planning, leading to better patient outcomes and safety. This study also demonstrated the benefits of using a dedicated cardiac MyoSPECT system, which enables reliable imaging even with low levels of activity.
- **Medical Physics profession** - The study demonstrates the potential for integrating 3D-printing technology into medical physics practice, offering a cost-effective and versatile tool for creating phantoms that better represent patient anatomy and clinical conditions.
- **University of Malta** - This study further showed the relevance of having a 3D-printing department within the University. Furthermore, it shows how different departments within the university, in this case the faculty of science and health science, can share resources to conduct research.

## 1.9 | Conclusion

This chapter presented an introduction to the study. Chapter two provides a critical review of the literature. Chapter three describes the research methodology, while chapter four presents the results together with analysis and discussion in chapter five. Chapter six then summarizes the most important conclusions of the study, proposes recommendations arising from the study, and suggests directions for future research.

# 2

# Literature Review

## 2.1 | Introduction

This review was initiated using the following electronic search engines/databases until the 1st of September 2024:

- HyDi
- Google Scholar
- PubMed

The following keywords were used to search for articles (derived using the PICO framework):

Cardiac, myocardial perfusion, cardiac scan, nuclear medicine, phantom, materials, 3D printing, techniques, fused deposition modelling, waterproofing, Fused Deposition Modelling, PETG, microfluidics, microfluidic structures.

Only papers from 1995 to 2024 were considered, meeting the inclusion criteria: (1) English full-text papers; (2) studies linking 3D printing and phantom production; (3) studies linking 3D-printing and waterproofing; (4) studies linking phantoms and evaluation of NM machine performance. Exclusion criteria included: (1) insufficient data; (2) inadequate methodology; (3) expert opinion papers.

This section discusses the relevance of MPI in the NM department. Through this literature review, the feasibility of 3D printing left ventricular cardial model will be discussed. Followed by the importance of and the techniques used to evaluate the performance of the machinery and systems found in the department.

## 2.2 | Cardiac imaging in Nuclear Medicine - Myocardial Perfusion

In this section of the Literature Review, the importance of Cardiac Imaging in Nuclear Medicine will be discussed.

### 2.2.1 | Importance of Cardiac Imaging in Nuclear Medicine

Cardiac imaging in nuclear medicine is a specialised area that utilises small amounts of radiopharmaceuticals to evaluate the function and structure of the heart. This type of imaging is primarily used to assess the health of the heart, diagnose any cardiac pathologies and guide the medical staff into management and treatment decisions. Crean et al. (2004) explained that MPI is an indispensable tool for the following reasons:

#### Detection of Coronary Artery Disease

First of all, MPI is particularly valuable in detecting areas of the heart muscle that receive inadequate blood supply due to partial or complete blockages in the coronary arteries. This condition is often caused by Coronary Artery Disease (CAD). MPI can identify these areas by showing the distribution of blood flow in the heart both at rest and during stress (Zaret and Beller, 2005).

#### Assessment of the Severity and Location of Ischemia

As a result, of this restriction in blood supply to the heart one might experience Ischemia. Which is the death of heart cells when they do not receive enough oxygen. MPI helps in quantifying the

extent and the locality of ischemia. This is crucial for planning appropriate therapeutic strategies such as angioplasty or coronary artery bypass surgery (Iskandrian and Garcia, 2012).

### Evaluation of Myocardial Viability

MPI can distinguish between viable and non-viable heart muscle. Viable myocardium may recover function if blood flow is restored, whereas non-viable tissue is unlikely to benefit from attempts to improve blood flow. This information helps in making decisions about the potential benefits of surgical interventions versus medical management (Bonow et al., 2011).

### Guidance for Treatment Plans

Ultimately, the results obtained from a MPI scan guide treatment decisions and provide evidence for treating the patient. Depending on the outcome of the images the medical staff will then choose on whether to treat the patient with invasive procedures like coronary angiography or just manage it with medication and lifestyle changes (Fihn et al., 2014).

### Monitoring and Follow-up

Post-treatment MPI is used to evaluate the success of any interventions taken and to monitor the progression of the disease. Making it a valuable tool for the ongoing management of patients with cardiac conditions.

### Summary

In summary, myocardial perfusion imaging forms the backbone of non-invasive cardiac diagnostics because of its ability to assess the functional impact of CAD on the heart. Allowing medical professionals to evaluate myocardial viability and guide them in clinical management in both acute and chronic settings.

## 2.3 | Anatomy of the Heart

An extensive review of the major cardiac divisions and anatomical features necessary to comprehend MPI is given in this section. The 17-segment heart model is suggested by the American Heart Association (AHA) for assessing myocardial perfusion or left ventricular function. It splits the left ventricle into three equal sections, each of which is perpendicular to the long axis: basal, mid-cavity, and apical. This causes the apical region to be divided into four segments of 90°, while the basal and mid-cavity parts are further divided into six segments of 60° each. The very tip of the ventricle, known as the apex, is represented by the apical cap. Figure 2.1 depicts each of these portions.

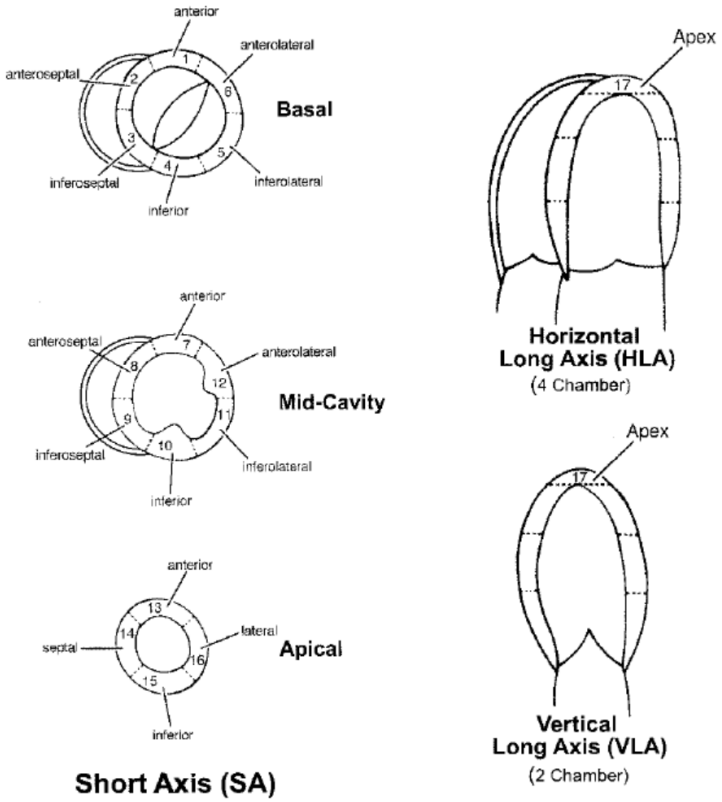


Figure 2.1: Regional Wall Segments (AHA et al., 2002)

The functional values obtained from the 17 cardiac segments can be organised into a polar plot, as

in figure 2.2, simplifying comparisons across different conditions (e.g., rest vs. stress). The polar plot displays the segments in a series of concentric rings: the apex is in the centre, followed by the four apical segments, six mid-cavity segments, and six basal segments. This arrangement allows for easy comparison of outcomes between patients or scenarios, visualising myocardial perfusion distribution across the heart.

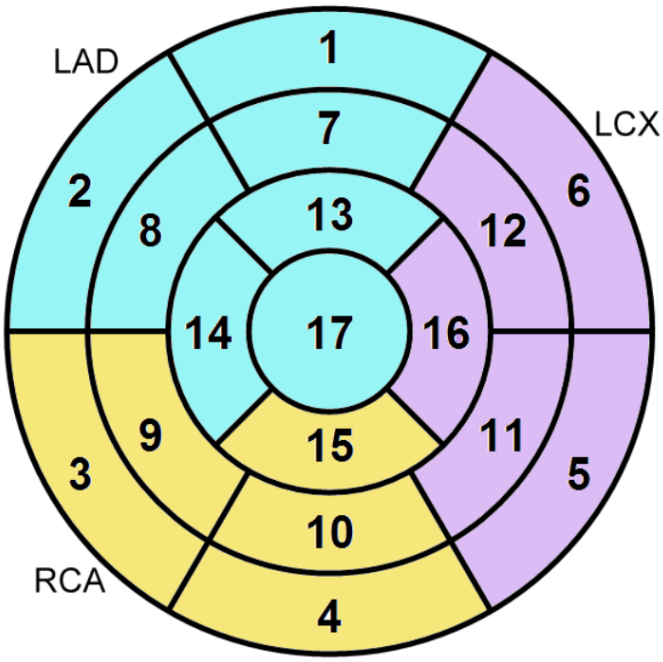


Figure 2.2: Polar plot (AHA et al., 2002)

Table 2.1: Cardiac Segments

| **Basal Segments** | **Mid-cavity Segments** | **Apical Segments** |
|---|---|---|
| 1. basal anterior | 7. mid anterior | 13. apical anterior |
| 2. basal anteroseptal | 8. mid anteroseptal | 14. apical septal |
| 3. basal inferoseptal | 9. mid inferoseptal | 15. apical inferior |
| 4. basal inferior | 10. mid inferior | 16. apical lateral |
| 5. basal inferolateral | 11. mid inferolateral | 17. apex |
| 6. basal anterolateral | 12. mid anterolateral | |

Additionally, figure 2.2 and table 2.1 display the specific coronary artery regions assigned to each

segment. The Left Anterior Descending (LAD) artery generally provides blood to segments 1, 2, 7, 8, 13, 14, and 17, while the Right Coronary Artery (RCA) supplies segments 3, 4, 9, 10, and 15. The Left Circumflex (LCX) artery supplies blood to segments 5, 6, 11, 12, and 16. The American Heart Association (AHA) highlights the presence of variability in the blood flow to the coronary arteries, particularly at the apical cap. This region can get blood from any of the three arteries.

### 2.3.1 | Cardiac Imaging Devices

There are many devices which can be used to image the heart. However, only the devices discussed in this section are capable of performing MPI. These are:

- Traditional Anger Cameras
- Single Photon Emission Computed Tomography with integrated Computed Tomography (SPECT/CT) systems
- Cardiac Dedicated Gamma Cameras - Also referred to as Dedicated Solid State Cardiac Systems
- Positron emission tomography (PET) systems paired with computed tomography (CT) scanners

#### 2.3.1.1 | Gamma Camera System

Prior to the SPECT/CT systems, the traditional anger camera systems were used for cardiac SPECT imaging. The core of the gamma camera is the detector head, which contains the scintillation crystal, the Photomultiplier Tubes (PMT)s and any required electronics.

The scintillation crystal is typically Sodium Iodide doped with Thallium [NaI(TI)]. This crystal is chosen because of its optimal combination of properties for detecting the range of gamma-ray energies typically used in nuclear medicine. Specifically, those emitted by Technetium-99m. Furthermore, NaI(TI) crystals produce a high light yield when gamma rays interact with them. This light signal is then picked up by the PMTs behind the crystal to convert it to an electronic signal.

Adding to this, it is highly efficient at stopping gamma rays too. The biggest downside to it, however, is its hygroscopic nature. As a result, NaI(TI) crystals are very sensitive to moisture and as a requirement, they must be housed in a hermetically sealed container to prevent degradation.

The dual head system, typically configured in a 90-degree or L-mode setup for MPI, is discussed by Garcia et al. (2011). Patients are usually positioned supine, with the camera heads brought as close as possible to the chest to ensure that the heart is within the optimal field of view; this is better understood through figure 2.3. Low-Energy High-Resolution Collimators, which were chosen for their effectiveness with low-energy isotopes like Technetium-99m, were essential for detailing areas of reduced blood flow within the heart in MPI.

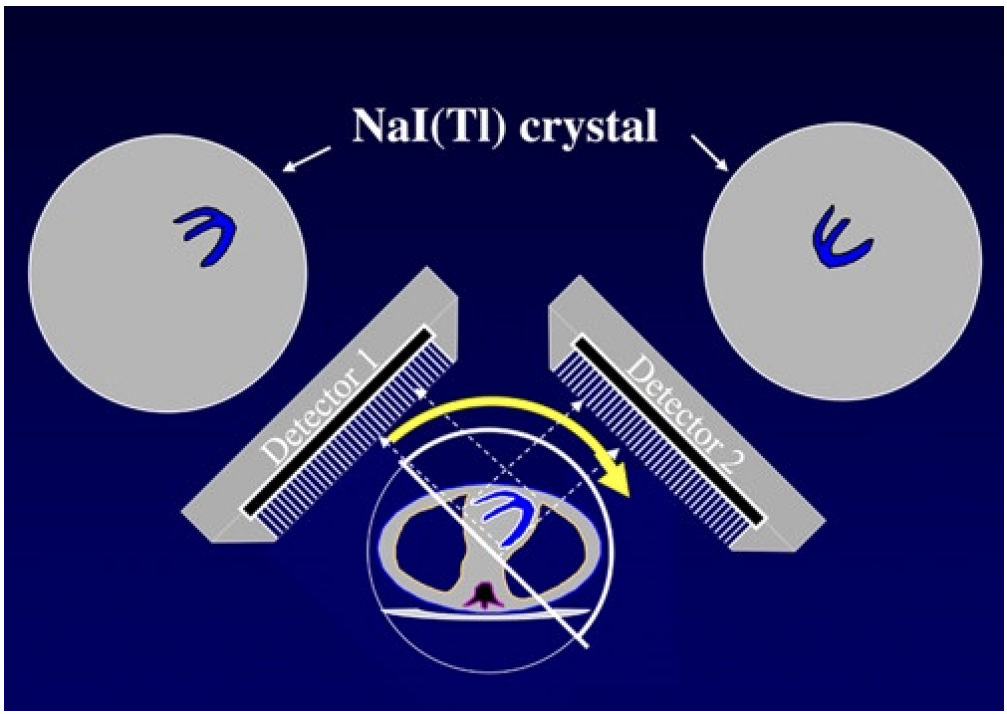


Figure 2.3: Conventional Gamma Cammera setup for Myocardial SPECT imaging (Garcia et al., 2011)

#### 2.3.1.2 | Single Photon Emission Computed Tomography with integrated Computed Tomography (SPECT/CT)

Until a few years ago, and even in most NM departments today, SPECT/CT systems were the most commonly used devices for MPI due to their widespread availability, established protocols, and versatility within the NM department. These systems use gamma cameras, often similar or identical to traditional Anger cameras, to detect the gamma rays emitted by radiopharmaceuticals administered to the patient, which accumulate in the heart muscle.

Slomka et al. (2016) further explained that the integration of SPECT with computed tomography (CT) has led to hybrid SPECT/CT systems that combine functional and anatomical imaging. SPECT/CT provides accurate attenuation correction, reduces artefacts and improves the localization of perfusion defects. Hence, hybrid imaging enhances the assessment of coronary artery calcifications and the overall evaluation of cardiac conditions.

The SPECT/CT system found in Malta's NM department is the GE NM/CT 870 DR. It is an advanced SPECT/CT system that brings several enhancements over traditional systems used in nuclear medicine. It integrates a Low Energy High Resolution and Sensitivity (LEHRS) collimator, which improves both spatial resolution and system sensitivity compared to the conventional Low Energy High Resolution (LEHR) collimator.

For comparison, "the spatial resolution and system sensitivity of the NM/CT 870 DR with an LEHR collimator for Tc-99m were 7.4 mm and 72 cps/MBq, respectively. The LEHR collimator has a hole diameter of 1.5 mm, a septal thickness of 0.2 mm, and a hole length of 35 mm." By contrast, the LEHRS collimator has a "hole diameter of 1.43 mm, a septal thickness of 0.13 mm, and a hole length of 32 mm. This configuration improves the system sensitivity to 92 cps/MBq while maintaining the same spatial resolution of 7.4 mm"(Shibutani et al., 2021; Thibault et al., 2019).

Further enhancing imaging, the NM/CT 870 DR features software known as Clarity 2D, which processes planar scintigraphy acquired with the LEHRS collimator. This reduces noise and im-

proves contrast, significantly boosting lesion detectability in gamma scintigraphy compared to the standard LEHR collimator. This improvement has been validated in previous studies, demonstrating the NM/CT 870 DR's superior performance in nuclear imaging.

Additionally, according to GE-HealthCare (2021) the system offers the SwiftScan Planar and SwiftScan SPECT modes, which combine step-and-shoot continuous scanning with 2D planar processing. These modes optimise scanning by enhancing both clarity and sensitivity, thereby allowing for reduced scan times or lower injected doses without sacrificing image quality. The NM/CT 870 DR is also equipped with Elite NXT NM detectors, designed to improve detection sensitivity and address challenges in nuclear medicine. Paired with a 16-slice CT scanner featuring IQ Enhancement technology, this system achieves helical coverage speeds comparable to a 50-slice CT scanner, making it more efficient and precise in quantitative imaging.

DePuey (2016) champions the use of SPECT/CT over modern solid-state detectors. These cameras provide crucial rotating projection images that aid in correcting patient motion during scans and can accommodate larger patients, which solid-state cameras cannot due to fixed fields of view and size limitations. Additionally, SPECT/CT systems are equipped with attenuation correction technology, which enhances image clarity by compensating for soft tissue interference. They also offer cost-effective solutions with low-count density software that enables shorter SPECT acquisition times and reduced radioisotope usage, nearly matching the efficiency of advanced CZT detectors. This makes gamma cameras particularly attractive for many small to medium-sized nuclear medicine facilities due to their versatility and broad application range.

However, the preference for conventional gamma cameras is not without criticism, especially with the advent of solid-state CZT detectors. Slomka et al. (2014) highlights that gamma cameras fall short in spatial and energy resolution compared to CZT detectors, posing significant diagnostic challenges. These include difficulties in detecting small lesions, the potential for misinterpreting perfusion defects, and the introduction of artifacts such as scatter and attenuation. Moreover, the extended imaging times associated with gamma cameras increase the likelihood of patient move-

ment, thus introducing motion artifacts and degrading the quality of the imaging results.

Garcia et al. (2011) further elaborates on the fact that the traditional design of SPECT cameras using standard parallel-hole collimators has been prevalent for more than half a century. However, this design is largely inefficient, as it only harnesses a small portion of the available NaI crystal detector area for cardiac imaging. Additionally, the predominant use of the filtered backprojection reconstruction algorithm in current SPECT systems is based on technology that dates back over 90 years. Hence, this further supports why most NM departments are now opting for the new Cadmium Zinc Telluride (CZT) detectors.

#### 2.3.1.3 | Cardiac Dedicated Gamma Cameras

The new devices which are taking over nuclear cardiac imaging are the solid-state CZT detectors. Garcia et al. (2011) explained that thanks to the advancements made, both in solid-state detectors and in reconstruction algorithms, these devices are "poised to meet the present healthcare challenges by improving image quality while reducing study time, radiation dose to the patient, and ultimately, study cost."

These solid-state detectors instantly detect gamma rays within the semiconductor material, removing the requirement for an intermediate conversion process, such as that used with scintillation crystals. The direct conversion detection technology provides significant benefits compared to conventional Anger camera designs. These advantages include higher photon detection efficiency and improved energy resolution. In addition, these detectors do not necessitate the use of photomultiplier tubes, allowing for a more condensed design. This facilitates the creation of smaller SPECT/CT systems that can be used for attenuation correction and hybrid imaging (Jo and Kang, 2024). In addition to these developments, the latest cardiac-dedicated SPECT cameras are now equipped with several detectors that are specifically designed to capture images of the heart's field of view. Figure 2.4 depicts the simultaneous acquisition of heart images by 8 detectors positioned around the patient's heart. The study conducted by Slomka et al. (2016) provided additional evidence to demonstrate the advantages of utilising CZT detectors that rely on solid-state

technology. These features encompass increased sensitivity (5-10 times greater) and enhanced visual resolution (2-3 times greater). This enables substantial decreases in the administered dosage and the time required for data collection.

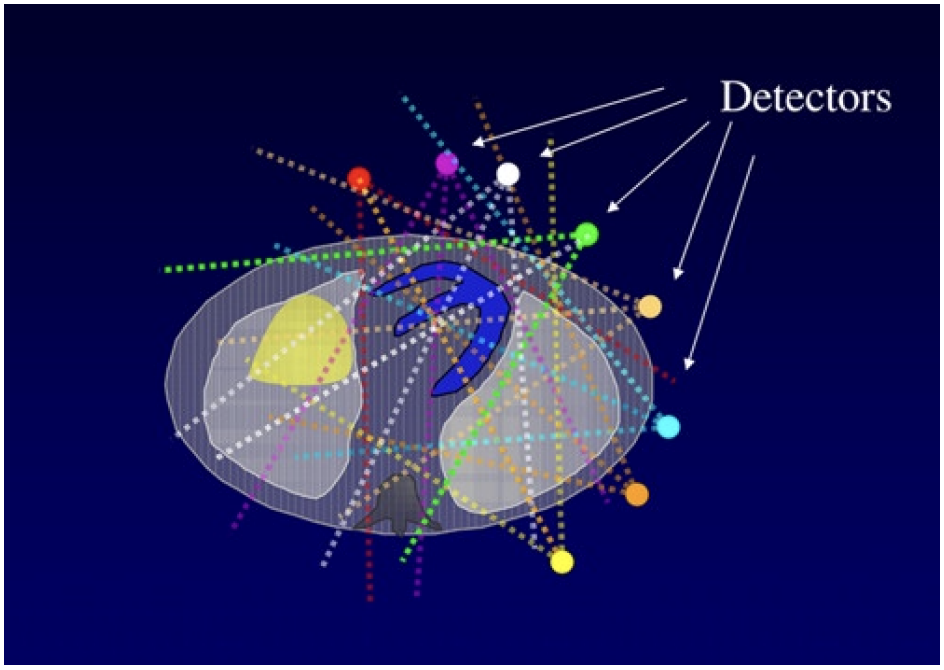


Figure 2.4: Detector design of modern cardiac dedicated SPECT system (Garcia et al., 2011)

Wu and Liu (2019) also explained that the combination of "high spatial resolution, high energy resolution, and high sensitivity leads to superior overall image quality. This provides an additional dimension of dose reduction by minimizing the need for unnecessary second rest scans in stress-first protocols and reducing the need for additional coronary CT angiography (CTA)".

The study conducted by Duvall et al. (2013) found that the high sensitivity of CZT-SPECT, when utilised for stress-only imaging, not only minimises the radiation dosage for patients but also significantly decreases occupational radiation exposure for staff members in nuclear cardiology laboratories. An examination of the data from personal dosimeters showed a notable reduction of approximately 40% in occupational exposure. This decrease was achieved by utilising decreased injection activity and choosing to employ stress-only imaging with the GE 530c scanner.

Previous reconstruction algorithms could not take into account the loss of resolution with distance which is inherent to the parallel-hole collimators used in the conventional gamma camera. Garcia et al. (2011) continued to explain that recent advancements in iterative image reconstruction have significantly improved spatial resolution and reduced noise by using techniques like resolution recovery and noise regularization. These methods mathematically correct resolution degradation and accurately account for additional counts, allowing for shorter acquisition times without compromising image quality. Enabling faster imaging with high diagnostic performance and accurate functional measurements.

Oddstig et al. (2019) provided a detailed comparison of the attenuation patterns observed in myocardial SPECT images acquired using CZT and conventional gamma cameras. CZT cameras demonstrated more consistent and accurate attenuation correction, highlighting their advantages in cardiac imaging over traditional gamma cameras. Hence, combining this with CT would result in great attenuation correction.

For the purpose of this review, only the two main cardiac dedicated solid-state detectors will be discussed. These are Spectrum Dynamic's D-SPECT scanner and GE Healthcare's 530c and 570c, which led to the production of the next generation cardiac-dedicated SPECT known as the MyoSPECT. The MyoSPECT will be discussed in the next section, however. As focus will be placed on describing the differences between the D-SPECT and the 530c.

### D-SPECT

The CZT Solid-State, Multiple Scanning Detector Design (D-SPECT) system developed by Spectrum Dynamics, features cadmium zinc telluride (CZT) solid-state detectors arranged in nine arrays with dimensions of 4 cm by 16 cm, as seen in figure 2.5. Each array is equipped with tungsten parallel-hole collimators with larger square holes (2.26 mm) and shorter lengths (21.7 mm), enhancing sensitivity by capturing more photons emitted from the heart. These detectors rotate independently around a central axis during data acquisition, covering the entire field-of-view

(FOV) and focusing on the heart to achieve higher detection efficiency (Erlandsson et al., 2009).

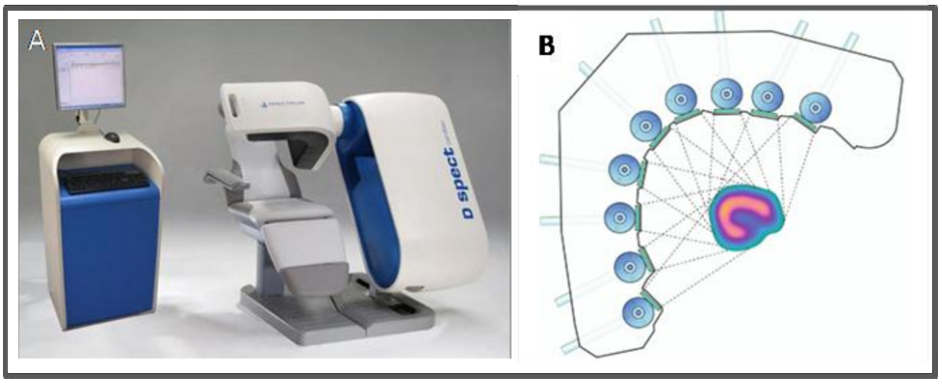


Figure 2.5: Spectrum Dynamic D-SPECT System - Costa (2012)

The D-SPECT system utilises resolution recovery (RR) approaches to counteract any potential loss of resolution caused by the bigger collimator holes. The technique preserves a spatial resolution similar to traditional systems by simulating the collimator-detector response during reconstruction (Erlandsson et al., 2009). The performance evaluations show that "the spatial resolution achieved with ordered-subset expectation maximisation (OSEM) and standard clinical smoothing is approximately 12.5 mm." This is comparable to the "13.7 mm resolution achieved by the GE Infinia scanner when using low-energy high-resolution (LEHR) collimators and filtered back-projection (FBP) reconstruction with Butterworth post-filtering", as reported in the study by Gambhir et al. (2009). The "sensitivity of the D-SPECT system varies from 647 to 1107 counts per second per MBq, which is 4.6 to 7.9 times greater than that of the GE Infinia. The energy resolution at 140 keV is 5.5%." Nevertheless, the D-SPECT system does not have the ability to do transmission scans for attenuation correction (Erlandsson et al., 2009).

### GE Healthcare NM 530c SPECT and NM 570c SPECT/CT

The Discovery NM 530c and NM/CT 570c are advanced cardiac imaging systems from GE Healthcare. The Discovery NM 530c is a dedicated cardiac SPECT system that utilizes GE's advanced Alcyone technology, featuring 19 detector modules with cadmium zinc telluride (CZT) detectors

arranged in a 2 by 2 array. Each detector module measures 4 cm by 4 cm and is paired with a tungsten pinhole collimator. The detectors in the 530c are stationary, focusing solely on the heart to maximize sensitivity and image quality. This configuration results in a central spatial resolution of 5.8 mm and an average sensitivity of 657 counts per second per MBq, with a maximum rate of 848 counts per second per MBq in the quality FOV (Bocher et al., 2010).

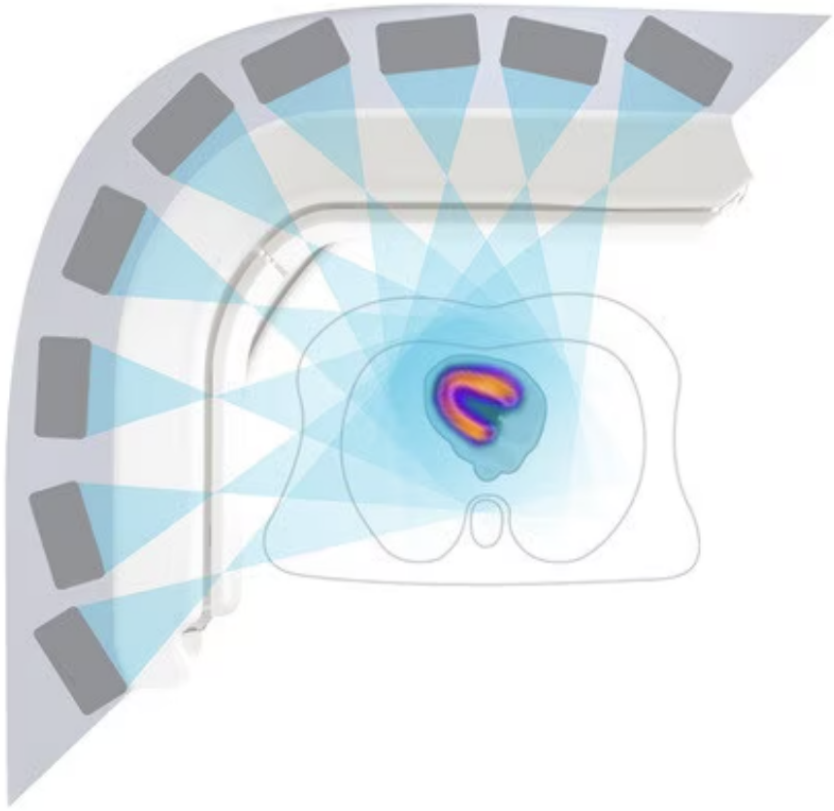

Figure 2.6: GE Healthcare - 530c HealthCare

The Discovery NM/CT 570c integrates the SPECT capabilities of the 530c with computed tomography (CT). Providing both functional and anatomical imaging. This hybrid system retains the advanced features of the NM 530c, including CZT detectors and Alcyone technology, while adding the benefits of CT for accurate attenuation correction. This reduces artefacts and enhances diagnostic accuracy. The NM/CT 570c achieves a complete cardiac scan, including myocardial perfu-

sion imaging (MPI), computed tomographic angiography (CTA), and calcium scoring (CaSC), in less than five minutes, optimizing patient throughput and convenience.

Wu and Liu (2019) explained that both systems employ pinhole collimators where the resolution and sensitivity are location-dependent, varying with the inverse square of the distance from the source to the pinhole. The average spatial resolution across the entire FOV is approximately 7 mm, with a gradient that requires precise patient positioning to ensure the heart remains within the optimal imaging range (Kennedy et al. 2014). The energy resolution for 140 keV photons is 5.4%, contributing to the systems' high image quality and diagnostic performance.

Since both systems include CZT detectors, these systems have high spatial and energy resolution; thanks to the detector's capabilities to directly convert gamma rays into digital signals. The sensitivity is further enhanced by multi-pinhole collimators and a stationary detector design that focuses entirely on the heart. These features enable fast acquisition times, allowing for complete scans in just a few minutes. In the case of the 570c, hybrid imaging combines SPECT and CT, offering comprehensive diagnostic capabilities that include attenuation correction and anatomical imaging.

### GE Healthcare - MyoSPECT

The MyoSPECT is GE Healthcare's next-generation cardiac-dedicated nuclear medicine scanner and also the one found in Malta's NM department. Chen et al. (2024b) explained that MyoSPECT systems typically use a multi-row and multi-column detector arrangement. This results in a multi-plane alignment of detectors as seen in figure 2.7. This configuration ensures comprehensive coverage of the heart, capturing detailed images from multiple angles simultaneously.

GE Healthcare also highlighted that, in addition to the previously mentioned advantages of the 530c, like higher spatial resolution, higher sensitivity and reduced scan times, the MyoSPECT system offers an extended field of view that increases the imaging volume by 76%. This enhancement accommodates a broader range of patients, including those with higher body mass indexes

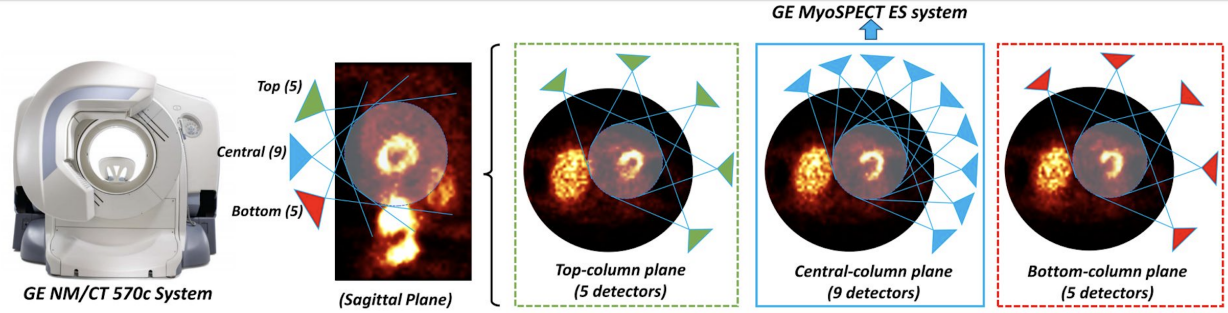


Figure 2.7: Multi-plane configuration of MyoSPECT Gamma Camera - Chen et al. (2024a)

(BMIs). However, in certain cases, this extended field of view might still be insufficient, necessitating the use of conventional gamma cameras or SPECT/CT systems. Furthermore, MyoSPECT also provides to different attenuation compensation solutions. Where attenuation is evaluated by imaging in prone and supine positions or by combining perfusion imaging with separate CT images in Xeleris. Finally, GE also included a smart position workflow feature which will provide automated scan position and FOV recommendations.

Advancements in hardware are not the only factors that make the MyoSPECT system more advanced than its predecessors. In addition to incorporating resolution recovery and noise regularization algorithms, Jo and Kang (2024) explained that the system also utilizes the maximum likelihood expectation maximization (MLEM) algorithms. The new iterative algorithm for image reconstruction, OSEM, is now widely used. OSEM enhances image quality and reduces noise by segmenting data into subsets, optimising images within each subset, and iteratively combining them. This results in high-resolution images that clearly represent fine structures, crucial for accurate interpretation in myocardial perfusion SPECT. Additionally, OSEM reduces processing time, improving the efficiency of patient diagnosis and examination.

All of these factors are what make the MyoSPECT such a reliable tool for MPI.

### Potential pitfalls and disadvantages of CZT scanners

While the MyoSPECT system offers a 76% increase in it FOV compared to it predecessor, it may still be insufficient for some patients with a very high Body Mass Index (BMI) or those with specific anatomical variations. In such cases conventional gamma cameras would need to be used. DePuey (2016) even expressed the fact that "a solid-state detector as the sole nuclear imaging device in a facility may not be a particularly wise choice." A secondary SPECT/CT camera would be ideal for imaging the larger patients.

Fiechter et al. (2012) took this a step further and evaluated the impact of increased body mass on the quality of myocardial perfusion imaging using the CZT cameras. A receiver-operating-curve analysis identified a "cutoff BMI of 39 kg/m² ($P < 0.001$) for achieving diagnostic image quality. In patients with a BMI of 40 kg/m² or greater, image quality was nondiagnostic in 81% of cases. However, CT-based attenuation correction improved diagnostic image quality, reducing the nondiagnostic rate to 55%. Repositioning further enhanced image quality. Rescanning with a conventional SPECT camera resulted in diagnostic image quality for all patients with a BMI of 45 kg/m² or more." Fiechter et al. (2012) also explained that due to the design of the CZT cameras, "their pinhole collimation geometry and a smaller field of view, these cameras are more prone to artefacts. Hence, patients with a BMI of 40 kg/m² or higher should ideally undergo myocardial perfusion imaging on a conventional SPECT camera, as obtaining diagnostic image quality on a cadmium-zinc-telluride (CZT) camera is challenging." The introduction of the new extended field of view still has not been evaluated. Thus, making this a current gap in the research.

Agostini et al. (2016a) further noted that the attenuation correction techniques offered by the MyoSPECT system are still inferior to those provided by SPECT/CT systems. This is primarily due to the reliance on a previously acquired CT scan, which may not be as reliable because of potential issues with patient positioning reproducibility. In SPECT/CT systems, the CT scan is performed simultaneously with the SPECT scan, ensuring that the patient's position remains consistent between the two imaging modalities. This consistency is crucial for accurate attenuation correction, as any variation in positioning can lead to misalignment and errors in the final images.

Therefore, while the MyoSPECT system provides useful attenuation correction capabilities, it may not achieve the same level of attenuation correction as SPECT/CT systems.

#### 2.3.1.4 | PET/CT for cardiac imaging

MPI can also be conducted using a PET/CT scanner. PET/CT offers several advantages over traditional cardiac-dedicated cameras. One of the primary benefits is superior image quality, thanks to higher spatial and contrast resolution, which allows for more precise localization and quantification of perfusion defects. PET enables absolute quantification of myocardial blood flow (MBF) and coronary flow reserve (CFR), providing valuable functional information for clinical decision-making. The high sensitivity and rapid decay of PET tracers result in shorter scan times, enhancing patient comfort and throughput. Additionally, PET typically involves lower radiation exposure compared to SPECT, due to the efficient detection and short half-lives of PET tracers. Accurate attenuation correction using CT data further improves the reliability of perfusion assessments, making PET/CT a highly effective tool for cardiac imaging.

Despite its advantages, PET/CT also has several disadvantages when compared to cardiac-dedicated cameras. The high cost of PET/CT systems and the need for cyclotrons to produce certain tracers, like F-18, limit accessibility. This is one of Malta's current issues in the NM department. PET/CT protocols are also more complex and require specialised training for radiographers and clinicians, adding to the operational complexity. Finally, stress testing with PET typically relies on pharmacological agents, since time is an issue with the half-lives of PET isotopes. Thus, it may not be suitable for all patients and can have side effects.

## 2.4 | Radiopharmaceuticals used for MPI

According to Boschi et al. (2022), the ideal radiopharmaceutical for MPI should combine high myocardial uptake, low radiation dose, minimal uptake in non-target organs during image acquisition, and compatibility with advanced imaging technologies. Additionally, it should have a high first-pass myocardial extraction fraction, rapid blood clearance, and a linear relationship between

myocardial uptake and coronary blood flow. For traditional Anger cameras and cardiac-dedicated CZT cameras, [99mTc] Tc-Sestamibi, [99mTc] Tc-Tetrofosmin, and Thallium-201 [TI-201] are commonly used. TI-201 has the least non-target organ uptake but its long half-life and lower photon energy result in higher patient doses and lower image quality. Therefore, Tc-99m compounds are more popular. Tc-99m tetrofosmin is preferred due to its faster liver and blood clearance, which leads to clearer images and less interference from non-target organ uptake. However, Tc-99m sestamibi remains widely used due to its well-established protocols and consistent myocardial uptake. This preference is reflected in Malta's Nuclear Medicine department, which focuses on Sestamibi.

In MPI, the choice of dosage for Tc-99m sestamibi can be based on fixed doses, weight-based calculations, or protocol-specific variations. Each method aims to balance optimal image quality with minimal radiation exposure. Below is a detailed analysis based on various studies and protocols.

### 2.4.1 | Fixed Dose Protocol

Standard fixed dose protocols simplify the dosing process by providing a consistent amount of radiopharmaceutical regardless of patient size. Anagnostopoulos et al. (2004) recommend a one-day protocol using a fixed dose of 740-1480 MBq for combined stress and rest imaging. This approach ensures adequate myocardial uptake and image quality across various patient sizes but may lead to suboptimal dosing for very small or very large patients, affecting image quality and radiation exposure. Dorbala (2012) suggests a two-day protocol with lower doses, typically 370 MBq for stress and an additional 370 MBq for rest imaging. This method reduces radiation dose per session, beneficial for patients, but requires multiple visits, which may be inconvenient.

### 2.4.2 | Weight Based Protocol

Weight-based dosing adjusts the amount of radiopharmaceutical based on the patient's body weight, aiming to optimize image quality and minimize radiation exposure. Agostini et al. Agostini et al. (2016b) suggested doses of 3-5 MBq/kg for stress and 9-15 MBq/kg for rest imaging

when using CZT cameras. This method tailors the dose to the patient's size, potentially improving image quality and reducing unnecessary radiation. However, it is more complex to calculate and administer, requiring precise weight measurements. Anagnostopoulos et al. (2004) also recommended using approximately 9-15 MBq/kg with adjustments for different patient sizes to ensure optimal imaging results.

The European Association of Nuclear Medicine (EANM) dosage calculator, based on dosage cards, offers guidance on weight-based dosing. These cards are derived from publications such as Jacobs et al. (2005), Lassmann and Treves (2014) and Lassmann et al. (2008), providing optimized, tracer-dependent dosage calculations to ensure effective dosing across various patient weights.

### 2.4.3 | Protocol Specific Variations

In MPI, several protocols balance image quality and radiation exposure. The stress-only protocol involves imaging only after stress (exercise or pharmacological). If stress images are normal, rest imaging is omitted, reducing radiation exposure and procedure time. Verberne et al. (2015) explained, however, that this may not suit patients with significant coronary artery disease. The one-day stress-rest protocol performs both stress and rest imaging on the same day, using a lower dose of radiopharmaceuticals for the stress test followed by a higher dose for the rest test. A flow chart of this process is given in figure 2.8. This is convenient, as both tests are completed in one visit, but it results in a higher cumulative radiation dose. The two-day protocol separates stress and rest imaging into different days, lowering the radiation dose per session and improving image quality. The downside, though is that it requires patients to return for a second visit (Hyafil et al., 2019). Thanks to the introduction of the new CZT cameras a new ultra-low dose protocol is also being developed in many clinics. Allowing physicians to further minimize radiation exposure while maintaining image quality (Mouden et al., 2012a).

### 2.4.4 | Special Considerations

Pediatric patients' dosages are calculated based on body weight using the EANM pediatric dosage card (Jacobs et al., 2005; Lassmann and Treves, 2014). The focus is on minimizing radiation exposure while ensuring diagnostic image quality. For obese patients with a BMI greater than 40 $kg/m^2$, conventional SPECT systems are recommended over CZT cameras due to better diagnostic image quality (Fiechter et al., 2012). The increased field of view and better attenuation correction of standard gamma cameras make them more suitable for larger patients. This should be reexamined, as the original study was conducted on the 530c CZT camera. The newer MyoSPECT system has a field of view that is 76% larger than the 530c, making this an important limitation that warrants further investigation.

### 2.4.5 | Malta's Protocol

With all of the different protocols now explained, Malta adopts a fixed dose protocol in the NM department. According to the Radiation Protection Committee (RPC) patients in Malta are administered the doses found in table 2.2.

| Procedure | Stress (MBq) | Rest (MBq) |
|---|---|---|
| Myocardial Perfusion (2-day protocol) | 400 | 500 |
| Myocardial Perfusion (1-day protocol) | 200 | 600 |

Table 2.2: Maltese DRLs for MPI

These values align with those from other protocols, simplifying the department's preparation of the required activity for each patient. However, it's crucial to consider that patients differ in size and shape. For instance, obese patients receive the same dose, but the acquisition time is extended to compensate. Additionally, in some cases, the MyoSPECT's detectors may not fully capture the heart, as it may be outside the field of view due to the patient's size. In such cases, the patient must be imaged using SPECT/CT instead.

### 2.4.6 | Uptake of radiopharmaceutical in myocardium and other organs

Boschi et al. (2022) explained that Tc-Sestamibi demonstrates rapid myocardial uptake, reaching peak levels approximately 1 minute after intravenous injection. By 5 minutes post-injection, less than 5% of the initial activity remains in the bloodstream. This radiotracer has an extraction coefficient of 65%, which, although effective, is lower compared to that of thallium-201 which is 85%. After Tc-Sestamibi administration, approximately 1% of the injected dose accumulates in the myocardium at rest, while uptake slightly increases to 1.4% following stress or exercise, measured 1 hour post-injection.

## 2.5 | Dose Administration and Imaging Protocol

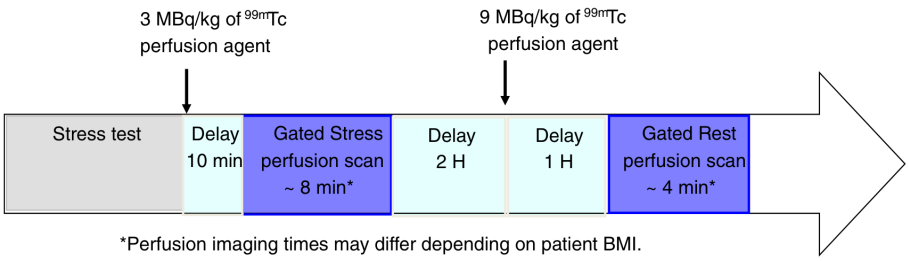


Figure 2.8: One day stress-rest protocol for MPI - Agostini et al. (2016a)

To further understand the flow of patients within the department, one should interpret Figure 2.8 in more detail. According to Hyafil et al. (2019), the maximum wait time for imaging post-injection is 60 minutes to ensure low uptake in non-target organs. During stress testing, the radiopharmaceutical is administered at peak stress.

Scan duration varies; traditional SPECT/CT systems take 15-20 minutes, while newer CZT cameras reduce this to around 7 minutes. Agostini et al. (2016a) highlighted that with new CZT cameras, imaging time is so reduced that in the same 20 minutes previously required for a traditional Anger cameras, CZT cameras allow for prone and supine imaging for attenuation correction and the rest scan. This efficiency facilitates a better workflow and improves patient throughput.

Furthermore, in a study involving 456 patients, Mouden et al. (2012b) explained that "stress-only images acquired on the GE 570c system were more frequently interpreted as normal, with identical clinical outcomes after a 1-year follow-up compared to those acquired on conventional scanners." As a result, they concluded that "the need for rest imaging (35% versus 56%) and CTA (20% versus 28%) was significantly lower, leading to a reduced injected activity (658±390 MBq versus 840±421 MBq) and shorter total imaging time (6.39±1.91 minutes versus 20.40±7.46 minutes)." This indicates that these cameras not only improved image quality but also reduced the required dose for patients and shortened the imaging time.

## 2.6 | Phantom Requirements for Nuclear Medicine

A cardiac phantom can come in two versions: static and dynamic. A static phantom accurately represents the anatomy of a non-moving heart, providing consistent and reproducible results for system calibration and quality assurance. In contrast, a dynamic phantom simulates the beating motion of the heart, reflecting changes in perfusion over time. Since this dissertation focuses on the production of a static heart, the review will concentrate on static phantoms.

Whether produced with 3D printing or other traditional techniques, the phantom must meet the same requirements. After researching the department's current cardiac phantom, Data Spectrum Corporation's Cardiac Insert™ with Fillable and Solid Defect Sets™, and evaluating the works of Kiss et al. (2022) and Jasmat (2022), a set of criteria were established.

Firstly, the 3D-printed phantom has to meet specific technical criteria. Preferably, the material should be clear to semi-clear and watertight, as the space in the myocardium would be filled with radioactive liquid. It should represent the left ventricle of a normal adult individual and have filling ports that do not affect imaging.

Secondly, the phantom has to match performance criteria. The materials and parameters used

should be tissue-equivalent. Phantom imaging should mimic patient imaging for both myocardial perfusion imaging (MPI) and CT. It should have the ability to introduce defects, as with the current cardiac phantom, and be durable, long-lasting, and reproducible. Additionally, it should provide comparison capabilities with the department's current cardiac phantom.

The choice of printing technique also affects cost, availability, and reproducibility. Jasmat (2022)'s phantom, although superior to Kiss et al. (2022)'s phantom, is difficult to reproduce because it uses advanced printers that require significant competence to operate, dedicated rooms to safeguard against toxic fumes from materials used, and substantial post-print processing to ensure the print is usable. Therefore, Kiss et al. (2022)'s approach and phantoms, which are also fully compatible with the commercially available Anthropomorphic Torso Phantom of Data Spectrum Corporation, are the ones which will be investigated in this study.

## 2.7 | 3D Printing Process

Various different authors have developed anthropomorphic phantoms in the past. With each project having different approaches which can be taken. A comparative review was conducted between the works of Kiss et al. (2022), Jasmat (2022) and Green and Grice (2022) who all managed to produce a different variation of a 3D-printed phantom. Even though each one took a different approach a detailed flow chart which depicts the steps needed to be taken is included in figure 2.9.

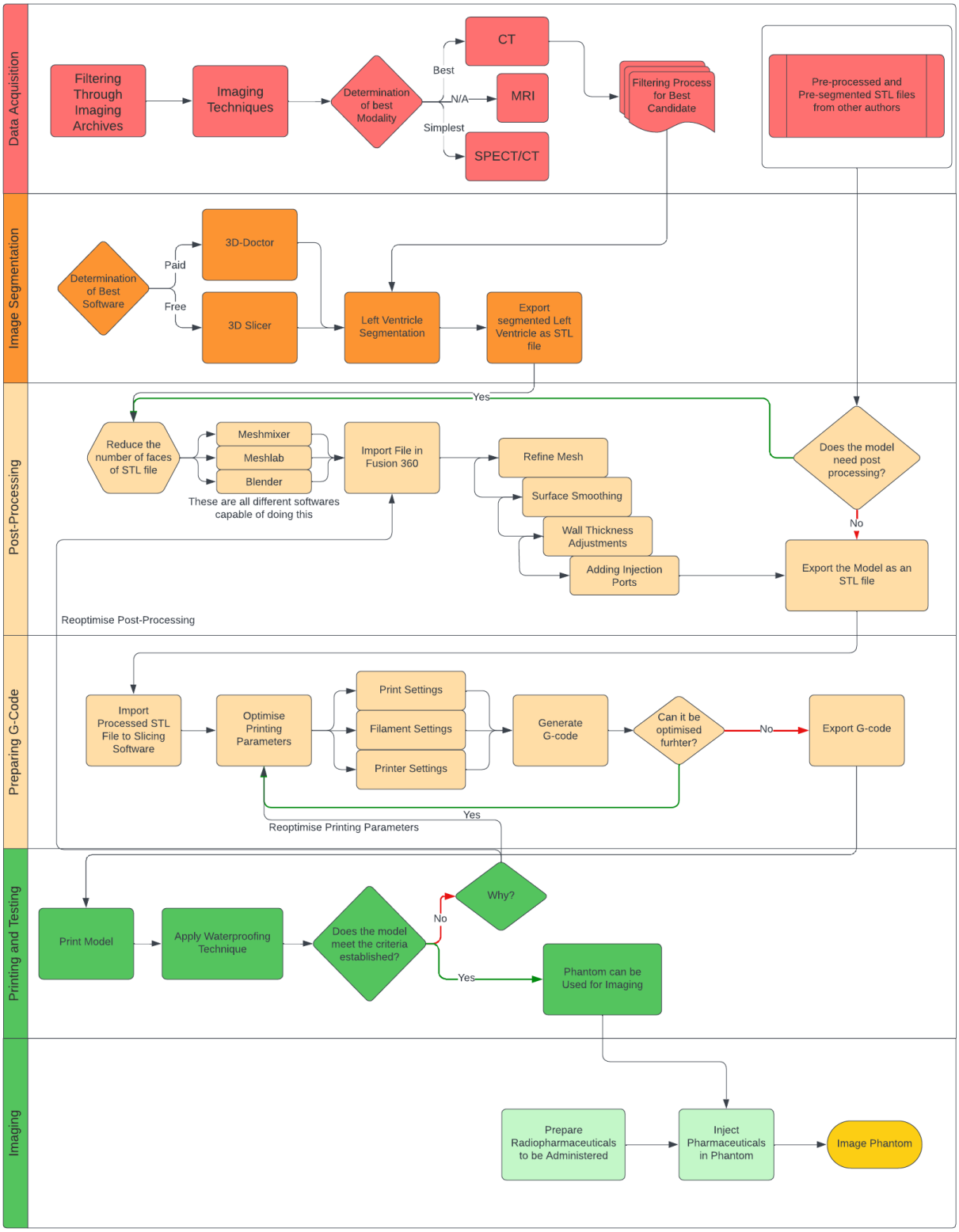


Figure 2.9: Summary of 3D Printing Process in Literature

### 2.7.1 | Phantom fabrication process

This section of the review will now provide a detailed overview of the processes that can be adopted to create the phantom that meets the criteria described in section 2.6. The flowchart in figure 2.9 illustrates the complete process and the different approaches to producing a 3D-printed nuclear medicine phantom, starting from data acquisition through to imaging.

#### 2.7.1.1 | Data acquisition

The process begins with the acquisition of imaging data, often retrieved from pre-existing imaging archives. Filtering through these archives helps identify the best possible candidate data for segmentation. Several imaging modalities can be used, including CT, MRI, and SPECT. The decision of which modality to use depends on the intended purpose of the phantom. For example, CT is often the best choice for detailed anatomical models. If suitable pre-processed and segmented STL files are available from previous authors, they can be used directly to expedite the process.

#### 2.7.1.2 | Image segmentation

Once the imaging modality and the ideal candidate is selected, segmentation is performed to segment the desired anatomical structure. In this case, the left ventricle of the heart. A variety of software options can be used for segmentation, including 3D-Doctor (paid) or 3D Slicer and Blender (free alternatives). The software is used to segment the left ventricle from each individual slice and generates a segmented STL file, which is the format required for 3D printing. After segmentation, the STL file is exported for further refinement.

#### 2.7.1.3 | Post-processing

In some cases, the segmented STL file may need post-processing to refine the 3D model. If the model needs further improvements though, tools like Meshmixer, Meshlab, or Blender can be used to reduce the number of faces and smooth the mesh. The file is then imported into Fusion 360, where additional refinements are made, including further smoothing of the surface, adjusting

wall thickness, and adding injection ports if needed. Once the model is fully refined, it can either be exported directly as an STL file or go through additional optimization steps.

#### 2.7.1.4 | Preparing G-code

The next stage is converting the STL file into G-code, the language used by 3D printers. The STL file is imported into a slicing software to fine-tune the print settings, filament settings, and printer parameters. If necessary, the file can be re-optimized at this stage to further improve print quality. Once all settings are confirmed, the G-code is generated. If further optimisations are not required, the file is ready to be sent to the 3D printer.

#### 2.7.1.5 | Printing and testing

The G-code is then used to print the model. After printing, a waterproofing technique is applied to ensure the phantom is leak-proof and capable of containing the radiopharmaceuticals used in nuclear medicine studies. The printed model is rigorously tested to ensure it meets the established criteria for quality, such as water-tightness and structural integrity. If the model does not meet these criteria, it may need further processing or adjustment to the print settings before reprinting.

#### 2.7.1.6 | Imaging

Once the phantom passes all tests and meets the criteria, it is ready for imaging. Radiopharmaceuticals are prepared, injected into the phantom, and imaging is conducted using the appropriate nuclear medicine equipment. This final step replicates the conditions of clinical imaging, providing essential data on the phantom's functionality and performance.

This flowchart represents a comprehensive guide to producing high-quality, functional 3D-printed phantoms for nuclear medicine applications, ensuring both accuracy and usability at every step of the process.

### 2.7.2 | 3D Printing Protocols and Parameters

Multiple different printing techniques can be used to produce such phantoms. Each technique has its own advantages and disadvantages. The most popular techniques have to be FDM, SLA and Polyjet Printing. As explained in section 2.6, the simplest, cheapest and most straightforward one to use is the FDM technique (Jasveer and Jianbin, 2018). Hence, the optimisation parameters of such printers were evaluated.

The preferred material among researchers for 3D printing phantoms and water proof parts in general is Polyethylene Terephthalate Glycol (PETG). This material is chosen for its durability and excellent resistance to water, qualities that also make it the material of choice for commercial water bottles. For optimal results, the department has selected Prusament as the filament brand, known for its high-quality PETG and full compatibility with the department's existing 3D printer. For the Ultimaker printer, the brand's own Ultimaker PETG is then the most suitable version for it.

After selecting the material, it is crucial to fine-tune the printing parameters to balance print speed, quality, and waterproofing. Although modern 3D printers are capable of printing at high speeds, achieving the necessary quality and waterproofing requires a compromise on speed. Green and Grice (2022); Kiss et al. (2022); Kočí (2021, 2024); O (2023); Romero et al. (2021)'s work were reviewed to set the testing criteria found in table **??**.

The optimum parameters will be evaluated in the pilot study section. However, based on Romero et al. (2021) work, the printing parameters which should obtain the best water tightness are presented in table 2.4.

Post-print processing, commonly referred to as post-processing, is a critical step to consider for ensuring the durability and functionality of 3D-printed cardiac phantoms. Among the various approaches available, two promising methods will be systematically evaluated in the upcoming pilot study: the application of acrylic lacquer and the use of a new chemical sealant called Dichtol AM Hydro.

| Parameter | Specification |
|---|---|
| Layer Height | 0.1-0.12 mm |
| Wall Thickness | 3-4 mm |
| Number of Perimeters | 4-8 |
| Top Shell Layers | 8-10 |
| Bottom Shell Layers | 8-10 |
| Solid Infill | 100% |
| Printing Speed | 50-100 mm/s |
| Supports | Only if needed |
| Extrusion Multiplier | 1.01 - 1.10 |
| Outer Wall Line Width | 0.5 mm |
| Inner Wall Line Width | 0.5 mm |
| Top Surface Line Width | 0.5 mm |
| Seam Position | Random |
| Infill Overlap | Activated |
| Vase Mode | Activated |

Table 2.3: Printing parameters and optimizations to be evaluated

| Parameter | Specification |
|---|---|
| Perimeters | 4 |
| Extrusion Multiplier | 110% |
| Extrusion Temperature | 225 |
| Layer Height | 0.16 mm |
| Print Speed | 50 mm/s |

Table 2.4: Proposed Parameters

Acrylic lacquer is straightforward to apply and effectively creates a waterproof layer on the surface of the print. In contrast, Dichtol AM Hydro offers an additional advantage; it not only forms a protective waterproof layer but also penetrates and fills any microscopic gaps within the print. This process seals the print more comprehensively, addressing potential vulnerabilities both on the surface and within the layers.

## 2.8 | Conclusion

This chapter presented a comprehensive review of the existing literature relevant to the development and application of 3D-printed phantoms in nuclear medicine, particularly focusing on myocardial perfusion imaging and advancements in imaging technologies such as SPECT and MyoSPECT. By exploring various approaches and techniques from previous studies, such as those by Kiss et al. (2022), Jasmat (2022), and Green and Grice (2022), this review highlighted the significant progress made in customizing phantoms for clinical use, while also addressing the challenges and innovations in phantom fabrication. In the next chapter, the research methodology used in this study will be discussed, detailing the processes and techniques implemented to achieve the objectives outlined.

# 3

# Research Methodology

## 3.1 | Introduction

This chapter presents the research methodology used in the study. The research methodology was designed to ensure that the objectives of the study are comprehensively addressed. It consists of a research approach, research strategy, data collection techniques, data collection procedures, data collection tools, and data analysis techniques. In this study, the research approach was a mixed-methods approach, combining both qualitative and quantitative methods. The research strategy employed was primarily experimental and comparative. The data collection technique involved direct observation of experiments and tests conducted on the 3D-printed cardiac phantoms. The data collection procedure included systematic observation during fabrication, post-processing, and imaging of phantoms. The data collection tools utilised were various physical instruments, i.e. the gamma cameras and dose calibrators, alongside specialized software for image reconstruction and analysis. The data analysis was performed using GE Healthcare's Xeleris 4 focusing on qualitative and quantitative assessments of image quality and defect detection.

## 3.2 | Research Approach

This research largely employs a mixed-methods research approach to accomplish its objectives. These include evaluating imaging technologies, creating anthropomorphic phantoms, and iden-

tifying the best 3D printing materials and parameters. This method provides objective responses to the research questions by measuring the phantoms' physical characteristics, image quality, and performance under various conditions.

The creation of several cardiac phantoms is another method the study uses to identify the ideal printing parameters and post-printing techniques to waterproof models. Hence, the impact of the changes made between each 3D-printed phantom was carefully evaluated during the pilot study phase of this research. The study also assesses improvements in image quality offered by CZT detectors over traditional SPECT systems and compares the performance of the 3D printed phantom with the department's existing model.

Qualitative approaches are taken into consideration for insights into practical usability and clinical relevance, even if quantitative methods are the main focus for capturing objective performance measures (Borrego et al., 2009). The results are enhanced by this mixed-methods approach.

## 3.3 | Research Strategy

The research strategies for this study are primarily experimental and comparative. The experimental aspect involves systematically varying 3D printing parameters—such as material type, extrusion temperature, layer height, and print speed—to determine the optimal conditions for creating durable, watertight cardiac phantoms. This experimental approach is crucial for addressing the objectives of determining the best materials and parameters for 3D printing and fabricating anthropomorphic hearts.

This study is prospective in nature, focusing on testing predefined hypotheses about the quality and performance of the 3D-printed phantoms. The prospective design allows for the controlled investigation of how different variables influence the phantoms' final properties, making it possible to draw clear conclusions about the best practices for 3D printing phantoms.

The study also includes a comparative analysis, specifically comparing the performance of the new 3D-printed phantom with existing models, i.e. the department's current cardiac phantom and the phantoms produced by Kiss et al. (2022). This comparison under identical or at least very similar imaging conditions is critical for evaluating improvements in image quality and defect detection capabilities, particularly when assessing the benefits of CZT detectors over conventional gamma camera SPECT systems. Furthermore, this comparison facilitates the evaluation of the improvements with the modified and improved printing parameters.

## 3.4 | Data Collection Technique

The data collection in this study was primarily conducted using a direct observation technique. This approach involved systematically observing and recording the outcomes of various experiments and tests performed on the 3D-printed cardiac phantoms. The direct observation technique was chosen for its ability to provide detailed, firsthand data on the physical properties and imaging performance of the 3D-printed phantoms.

The first part of the data collection technique, which will be further explained in the pilot study section, involved direct observation of the experiments conducted to investigate the optimal material and parameter selection. Observations were made during the fabrication process to note any anomalies or challenges encountered during printing. Once the prints were satisfactory, they moved to the post-processing stage, where they were subjected to further testing to observe properties such as water tightness, structural integrity, and surface smoothness.

Once the phantoms were ready for imaging, the comparative observation part of the study was conducted. First, the department's standard cardiac phantom, produced by Spectrum Dynamics, was imaged to compare it with the 3D-printed phantom of a normal heart. Both phantoms were administered the same dose of 4 MBq (decay corrected values are provided in tables 4.2 and 4.3) and were imaged first on the MyoSPECT and then on the NM/CT 870 DR SPECT. These phantoms were imaged under standard imaging conditions, i.e., 7 minutes on the MyoSPECT and 13

minutes on the SPECT. The phantoms were set up on the MyoSPECT and the SPECT as seen in figures 3.3 - 3.4.

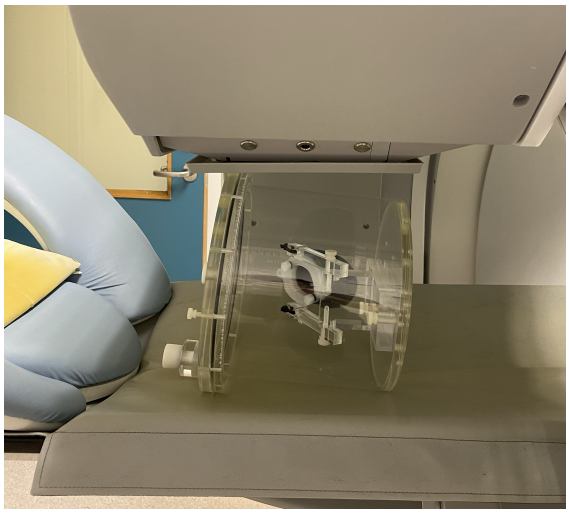

Figure 3.1: 3D-printed phantom in MyoSPECT

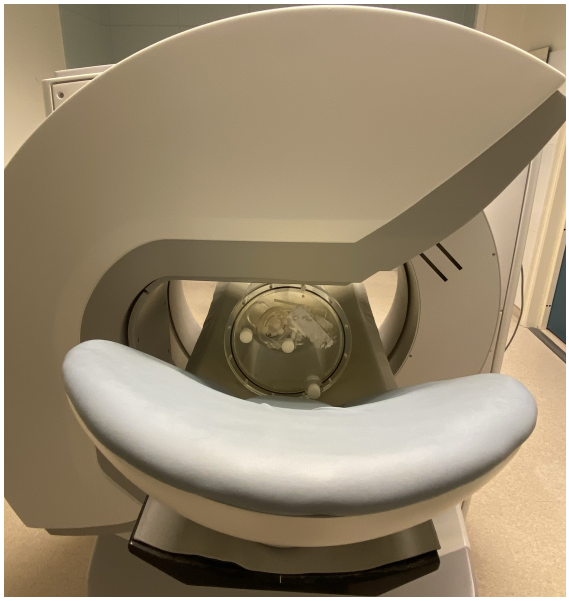

Figure 3.2: Data Spectrum Cardiac phantom in MyoSPECt

Following this, the next comparative observation was conducted to compare the images of the 3D-printed phantom with those of Kiss et al. (2022). For this, 6 MBq of activity was injected into both the 3D-printed normal heart and the defective heart. Kiss et al. (2022) reported a decay-corrected activity of 13.82 MBq in the normal heart and 11.39 MBq in the defective heart. However, based on research and practices adopted in Malta, this level of uptake is considered too high. To better represent actual clinical conditions, Boschi et al. (2022)'s recommendations were followed. According to this research, Boschi et al. (2022) explained that 1 hour post-administration, only 1-1.4% of the administered dose would be present in the heart. Therefore, both phantoms were administered 1% of 600 MBq, which is the maximum dose given to patients in Malta (these are patients undergoing the 1-day protocol). With the activity administered, imaging was then conducted on the NM/CT 870 DR only, as Kiss et al. (2022) conducted their tests on a SPECT system.

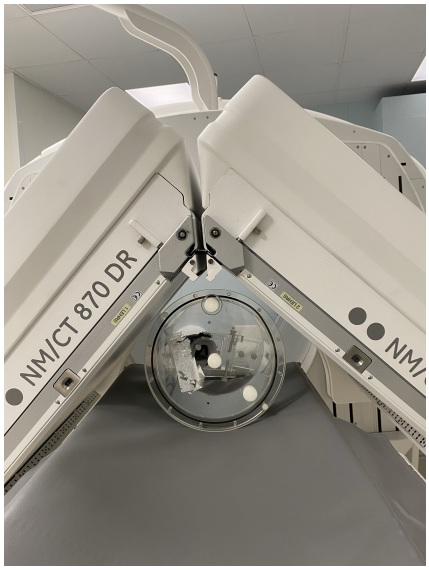


Figure 3.3: 3D-printed phantom in NM/CT 870 DR

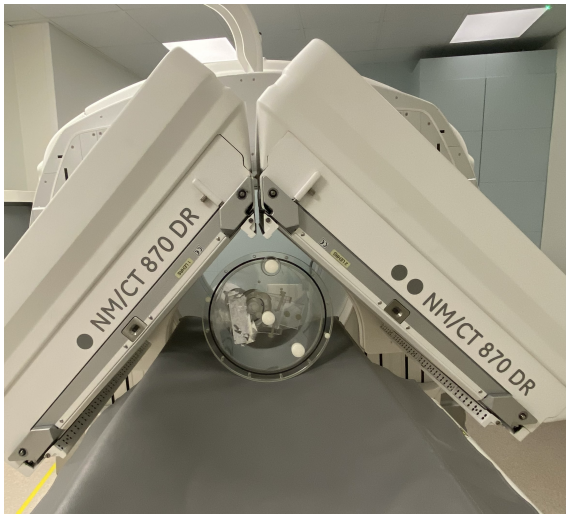


Figure 3.4: Data Spectrum Cardiac phantom in NM/CT 870 DR

The department's NM/CT 870 DR SPECT system, equipped with a Low Energy High Resolution and Sensitivity (LEHRS) collimator, was used for imaging. This differed from the machine used by Kiss et al. (2022), which was the AnyScan® DUO FLEX SPECT/CT system equipped with a Low Energy High-Resolution (LEHR) collimator.

Following these initial comparisons, the defective phantom, which had an initial activity of 6 MBq, was allowed to decay. Scans were then taken periodically, thanks to the relatively short half-life of Technetium, as the activity decayed to 5, 4, 3, and 2 MBq, respectively. These scans were performed on both the MyoSPECT and the SPECT systems to compare each machine's ability to represent the shape and defect in the heart at different activity levels.

Finally, a comparison between an ultra-low dose of 200 MBq, a normal dose of 400 MBq, and a high dose of 600 MBq was conducted on both machines, this time using the normal heart 3D-printed phantom. This was done to further evaluate any differences between the two machines.

Alternative techniques, such as using the well-established NM Monte Carlo simulator, GATE,

were considered. GATE (Geant4 Application for Tomographic Emission) is an open-source software that could have been used to simulate expected outcomes with the 3D-printed anthropomorphic phantom (OpenGATE, 2022). Additionally, it could have been employed to verify the results obtained after imaging (Jan et al., 2004; Sarrut et al., 2021).

## 3.5 | Data Collection Procedure

Within this section, the data collection process will be explained. Thus, it also includes an explanation of the equipment setup.

### 3.5.1 | Cardiac Phantom

The cardiac phantom previously developed by Kiss et al. (2022) was manufactured, studied, and optimised. This phantom was chosen as it allowed for a direct and identical comparison with the department's current cardiac phantom and with one that is already present in current literature on the topic. Furthermore, it allowed the focus to be shifted to the main aim of the dissertation; i.e. the optimization and manufacturing of the 3D-printed phantom.

### 3.5.2 | Printer

Choosing the right printer for the job was crucial to the research. Three different types of printers were available for use. These were the Original Prusa i3 MK3S+, a Bambu Lab P1S, a Bambu Lab A1 mini an Ultimaker S5.

The Prusa and Bambu Lab printers were used for the prototyping and the pilot study phase of the study. Whilst the Ultimaker printer was used for both the pilot study phase and final printing phase.

All of these printers had to be FDM printers, have dual or at least single extrusion, have great print quality, safe, affordable and be as user friendly as possible. This ensures replication of the

study. As when reviewing similar works certain authors used SLA based printers, which are more expensive, more complicated to use and might even emit toxic fumes which would require separate ventilation systems to ensure the safe operation of the printers. All printers used a 0.4 mm nozzle.

All printers were either serviced, or calibrated and cleaned prior to starting the pilot study phase and even more importantly the final printing stage. No extra modifications were needed on any of these printers since the material of choice was clear-PETG.

### 3.5.3 | Material

As explained in the literature review the material of choice was PETG as it offered the best water retention properties. Two different PETG filaments were acquired with different diameters. As the Bambu Lab and Prusa printers are compatible with the typical 1.75 mm filaments, whilst the Ultimaker is only compatible with 2.25 mm filaments. Hence, the Prusament PETG was used with the Bambu Lab and Prusa printers whilst Ultimaker's PETG was used with the Ultimaker 5S printer.

### 3.5.4 | Slicing Software

The dedicated software for each printer was used to convert the STL files into G-code, ensuring the best compatibility and print quality. PrusaSlicer was utilized for the Prusa printer, Ultimaker Cura for the Ultimaker printer, and Bambu Studio for the Bambu printer. Using each printer's specific software allowed for seamless integration and precise control over the advanced printing parameters required. This ensured that the prints met the desired quality standards. The software also offered features for refining the model and optimizing print settings, providing the best possible print results for each system.

### 3.5.5 | Pre-Processing Software

Prior to printing the phantom some pre-processing work was required. This was done to make the print more watertight and thus reduce the post-print processing needs. Figure 3.5 is a flow diagram which shows why this is such a fundamental step in printing process.

The face reduction and pre-processing software used were Autocad's Meshmixer and Fusion 360 respectively. Their ease of use and freely available online tutorials made them the most attractive choices for the job.

### 3.5.6 | Radionuclide Used

As outlined in the literature review, Technetium-99m was selected for imaging the phantoms, as it is the standard radionuclide used for cardiac imaging in Malta's Nuclear Medicine department. This selection ensures the replication of clinical scenarios.

## 3.6 | Phantom Fabrication Method

In this subsection, the methodology used to create the phantom for this study is discussed. This section is intended to help the reader gain a better understanding of the procedures outlined in the previous sections. Furthermore, to better understand the process, figure 3.5 which is a flow-chart of the process was also designed. This section is a step-by-step explanation of figure 3.5.

This subsection elaborates on the methodology used to construct the phantom for this study. It is designed to clarify the procedures outlined in the previous sections. Additionally, figure 3.5, which presents a flowchart of the process, is included to enhance understanding. This section provides a detailed, step-by-step explanation of figure 3.5.

The first step into fabricating the phantom was the data acquisition phase. When reviewing figure 2.9 and comparing it to figure 3.5 one should note that that there were two possible paths which

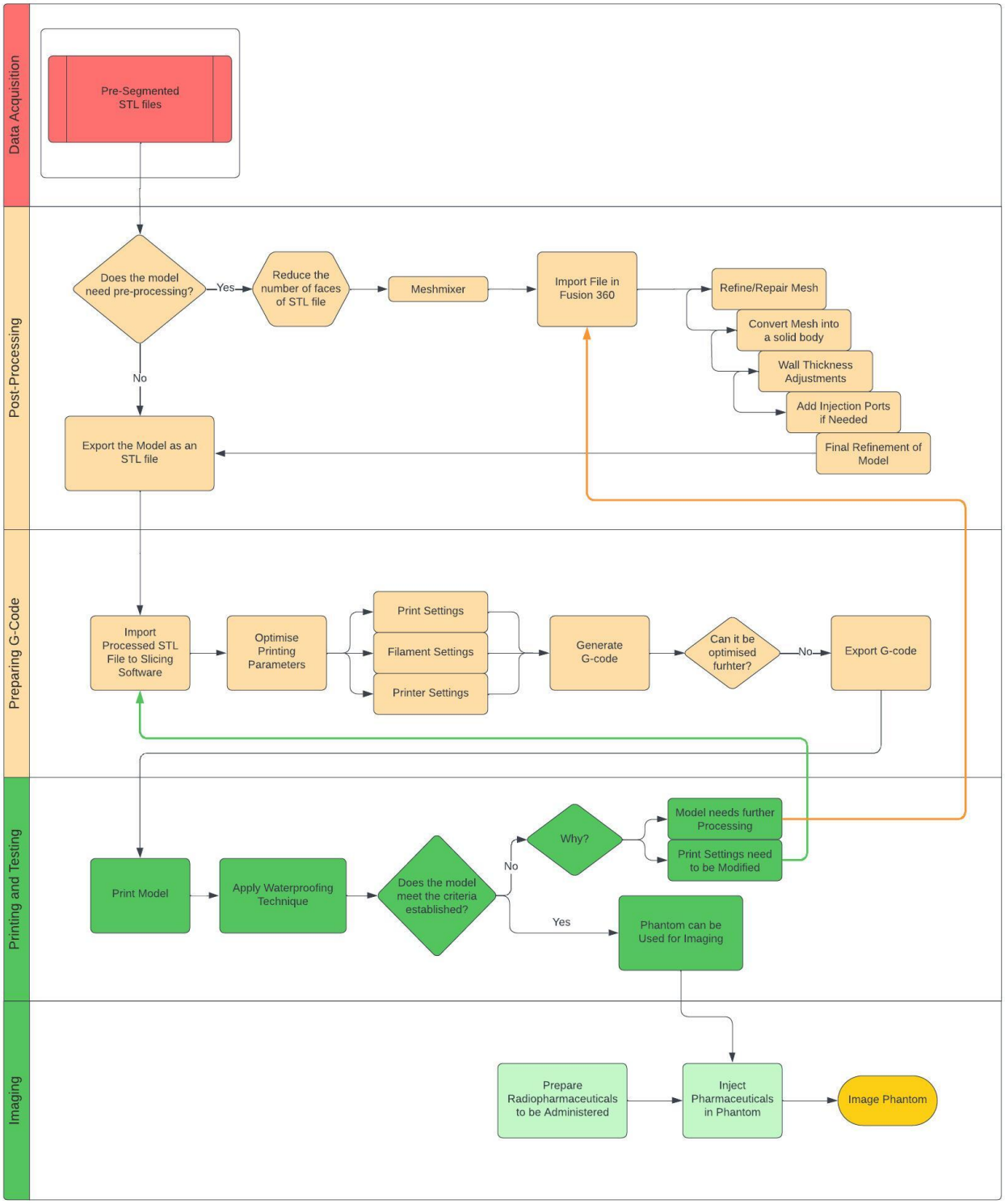


Figure 3.5: Phantom Fabrication Method

could have been taken.

The first path required the acquisition of CT, MRI, or SPECT/CT images. These images would require segmentation using slicing software, followed by exportation as an STL file for subsequent post-processing. The STL file would then undergo additional refinements in Fusion 360 to transform it into the desired model.

Rather than following the initial path, the phantom developed by Kiss et al. (2022) was investigated. This approach presented several advantages. Firstly, it facilitated precise replication of the imaging scenarios used with the department's existing NM cardiac phantom, as it is designed to fit into the Data Spectrum cardiac phantom holder. Secondly, this choice shifted the focus towards refining the 3D printing process and the phantom's fabrication, enabling further optimisation and deeper understanding of the requirements for 3D printing a phantom. Thirdly, it allowed for the assessment of producing in-house phantoms through 3D printing as opposed to purchasing them.

The model required some post-processing to ensure it was watertight. The model, provided by Kiss et al. (2022), along with his instructions for printing the phantom, necessitated post-print modifications. Hence, adjustments were made to both the phantom design and the printing parameters to try and make the print watertight without needing any post-print-processing.

After refining the STL file during the post-processing phase, it was imported into various slicing software applications, tailored to the specific printers being used. Each software offered unique advantages and drawbacks. Bambu Studio and Prusaslicer were the most user-friendly options. All software options permitted identical modifications to the printing parameters, meaning the primary distinction among the printers lay in the print quality they could achieve. All of these software then exported a file known as the G-Code which contained all the instructions needed to print the model.

The printing and testing phase then followed. This phase will be discussed in detail during the

pilot study phase. Several prints were printed and evaluated to determine the best printing parameters before printing the right model in the quantity required. All final prints were conducted on the Ultimaker 5S as it had the best printing quality out of all three printers. This was then followed by the waterproofing technique.

The waterproofing technique used for the phantoms which were imaged, consisted of the application of three sets of acrylic layers which were sprayed on the print. With one hour of drying time in between each one. This completely ensured that the print was waterproof.

Following this procedure, the prints were re-evaluated using the same waterproofing test employed during the pilot study, as adopted by Romero et al. (2021). Upon completion of this process, the 3D-printed phantoms were ready to be used for imaging.

## 3.7 | Data Collection Tool

This section will discuss the tools used to collect the data. Both physical instruments and dedicated software were used to extract the data from the images obtained. All of the tools mentioned in this section were validated and/or calibrated prior to acquiring and analysing the images.

### 3.7.1 | GE MyoSPECT

Half of the data was acquired using the GE MyoSPECT Gamma Camera. The phantom was positioned on the couch according to standard phantom positioning protocols to ensure consistent replication when changing the phantom with different doses. The machine was calibrated that morning through a daily quality control (QC) process. This QC process included checks for uniformity, energy resolution, and system sensitivity, ensuring the gamma camera operated as expected.

### 3.7.2 | GE NM/CT 870 DR SPECT/CT Sytem

The second half of the data was acquired on GE's SPECT/CT system. The phantom was placed in an identical position and orientation as when placed in the MyoSPECT. This allowed for fair comparisons between the two machines. The SPECT system was oriented in an L-mode setup, with the collimators of choice being GE's new LEHRS collimator. Like the MyoSPECT, the SPECT system also underwent a thorough daily QC process to ensure accurate and reliable performance.

### 3.7.3 | Dose Calibrator

The CRC-55tR dose calibrator was used to measure the radioactivity injected into the phantom. Initially, the radioactivity was drawn into a syringe, which was then placed in its designated holder to ensure geometric consistency between measurements. Prior to taking the first reading the dose calibrator was calibrated to account for background radiation. This dose calibrator had an uncertainty value of $\pm 2\%$.

### 3.7.4 | Software

Image reconstruction was performed using GE Healthcare's Xeleris 4 software, a platform designed for nuclear medicine purposes. The QGS/QPS tool was used to process, reconstruct, and export the cardiac images of each different scan conducted. The polar maps, SA, VLA and HLA views of each scan were obtained through this software.

### 3.7.5 | Activity injected into the phantom and decay correction

Based on Boschi et al. (2022)'s recommendations, the activity administered was set to 1% of each simulated case as outlined in the data collection technique section. This simulates the amount of activity that would be present in the heart one hour post-administration.

However, it is important to note that obtaining the relatively low doses required from a Technetium generator was challenging. This is particularly the case when the technetium has just been

eluted or if the generator is newly acquired.

Moreover, acquiring the correct amount of activity is not the final step. When injecting the activity into the phantom, some of it inevitably remains in the syringe itself, and this residual activity must be accounted for when determining the actual amount of activity present in the phantom.

Finally, it is also important to consider the decay of the activity at the time of acquisition. The activity at the time of acquisition was determined through the standard equation:

$$N(t) = N_0 \cdot e^{-\lambda t} = N_0 \cdot e^{-(ln2/t_{1/2})t} \tag{3.1}$$

Where:
$N(t)$ is the amount of radioactive material at time $t$
$N_0$ is the initial amount of radioactive material,
$\lambda$ is the decay constant and
$t_{1/2}$ is the half-life of radioactive material used
Since Technetium 99m was used its half-life was 6.01 hours

These calculations were then conducted for every scan. Thus, the decayed corrected activity can be found in tables 4.2 and 4.3.

## 3.8 | Data Analysis Technique

This section outlines the analysis techniques used to obtain the results and images presented in the results section. Each subsection below details a specific step of the process.

All acquisitions were processed using the GQS/QPS tool in the Xeleris software at the Nuclear Medicine department. To evaluate the scans, the heart was oriented as shown in figure 3.6. Individuals experienced in nuclear medicine cardiac imaging will immediately recognize that the heart's orientation is not in its typical anatomical position. This represents a limitation, which will

be further discussed in the relevant section. However, using the orientation features available in the QGS/QPS tool, the heart was artificially aligned to the standard position for analysis.

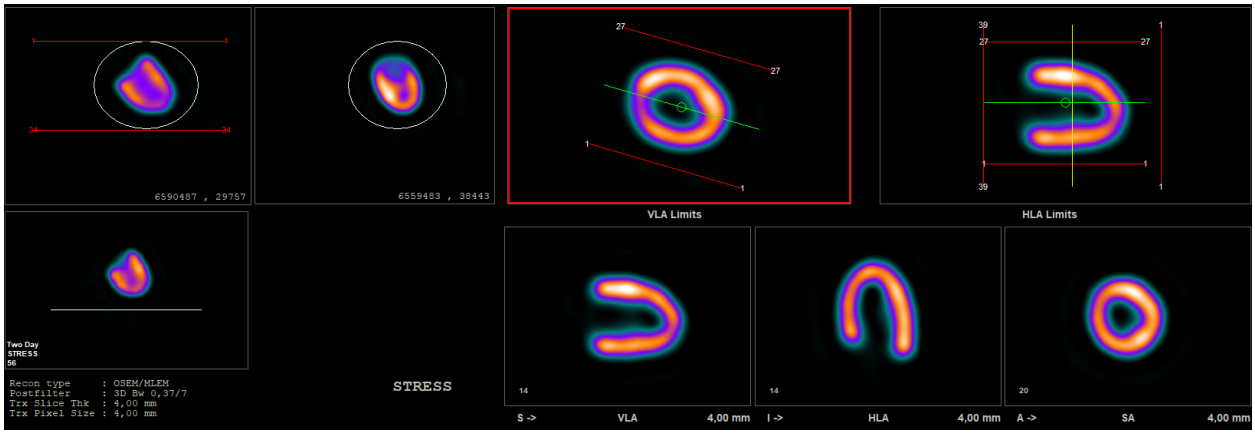


Figure 3.6: Orientation of the heart in Xeleris - QGS/QPS software

Once the orientation and position of the heart were satisfactory, the QGS/QPS system generated the polar maps along with a series of SA, VLA, and HLA views for each scan as seen in appendix c.

To enable the necessary comparisons and analyses required to meet the objectives of this project, a polar map of the vascular regions was first obtained. This step was crucial for ensuring consistent orientation across scans, allowing for accurate comparisons.

After confirming the heart's orientation, a polar map with 17 segments was acquired for each image, facilitating a quantitative comparisons of all the different regions between the scans.

Finally, to further evaluate and compare the image quality of the MyoSPECT and the SPECT systems, the best views from the SA, VLA, and HLA perspectives were selected. This allowed for a direct comparison between the two machines at different doses for both the normal and defective phantoms.

## 3.9 | Pilot Study

This section provides a detailed explanation of the pilot study conducted to 3D-print the phantoms used in this study. Each subsection within this section will give an overview of the different steps and approaches taken to address various challenges.

### 3.9.1 | Initial Choice of Printing Parameters

Before starting the printing process, an extensive literature review was conducted. The outcome of the print heavily depends on the chosen printing parameters, often requiring a compromise between speed and quality. This review guided the selection of printing parameters, based on those used by Green and Grice (2022); Kiss et al. (2022); Kočí (2021, 2024); O (2023); Romero et al. (2021).

Through the evaluation of their work, optimal configurations were identified within the ranges listed in table **??**. Additionally, a proposed parameter table, which is table 2.4 was provided in the literature review, offering excellent guidelines to begin with. These configurations were not overly demanding for any printer, meaning that all three available printers could potentially achieve prints with these settings.

### 3.9.2 | Choice of Material

As discussed in the literature review, PETG was chosen as the material of choice for achieving the necessary waterproofing. However, due to delays in acquiring the material, PLA was sometimes used to conserve the remaining PETG from previous projects.

Using both materials, the phantom was printed multiple times to test and refine potential improvements. This step was crucial for determining the optimal parameters when transitioning to just PETG printing, as the two materials share similar properties during the printing process.

### 3.9.3 | Choice of Printer

The availability of three printers proved invaluable for this project. The prototyping stage was initially conducted using the Prusa and Bambu printers. The Bambu printer's superior printing speeds were mainly used for smaller attachments like screws and stands for the phantoms. All advanced and final prints were then conducted with the Ultimaker 5S printer.

#### 3.9.3.1 | Printing process on Prusa

The printing process on the Prusa printer began with PLA, using the configurations listed in table 3.1.

| Parameter | Specification |
|---|---|
| Perimeters | 8 |
| Extrusion Multiplier | 110% |
| Extrusion Temperature | 225 |
| Layer Height | 0.1 mm |
| Print Speed | 50 mm/s |
| Solid Infill | 100% |

Table 3.1: Test 1 - Parameters

This print encountered issues immediately. To attempt to solve the problem, the extrusion multiplier, which needs to be as high as possible to fill any gaps within the layers, was lowered to 105%. However, this was still too high, resulting in an overflow of material. This caused the print to fail as there was too much material extruding out of the extruder for it to layer on itself effectively. As a result, the extrusion multiplier was lowered again to 103%. This resulted in a print with bad printing quality as observed in figures 3.7 and 3.8.

The solution to fix this issue was to significantly reduce the printing speed. This would have extended the printing time too much, requiring the print to continue overnight. This approach was avoided because the printer had a tendency to overheat until it was serviced. As a result, printing was shifted to the Ultimaker printer.

Figure 3.7: Hole and inconsistencies in the sides of the phantom

Figure 3.8: Failed overhang to enclose phantom at the apex of the heart

#### 3.9.3.2 | Printing process on Ultimaker

Printing on the Ultimaker began with PLA. The same parameters used on the Prusa were applied to the Ultimaker, and the print quality was superior in all aspects, both visually and texturally. This print was produced with a 0.1 mm layer height and the standard 4 top and 4 bottom layers. However, it became evident that a finer layer height with more top and bottom layers was needed to fully enclose the phantom. An image of this print can be seen in Figure 3.9.

Encouraged by these results, a print was attempted with PETG. The first attempt used a 105% extrusion multiplier, but the print failed after just a few layers, partly due to the use of the wrong extruder—the BB extruder, which is primarily used for support materials, and already extrudes more material. The result of this print is found in figure 3.10.

Figure 3.9: First print on Ultimaker printer with PLA

Figure 3.10: Ultimaker - failed print because of bad extruder

As a result, the extrusion multiplier was reduced again to 103%. During this period, research on 3D printing microfluidic devices was conducted. Castaneda (2017) applied 3D printing to create microfluidic spherical capsules used in various nuclear and biomedical applications. The designs and specifications shared by Castaneda (2017) were integrated into the print parameters for this study. Hence, optimising the printing process further. Through this process the parameters were optimised as found in table 3.2.

Table 3.2: Printing parameters and optimizations to be evaluated

| **Parameter** | **Specification** |
|---|---|
| Layer Height | 0.05 mm |
| Wall Thickness | Fixed according to the shape of the heart |
| Number of Perimeters | 8 |
| Top Shell Layers | 8 |
| Bottom Shell Layers | 8 |
| Solid Infill | 100% |
| Printing Speed | 50-100 mm/s |
| Supports | Only if needed |
| Printing Temperature | 250°C |
| Bed Temperature | 85°C |
| Extrusion Multiplier | 103% |
| Outer Wall Line Width | 0.4 mm |
| Inner Wall Line Width | 0.4 mm |
| Top Surface Line Width | 0.4 mm |
| Seam Position | Random |
| Infill Overlap | Activated |
| Vase Mode | Activated |

When printing with these parameters, the result had significant stringing and partial inconsistencies as seen in figure 3.11.

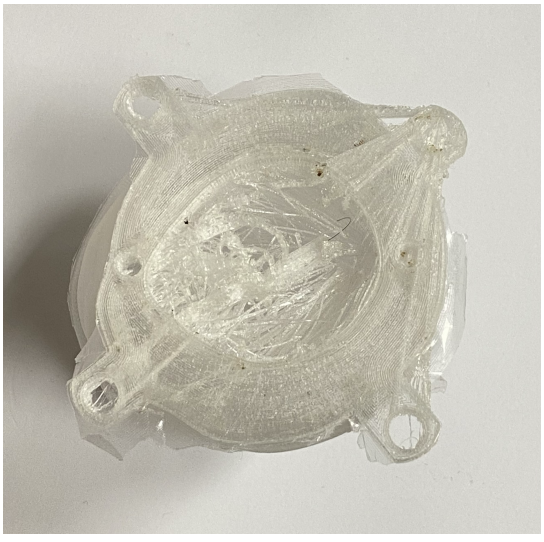

Figure 3.11: Ultimaker failed print because of a lot of stringing

As a result, a minor adjustment was made: the vase mode feature, although recommended by Kočí (2021), was deactivated. Thus, the final and optimized version of the parameters which were evaluated are represented in table 3.3.

Table 3.3: Printing parameters and optimizations to be evaluated

| **Parameter** | **Specification** |
|---|---|
| Layer Height | 0.05 mm |
| Wall Thickness | Fixed according to the shape of the heart |
| Number of Perimeters | 8 |
| Top Shell Layers | 8 |
| Bottom Shell Layers | 8 |
| Solid Infill | 100% |
| Printing Speed | 50-100 mm/s |
| Supports | Only if needed |
| Printing Temperature | 250°C |
| Bed Temperature | 85°C |
| Extrusion Multiplier | 103% |
| Outer Wall Line Width | 0.4 mm |
| Inner Wall Line Width | 0.4 mm |
| Top Surface Line Width | 0.4 mm |
| Seam Position | Random |
| Infill Overlap | Activated |
| Vase Mode | Deactivated |

It is also important to note that the Ultimaker's glass build plate chipped during the removal of two of the prints using these parameters. Further evaluation on how to mitigate this issue is recommended.

### 3.9.4 | Post-Processing

Once printed, the model had to undergo post-processing techniques. The processes required during this stage would vary depending on the model, as different models might need different types of support. The post-processing requirements also varied depending on the printer used, as different printers have different capabilities, and from one 3D-printing technique to another. For example, SLA prints would require more post-printing processes to further cure and clean the

print compared to FDM based prints.

Thanks to the simplicity of the model and the capabilities of the Ultimaker printer, all 3D-printed models did not need any support, only a brim to keep them adhered well to the bed during printing. Therefore, the only thing that needed to be removed was the brim at the base of the print.

### 3.9.5 | Waterproofing

Two waterproofing techniques were tested. First, all prints were sprayed with a layer of acrylic paint as instructed on the spray bottle. The spray was applied from a distance of 10-25 cm. It was left to dry for one hour and then another coating was applied. This step was repeated a total of three times to ensure that an even coating of acrylic paint was sprayed on the model.

The other method tested used a chemical called Dichtol AM Hydro. This chemical works differently from acrylic paint; instead of sealing the model from just the outside layer, it penetrates microscopic gaps and solidifies within them. Essentially, it impregnates all gaps, sealing each layer of the print, not just the external one. This technique required the model to be dipped in the solution for 10-15 minutes as instructed and left to dry for 24 hours before undergoing the waterproofing test adopted by Romero et al. (2021).

Figure 3.12 displays two phantoms: the one on the left was waterproofed using the impregnation technique, while the one on the right employed the acrylic technique. Notably, the phantom treated with the acrylic method exhibits a glossier finish, which may pose challenges for visibility during liquid filling due to reduced transparency.

To assess the watertightness of each vessel, a digital scale, a plate, and a sheet of absorbent paper were utilised. The procedure began by placing the plate on the scale and taring it after adding the absorbent paper. Next, the processed phantom was placed on the paper, and the water was carefully added using a syringe. After a period of 7 hours, the vessel was removed, and the weight

Figure 3.12: Impregnation vs acrylic technique

displayed on the digital scale was recorded. No value was observed on the scale from all models. Showing that no water leaked through this method.

The impregnation technique was determined to be superior due to its ease of application and higher effectiveness in waterproofing the phantom.

## 3.10 | Ethical Considerations

This study has been approved by the University Research Ethics Committee of the University of Malta. Ethical considerations were carefully observed throughout the research process to ensure

compliance with ethical standards and safety protocols. No patient data was obtained or used in this study, as the research focused solely on the production and imaging of a 3D-printed cardiac phantom provided by Kiss et al. (2022).

To ensure the safe handling of radioactive materials, all operations involving radioactivity were conducted by Mr Agius, the supervisor of the thesis, as formal training on generator operations and procedures in the hot lab had not yet been received. A dosimeter was worn at all times during the handling and imaging processes to monitor radiation exposure. The study adhered to strict radiation safety protocols to minimise any potential risks associated with the use of radiopharmaceuticals and imaging equipment, upholding the highest standards of ethical conduct.

## 3.11 | Limitations of the research methodology

As with any study, this research had its limitations. However, by recognising these early on, their impact was minimized as much as possible.

One limitation was the exclusive use of FDM-based printers. Although FDM printers provided good results, resin-based printers, known for their superior resolution, could have produced even finer details. Comparing the high-resolution FDM prints from this study with the potentially higher resolution outputs from resin printers would have been beneficial.

The Prusa printer was having overheating issues. As a result, unsupervised prints were not attempted. This limited the the pilot study phase with the Prusa to a maximum of 10 hours. i.e the print would be placed as early as possible and would be completed by the end of the day.

The materials compatible with the Prusa and Bambu printers did not arrive in time, limiting their use to the prototyping phase. These printers, while more accessible to a broader range of users, have slightly inferior printing capabilities compared to the Ultimaker 5S. It would have been valuable to see if they could achieve results comparable to that of the Ultimaker.

Environmental factors, such as fluctuations in temperature and humidity during printing or imaging, could have affected the quality of the 3D-printed phantoms. This was mitigated as best as possible by controlling the environment with an AC.

Although the 3D-printed phantom was watertight, issues arose with the screws used to seal the filling openings. The screws performed well at certain temperatures, but in the colder SPECT/CT room, they contracted, causing small leaks. Larger screws were printed, but they didn't fit properly when handled in warmer environments. This issue could have been mitigated by cooling the larger screws before use to ensure a proper seal.

As a result of these sealing issues, the phantom's orientation had to be adjusted when placed in the Jaszczak phantom for SPECT/CT imaging. The heart within the phantom was positioned differently than it would be anatomically in a patient, necessitating artificial reorientation during image analysis. This mismatch in positioning could affect the consistency and comparability of the images with that of Kiss et al. (2022) and with that of real patients.

The study did not assess the durability and performance of the phantoms over extended periods or with repeated use, which is critical for understanding the practical longevity and cost-effectiveness of using 3D-printed phantoms in clinical practice.

Inconsistencies in the preparation and handling of the radiopharmaceuticals could have introduced variability in the imaging results. Additionally, the timing of imaging after decay correction may have led to data variability, especially if the decay was not accurately accounted for during each session. This was mitigated as much as possible by using the same techniques and by adhering to the planned scanning times as much as possible.

The research did not account for patient-specific variables like cardiac motion or diaphragmatic movements. Additionally, the experiments were carried out in air, meaning the study did not

simulate the body's composition, which would have influenced the radiation attenuation from the phantom in a more realistic setting

Finally, the study did not utilise Monte Carlo simulations (e.g., GATE) to verify the results, which could have provided additional validation of the experimental outcomes.

## 3.12 | Conclusion

Finally, this chapter has provided a comprehensive overview of the research methodology utilized to address the research questions and meet the study's objectives. The chosen methods were well-aligned with the goals of the research and were effectively implemented. The upcoming chapter will present and analyze the results, followed by an in-depth discussion.

# 4

# Results

## 4.1 | Introduction

This chapter presents the results obtained from the various imaging scans and experiments conducted throughout this study. The results are organized according to the study's objectives, providing a clear overview of how each objective was addressed. Quantitative data, including decay-corrected activity measurements and regional uptake values, are provided to support the findings. These results will be further analyzed and discussed in the following chapter to draw meaningful conclusions and highlight the significance of the study's outcomes.

## 4.2 | Optimal 3D-printing parameters to print and fabricate a waterproof nuclear medicine cardiac phantom

The first and second objectives of this study were to determine the best 3D printing materials and parameters to fabricate a cardiac phantom suitable for use in the NM department. Through the pilot study conducted, the parameters found in table 4.1 were determined to be best.

All prints used for imaging were produced using these parameters. The printing speed and layer height were adjusted to the lowest possible values to ensure a watertight print while maintaining a reasonable printing time. Transparent Ultimaker PETG was selected for its superior water reten-

Table 4.1: Final printing parameters

| **Parameter** | **Specification** |
|---|---|
| Layer Height | 0.05 mm |
| Wall Thickness | Fixed according to the shape of the heart |
| Number of Perimeters | 8 |
| Top Shell Layers | 8 |
| Bottom Shell Layers | 8 |
| Solid Infill | 100% |
| Printing Speed | 30 mm/s |
| Supports | Only if needed |
| Material | Ultimaker PETG |
| Printing Temperature | 250°C |
| Bed Temperature | 85°C |
| Extrusion Multiplier | 103% |
| Outer Wall Line Width | 0.4 mm |
| Inner Wall Line Width | 0.4 mm |
| Top Surface Line Width | 0.4 mm |
| Seam Position | Random |
| Infill Overlap | Activated |
| Vase Mode | Deactivated |

tion properties. After printing, the phantom underwent the post-processing steps detailed in the methodology.

By carefully selecting the appropriate parameters, materials, and post-processing techniques, the phantom shown in Figure 4.1 was successfully fabricated multiple times.

Figure 4.1: Fabricated 3D-printed cardiac phantom

## 4.3 | Collaboration with another 3D-printing project

Another objective of this study was to collaborate with another member of the research group. The phantom produced in this study had to be capable of being included in their phantom too. Which was an anthropomorphic phantom of the thoracic region of an obese patient. The phantom managed to fit in their phantom as shown in figure 4.2 and in the same orientation and position as one would find the left ventricle of the heart in a patient.

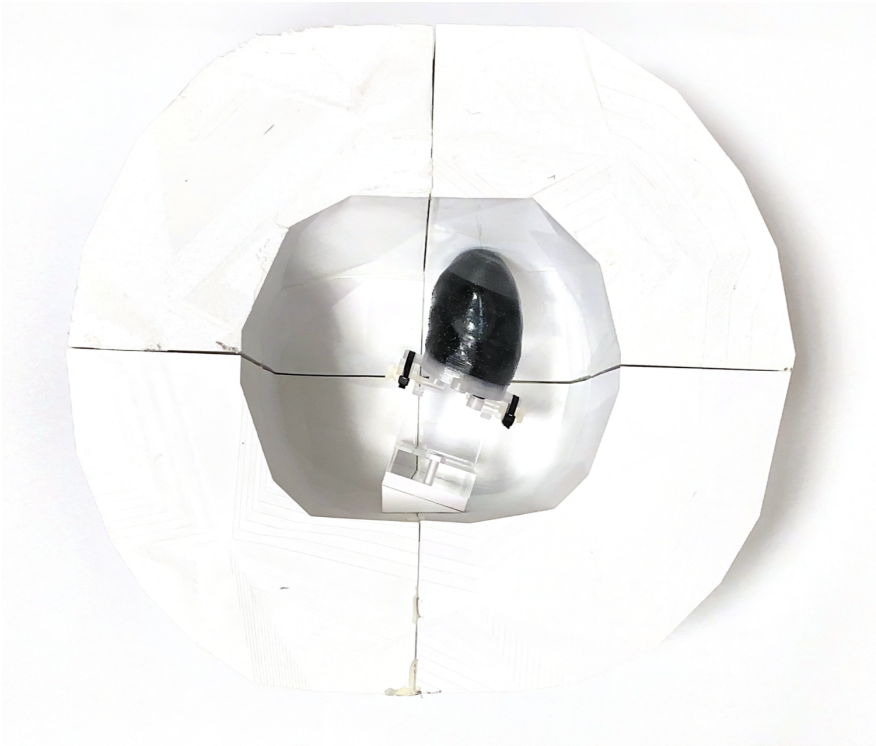

Figure 4.2: 3D-printed phantom in an anthropomorphic thoracic phantom of an obese patient

## 4.4 | Decay corrected activities of Technetium-99m

The following two subsections contain the decay-corrected activities at the time of acquisition for each scan. The first table represents the decay corrected values in the Data Spectrum Phantom and the 3D-printed heart phantoms. The second table contains the decay-corrected values present in the 3D-printed heart with the defect.

### 4.4.1 | Decay corrected activities in healthy heart phantoms

Table 4.2: Decay corrected activities of Technetium-99m in healthy heart phantoms at time of scan acquisition

| Scan Details | Activity in syringe pre-administration (MBq) | Residual activity in syringe post-administration (MBq) | Activity in phantom (MBq) | Time at administration of activity | Time at acquisition | Activity at time of acquisition (MBq) | Uncertainty (MBq) |
|---|---|---|---|---|---|---|---|
| Data Spectrum Phantom MyoSPECT | 4.2 | 0.329 | 3.871 | 13:40:00 | 13:59:00 | 3.73 | ±0.074 |
| Data Spectrum Phantom SPECT | 4.2 | 0.329 | 3.871 | 14:38:00 | 14:38:00 | 3.46 | ±0.069 |
| Low Dose Protocol MyoSPECT | 2.35 | 0 | 2.35 | 15:00:00 | 15:34:00 | 2.20 | ±0.044 |
| Low Dose Protocol SPECT | 2.35 | 0 | 2.35 | 15:00:00 | 15:43:00 | 2.16 | ±0.043 |
| Normal Dose Protocol MyoSPECT | 3.97 | 0.76 | 3.21 | 15:45:00 | 16:10:00 | 3.06 | ±0.061 |
| Normal Dose Protocol SPECT | 3.97 | 0.76 | 3.21 | 15:45:00 | 16:19:00 | 3.01 | ±0.060 |
| High Dose Protocol MyoSPECT | 6.35 | 0.228 | 6.122 | 15:05:00 | 15:27:00 | 5.87 | ±0.117 |
| High Dose Protocol SPECT | 6.35 | 0.228 | 6.122 | 15:05:00 | 15:51:00 | 5.60 | ±0.112 |

### 4.4.2 | Decay corrected activities in the 3D-printed hearts with the defect

Table 4.3: Decay corrected activities of Technetium-99m in heart phantoms with defect at time of acquisition

| Scan Details | Activity in syringe pre-administration (MBq) | Residual activity in syringe post-administration (MBq) | Activity in phantom (MBq) | Time at administration of activity | Time at acquisition | Activity at time of acquisition (MBq) | Uncertainty (MBq) |
|---|---|---|---|---|---|---|---|
| MyoSPECT 6 MBq | 6.87 | 0.448 | 6.422 | 08:00:00 | 08:30:00 | 6.06 | ±0.121 |
| MyoSPECT 5 MBq | 6.87 | 0.448 | 6.422 | 08:00:00 | 10:23:00 | 4.88 | ±0.098 |
| MyoSPECT 4 MBq | 6.87 | 0.448 | 6.422 | 08:00:00 | 12:32:00 | 3.81 | ±0.076 |
| MyoSPECT 3 MBq | 6.87 | 0.448 | 6.422 | 08:00:00 | 14:46:00 | 2.94 | ±0.059 |
| MyoSPECT 2 MBq | 6.87 | 0.448 | 6.422 | 08:00:00 | 17:27:00 | 2.16 | ±0.043 |
| SPECT 6 MBq | 6.87 | 0.448 | 6.422 | 08:00:00 | 08:08:00 | 6.32 | ±0.126 |
| SPECT 5 MBq | 6.87 | 0.448 | 6.422 | 08:00:00 | 10:34:00 | 4.78 | ±0.096 |
| SPECT 4 MBq | 6.87 | 0.448 | 6.422 | 08:00:00 | 12:42:00 | 3.73 | ±0.075 |
| SPECT 3 MBq | 6.87 | 0.448 | 6.422 | 08:00:00 | 14:55:00 | 2.89 | ±0.058 |
| SPECT 2 MBq | 6.87 | 0.448 | 6.422 | 08:00:00 | 17:35:00 | 2.13 | ±0.043 |

## 4.5 | Performance of the 3D-printed Cardiac Phantom

### 4.5.1 | Qualitative comparison

One of the objectives of this study was to evaluate the performance of the 3D-printed phantom. To evaluate this it was compared with the NM department's Data Spectrum Phantom. The results were organised as shown in figures 4.3 - 4.6 to facilitate this comparison. These figures provide a direct qualitative comparison between the polar maps and the different SA, VLA and HLA views obtained with both the SPECT and the MyoSPECT.

These are found on the next few pages.

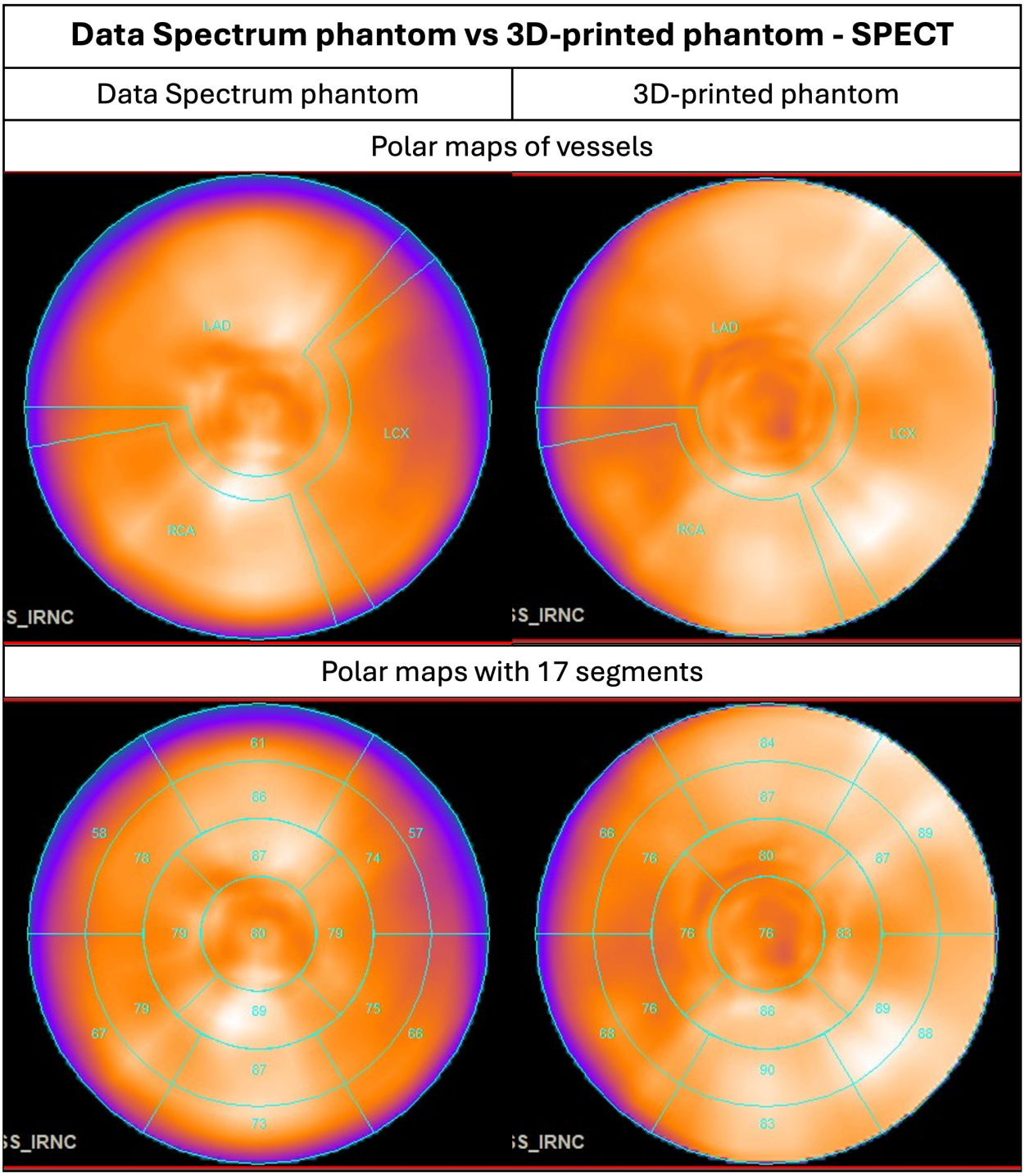


Figure 4.3: Polar maps obtained through imaging with SPECT

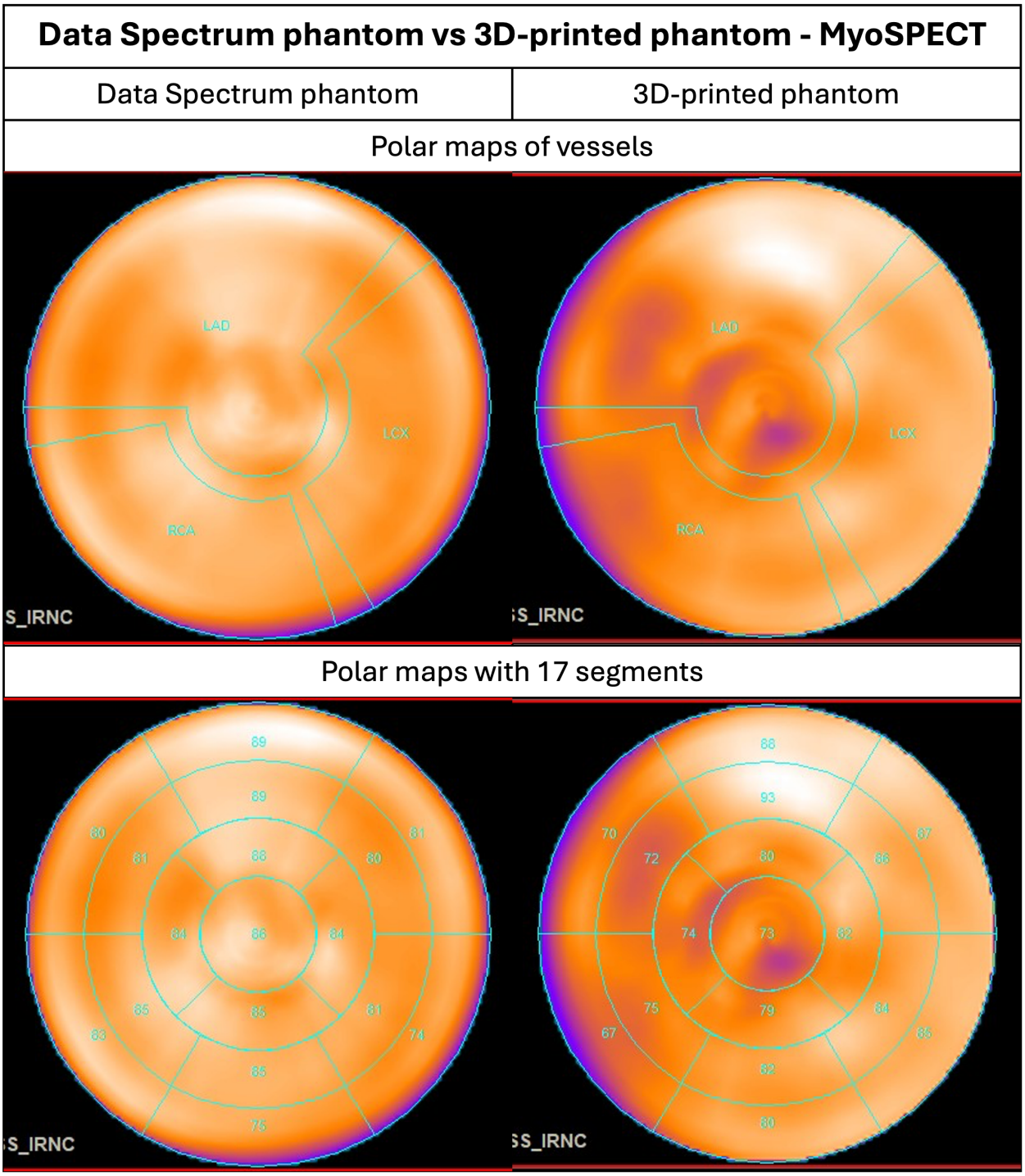


Figure 4.4: Polar maps obtained through imaging with MyoSPECT

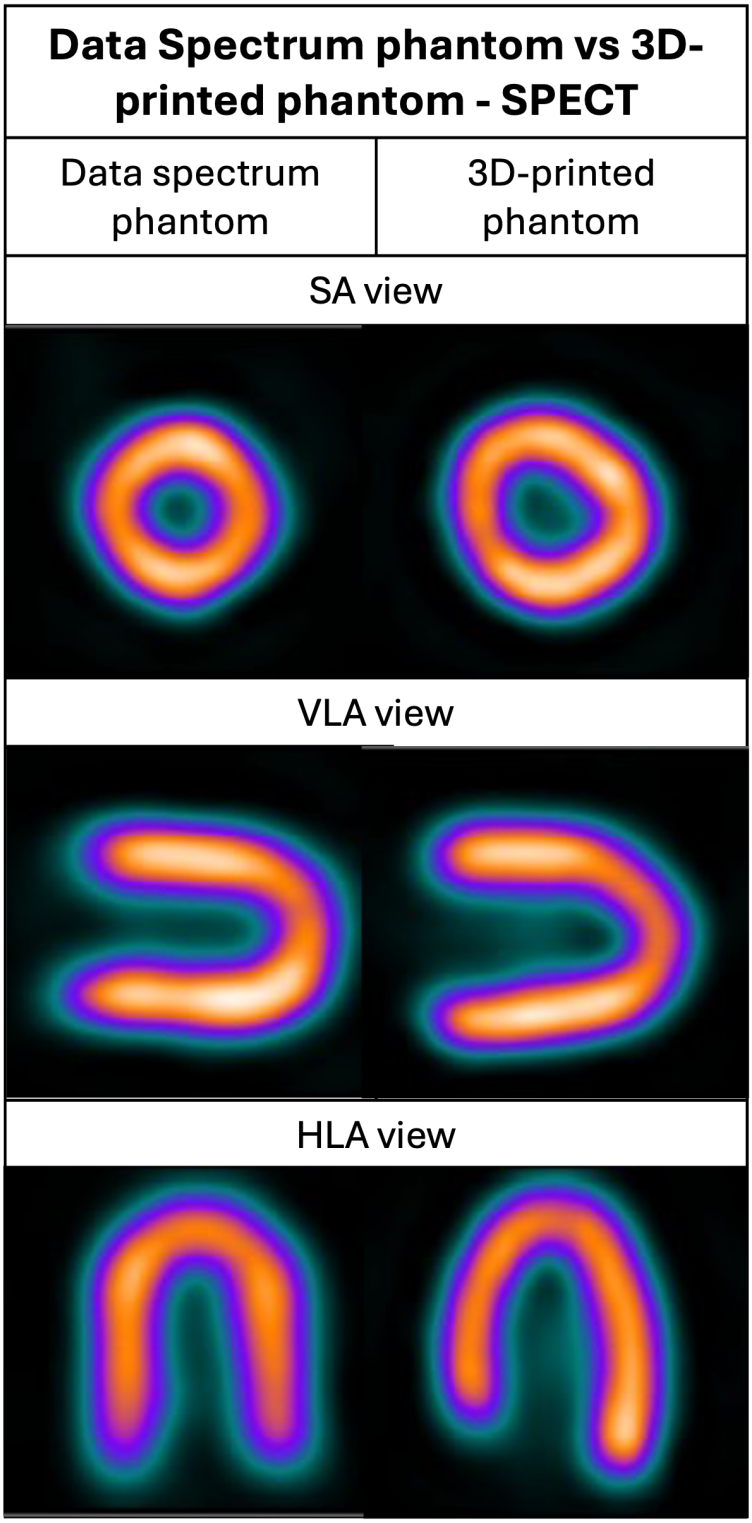


Figure 4.5: SA, VLA and HLA views obtained through imaging with SPECT

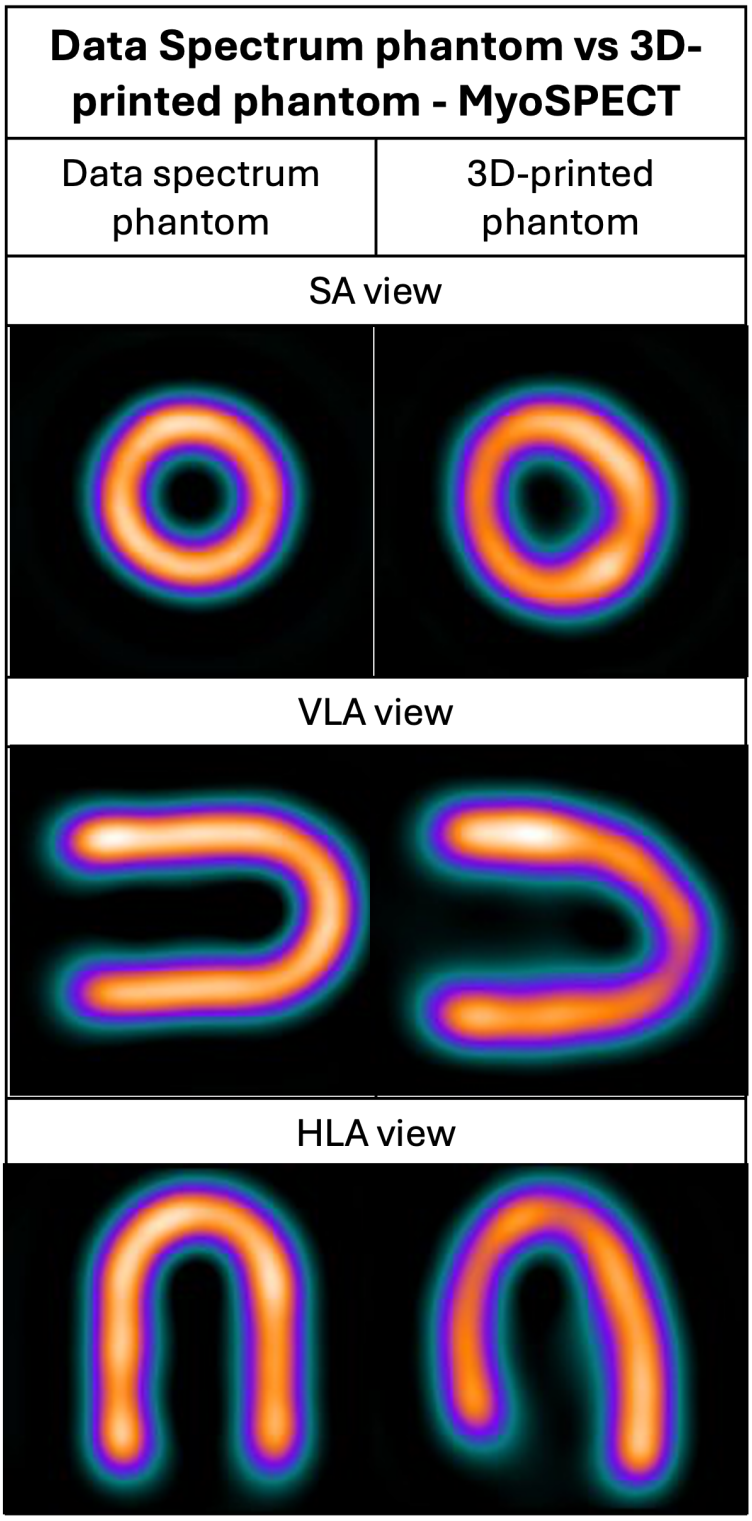


Figure 4.6: SA, VLA and HLA views obtained through imaging with MyoSPECT

### 4.5.2 | Quantitative Comparisons

To enhance the comparative analysis between the two phantoms, detailed tables were created. These tables present the values recorded for each segment, and also include the computed differences between the two phantoms for each machine.

#### 4.5.2.1 | Quantitative comparison on the values obtained from imaging with MyoSPECT

Table 4.4 presents the comparative results of the phantoms imaged with the MyoSPECT.

Table 4.4: Comparison between Data Spectrum Phantom vs 3D-Printed on MyoSPECT

| Segments | Data Spectrum Phantom | 3D-Printed Phantom | Difference |
|---|---|---|---|
| Basal Anterior | 89 | 88 | 1 |
| Basal Anteroseptal | 80 | 70 | 10 |
| Basal Inferoseptal | 83 | 67 | 16 |
| Basal Inferior | 75 | 80 | -5 |
| Basal Inferolateral | 74 | 85 | -11 |
| Basal Anterolateral | 81 | 87 | -6 |
| Mid Anterior | 89 | 93 | -4 |
| Mid Anteroseptal | 81 | 72 | 9 |
| Mid Inferoseptal | 85 | 75 | 10 |
| Mid Inferior | 85 | 82 | 3 |
| Mid Inferolateral | 81 | 84 | -3 |
| Mid Anterolateral | 80 | 86 | -6 |
| Apical Anterior | 88 | 80 | 8 |
| Apical Septal | 84 | 74 | 10 |
| Apical Inferior | 85 | 79 | 6 |
| Apical Lateral | 84 | 82 | 2 |
| Apex | 86 | 73 | 13 |

#### 4.5.2.2 | Quantitative comparison on the values obtained from imaging with SPECT

Next, the data of when the two phantoms were imaged with the SPECT were compared. The values were compiled in table 4.5.

Table 4.5: Comparison between Data Spectrum Phantom vs 3D-Printed on SPECT

| Segments | Data Spectrum Phantom | 3D-Printed Phantom | Difference |
|---|---|---|---|
| Basal Anterior | 61 | 84 | -23 |
| Basal Anteroseptal | 58 | 66 | -8 |
| Basal Inferoseptal | 67 | 68 | -1 |
| Basal Inferior | 73 | 83 | -10 |
| Basal Inferolateral | 66 | 88 | -22 |
| Basal Anterolateral | 57 | 89 | -32 |
| Mid Anterior | 86 | 87 | -1 |
| Mid Anteroseptal | 78 | 76 | 2 |
| Mid Inferoseptal | 79 | 76 | 3 |
| Mid Inferior | 87 | 90 | -3 |
| Mid Inferolateral | 75 | 89 | -14 |
| Mid Anterolateral | 74 | 87 | -13 |
| Apical Anterior | 87 | 80 | 7 |
| Apical Septal | 79 | 76 | 3 |
| Apical Inferior | 89 | 88 | 1 |
| Apical Lateral | 79 | 83 | -4 |
| Apex | 80 | 76 | 4 |

# 4.6 | Comparison between Kiss et al. (2022)'s Phantom and the 3D-printed Cardiac Phantom

## 4.6.1 | Qualitative Comparison

Another objective of the study was to compare the 3D-printed phantom against the one produced by Kiss et al. (2022). This comparison was crucial to verify that the phantom was accurately replicated through the modified specifications. Hence, confirming that the modified enhancements did not compromise the anthropomorphic structure of the phantom. These comparisons are made through figures 4.7 and 4.9.

### 4.6.1.1 | Comparison of structure through CT

To further compare the 3D-printed cardiac phantom. A CT was taken to analyse it internally and compare it with that of Kiss et al. (2022). This is represented through figure 4.7.

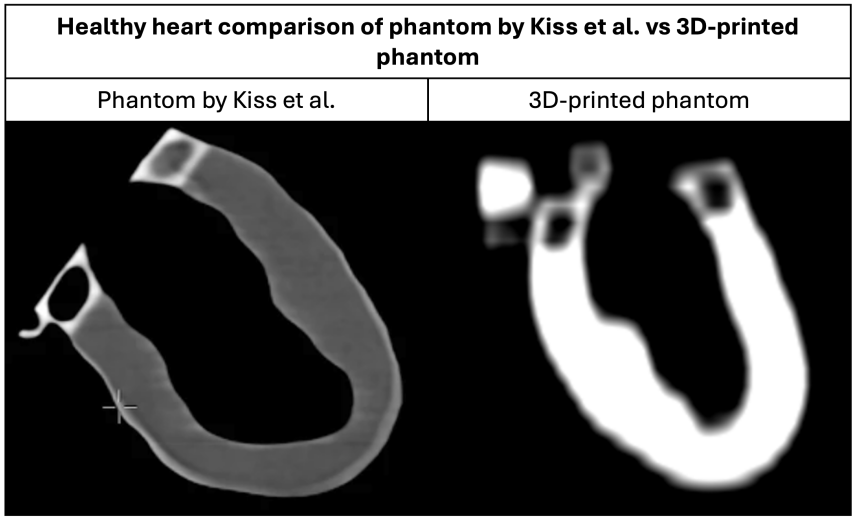


Figure 4.7: CT comparison of heart phantom produced by Kiss et al. (2022) and that 3D-printed during this study

Through this image, one can see that the phantom was replicated as expected. The only difference is its orientation. As the 3D-printed phantom had to be reoriented during imaging.

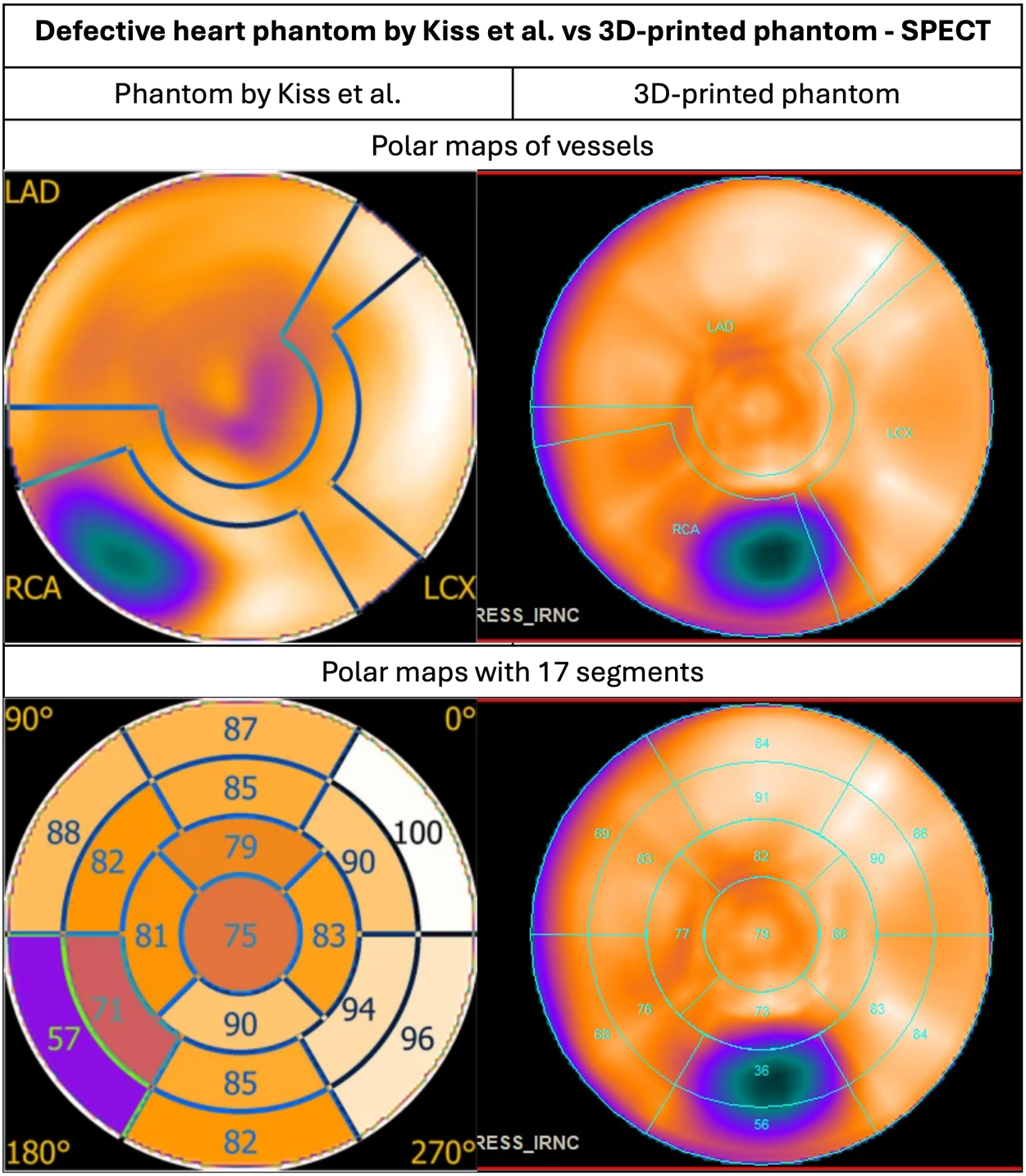


Figure 4.8: Comparison of the heart with defect

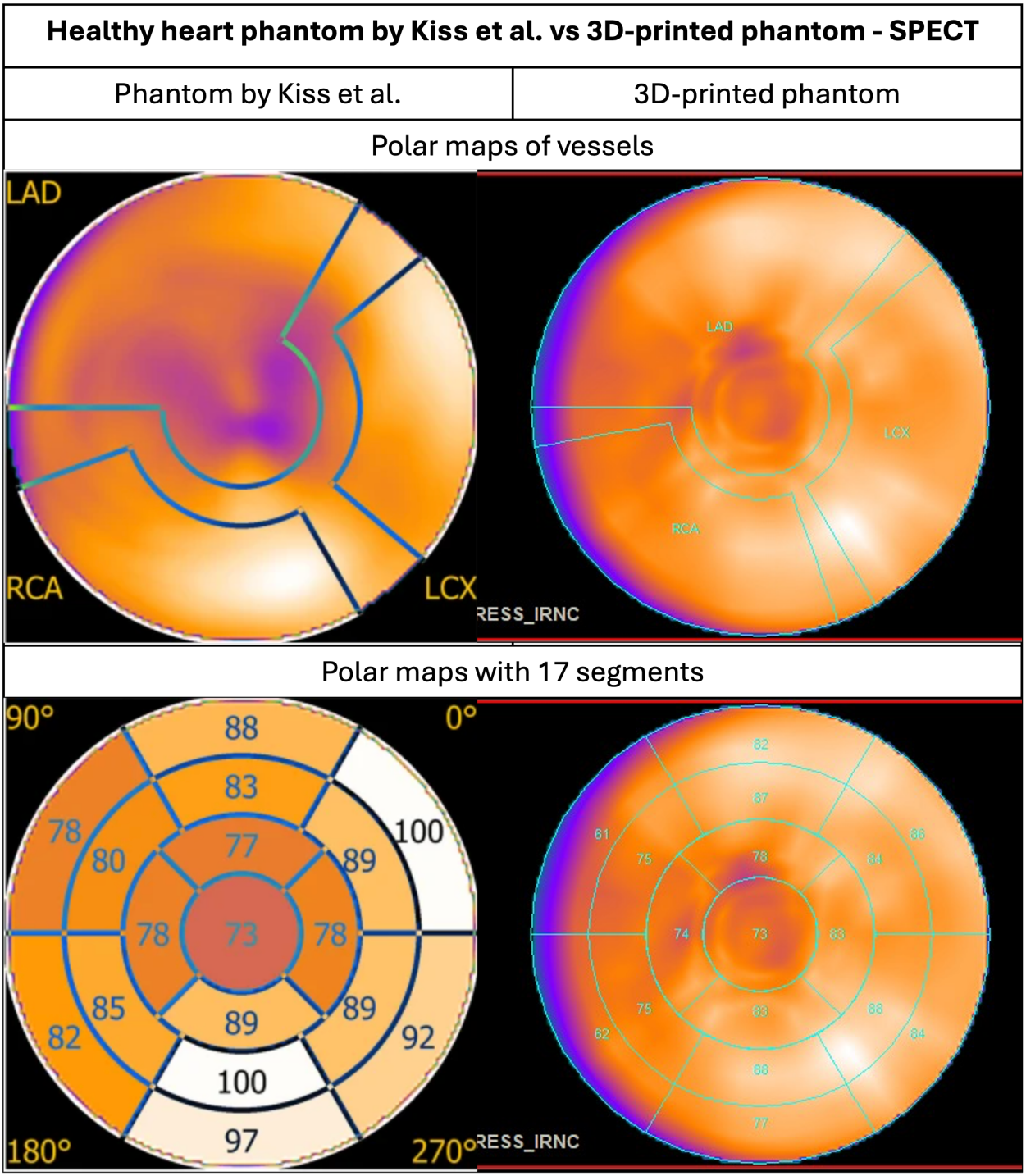


Figure 4.9: Comparison of the healthy heart

### 4.6.2 | Quantitative Comparison

Again, the values in the polar maps were tabulated for comparison. This was done for both the healthy heart phantom, in table 4.6 and the defective heart phantom, in table 4.7.

#### 4.6.2.1 | Healthy heart comparison

Table 4.6: Comparison between normal heart phantom by Kiss et al. vs 3D-printed phantom on SPECT/CT

| Segments | Data Spectrum Phantom | 3D-Printed Phantom | Difference |
|---|---|---|---|
| Basal Anterior | 88 | 82 | 6 |
| Basal Anteroseptal | 78 | 61 | 17 |
| Basal Inferoseptal | 82 | 62 | 20 |
| Basal Inferior | 97 | 77 | 20 |
| Basal Inferolateral | 92 | 84 | 8 |
| Basal Anterolateral | 100 | 86 | 14 |
| Mid Anterior | 83 | 87 | -4 |
| Mid Anteroseptal | 80 | 75 | 5 |
| Mid Inferoseptal | 85 | 75 | 10 |
| Mid Inferior | 100 | 88 | 12 |
| Mid Inferolateral | 89 | 88 | 1 |
| Mid Anterolateral | 89 | 84 | 5 |
| Apical Anterior | 77 | 78 | -1 |
| Apical Septal | 78 | 74 | 4 |
| Apical Inferior | 89 | 83 | 6 |
| Apical Lateral | 78 | 83 | -5 |
| Apex | 73 | 73 | 0 |

#### 4.6.2.2 | Defective heart comparison

Table 4.7: Comparison between phantom with defect by Kiss et al. vs 3D-printed phantom with defect on SPECT/CT

| Segments | Data Spectrum Phantom | 3D-Printed Phantom | Difference |
|---|---|---|---|
| Basal Anterior | 87 | 84 | 3 |
| Basal Anteroseptal | 88 | 69 | 19 |
| Basal Inferoseptal | 57 | 68 | -11 |
| Basal Inferior | 82 | 56 | 26 |
| Basal Inferolateral | 96 | 84 | 12 |
| Basal Anterolateral | 100 | 86 | 14 |
| Mid Anterior | 85 | 91 | -6 |
| Mid Anteroseptal | 82 | 83 | -1 |
| Mid Inferoseptal | 71 | 76 | -5 |
| Mid Inferior | 85 | 36 | 49 |
| Mid Inferolateral | 94 | 83 | 11 |
| Mid Anterolateral | 90 | 90 | 0 |
| Apical Anterior | 79 | 82 | -3 |
| Apical Septal | 81 | 77 | 4 |
| Apical Inferior | 90 | 73 | 17 |
| Apical Lateral | 83 | 86 | -3 |
| Apex | 75 | 79 | -4 |

## 4.7 | Comparison between SPECT and MyoSPECT Heart with defect at different levels of activity

The next objective aimed at comparing the image quality of the SPECT vs the cardiac-dedicated MyoSPECT. For this comparison, the defective phantom was imaged when it contained 5 different levels of activity. First 6 MBq and then, by giving it time to decay, at 5 MBq, 4 MBq, 3 MBq and 2 MBq. The different levels of activity were necessary to evaluate if the MyoSPECT obtains clinically significant results even at the low levels of uptake in the heart. The polar maps and different views of the heart are compared in figures 4.10 to 4.14.

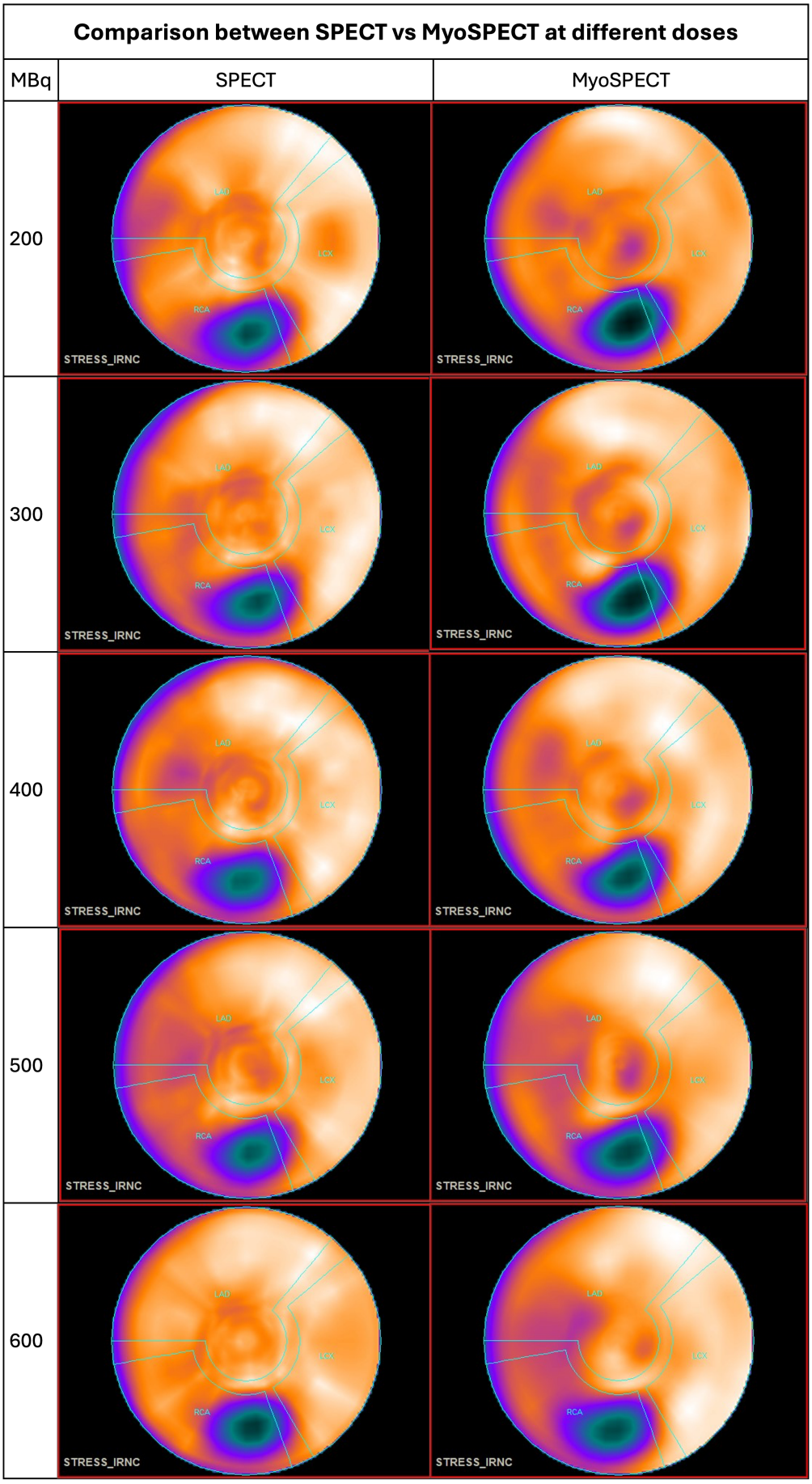


Figure 4.10: Comparison of SPECT and MyoSPECT through polar maps of the vessels

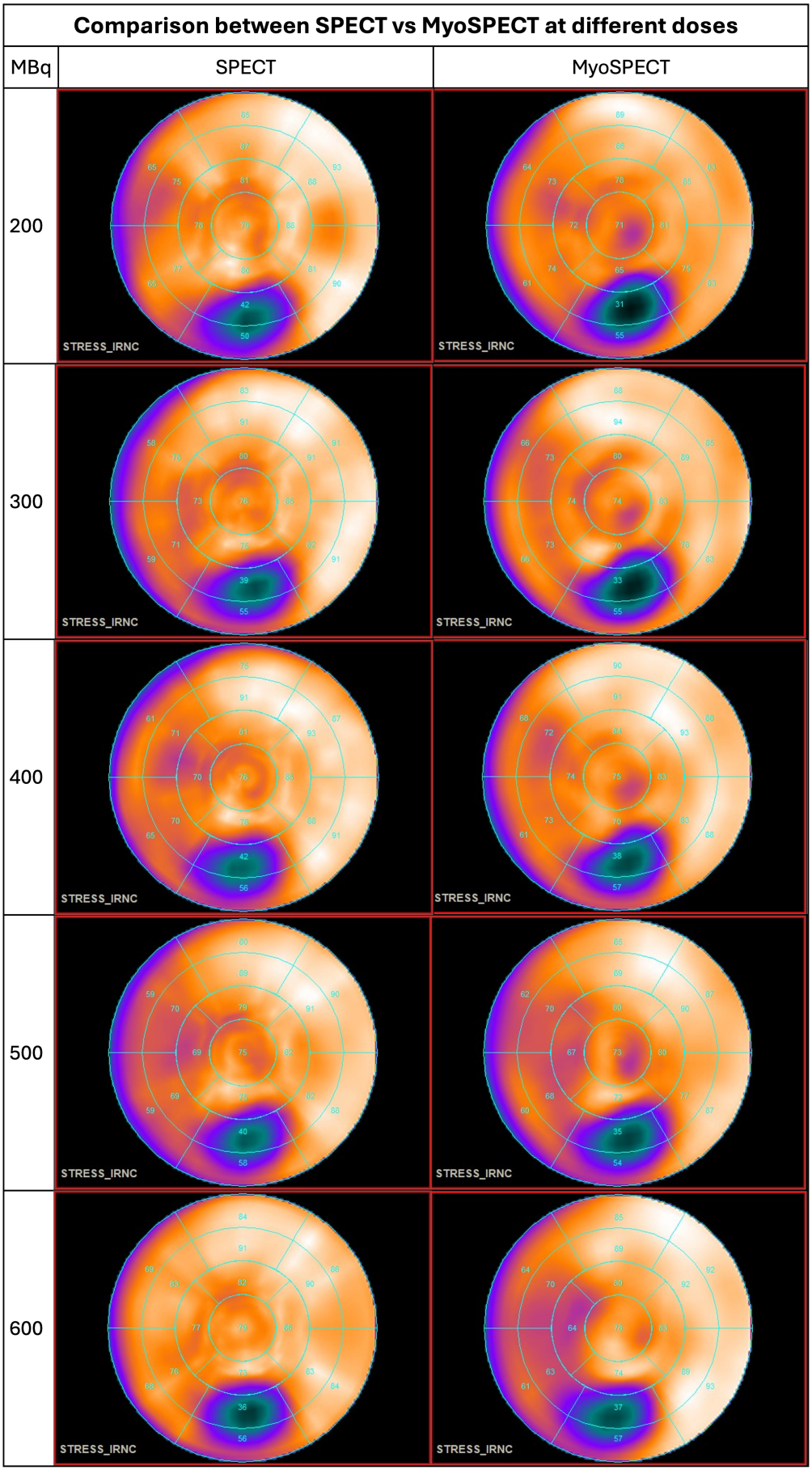


Figure 4.11: Comparison of SPECT and MyoSPECT through polar maps of the segments

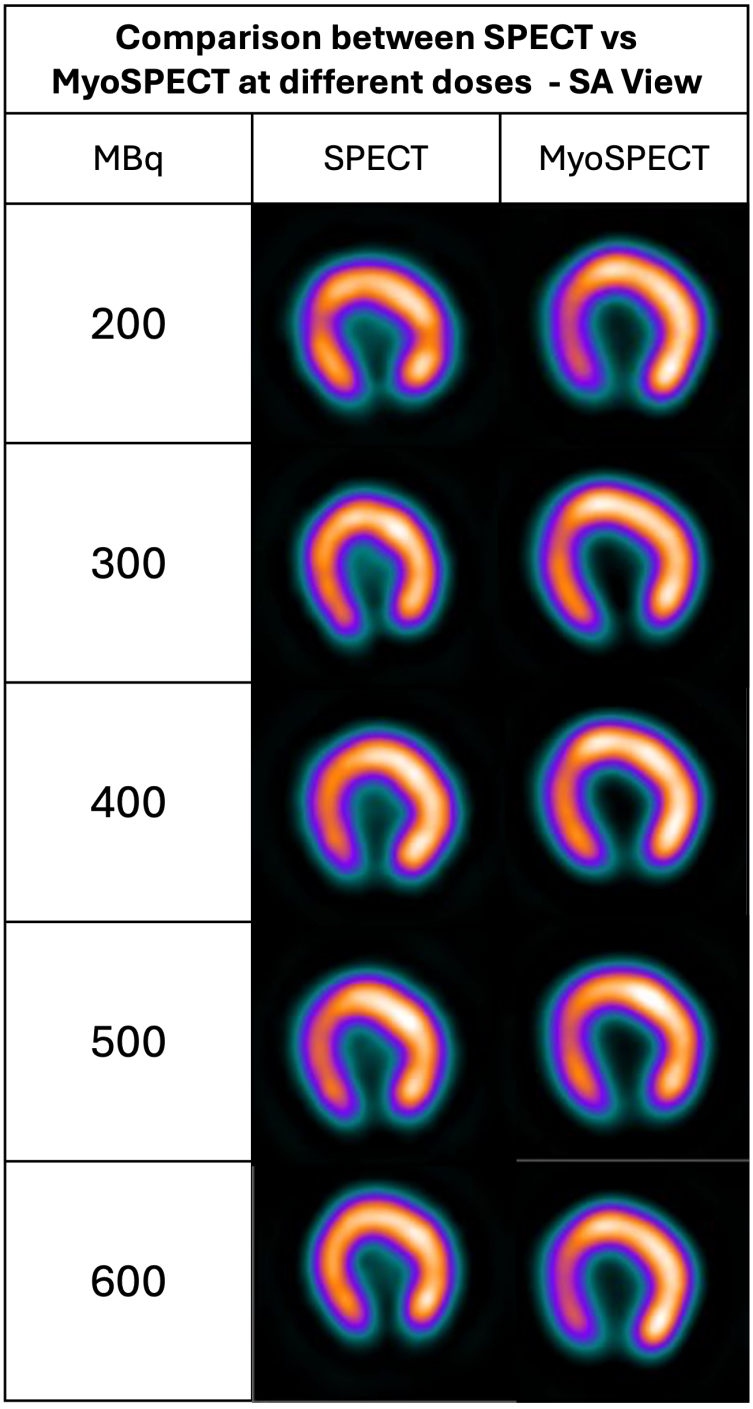


Figure 4.12: Comparison of SPECT and MyoSPECT through the SA view

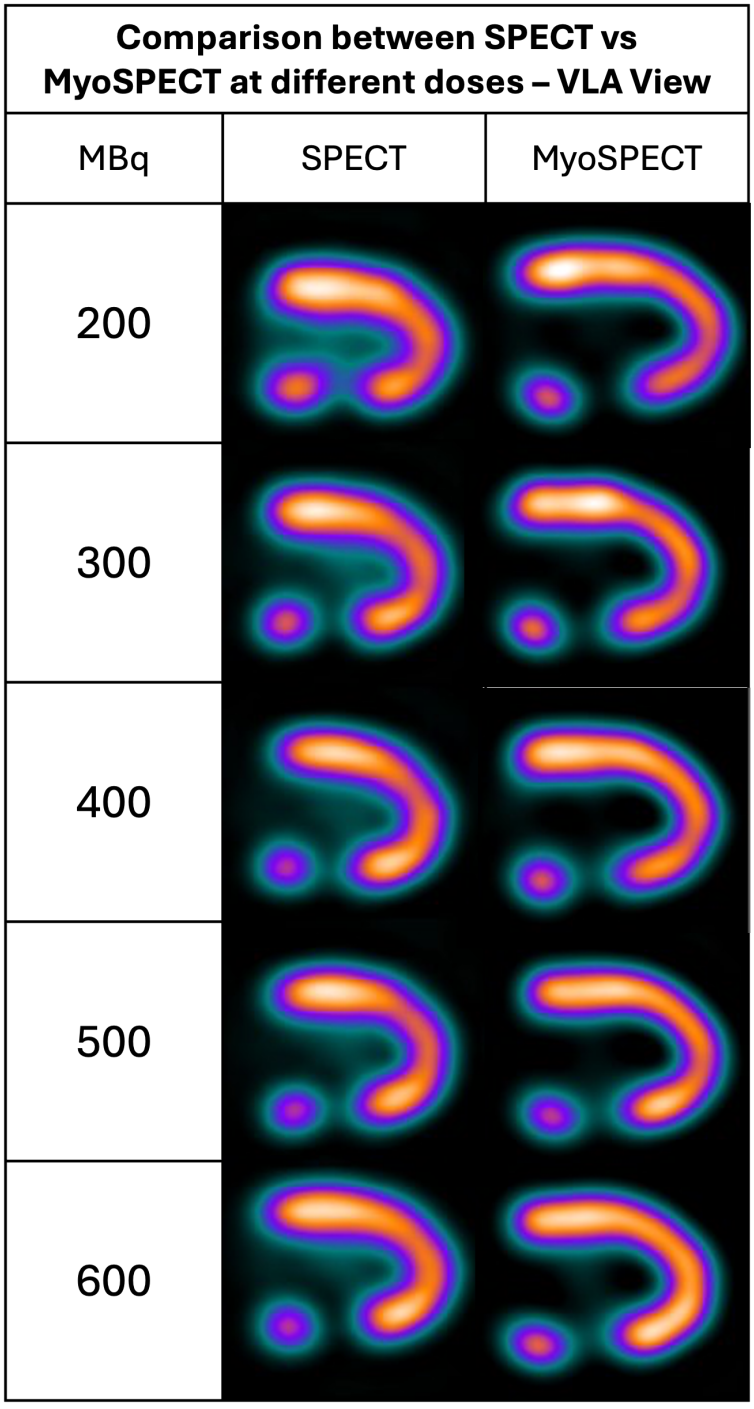


Figure 4.13: Comparison of SPECT and MyoSPECT through the VLA view

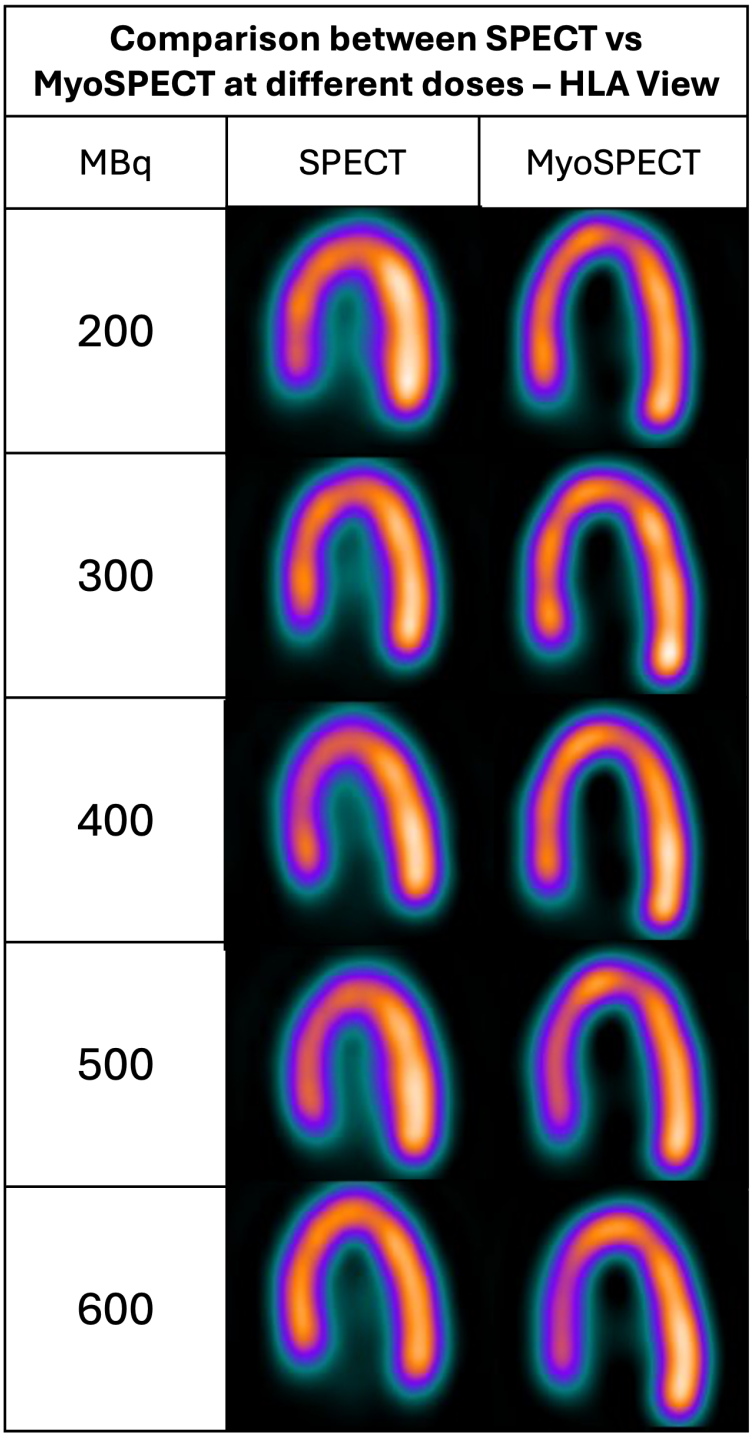


Figure 4.14: Comparison of SPECT and MyoSPECT through the HLA view

### 4.7.1 | Quantitative Comparison

Two tables were compiled. The first table was compiled to compare the ultralow dose protocol with the high dose protocol. The other table was compiled to compare the other levels of activity within the phantom.

#### 4.7.1.1 | Ultra-Low Dose vs High Dose Protocol

Table 4.8: Comparison between SPECT and MyoSPECT for the ultra-low and high dose protocol - 3D-printed heart with defect

| **Segments** | **200 MBq** | | **600 MBq** | |
|---|---|---|---|---|
| | **SPECT** | **MyoSPECT** | **SPECT** | **MyoSPECT** |
| Basal Anterior | 85 | 89 | 84 | 85 |
| Basal Anteroseptal | 65 | 64 | 69 | 64 |
| Basal Inferoseptal | 65 | 61 | 68 | 61 |
| Basal Inferior | 50 | 55 | 56 | 57 |
| Basal Inferolateral | 90 | 83 | 84 | 93 |
| Basal Anterolateral | 93 | 83 | 86 | 92 |
| Mid Anterior | 87 | 86 | 91 | 89 |
| Mid Anteroseptal | 75 | 73 | 83 | 70 |
| Mid Inferoseptal | 77 | 74 | 76 | 63 |
| Mid Inferior | 42 | 31 | 36 | 37 |
| Mid Inferolateral | 81 | 75 | 83 | 89 |
| Mid Anterolateral | 88 | 85 | 90 | 92 |
| Apical Anterior | 81 | 78 | 82 | 80 |
| Apical Septal | 78 | 72 | 64 | 74 |
| Apical Inferior | 80 | 65 | 86 | 83 |
| Apical Lateral | 88 | 81 | 79 | 78 |
| Apex | 79 | 71 | 78 | 78 |

#### 4.7.1.2 | Comparison between 300, 400 and 500 MBq dose

Table 4.9: Comparison between SPECT and MyoSPECT at 300 MBq, 400 MBq, and 500 MBq doses - 3D-printed heart with defect

| **Segments** | **300 MBq** | | **400 MBq** | | **500 MBq** | |
|---|---|---|---|---|---|---|
| | **SPECT** | **MyoSPECT** | **SPECT** | **MyoSPECT** | **SPECT** | **MyoSPECT** |
| Basal Anterior | 83 | 88 | 75 | 90 | 80 | 85 |
| Basal Anteroseptal | 58 | 66 | 61 | 68 | 59 | 62 |
| Basal Inferoseptal | 59 | 66 | 65 | 61 | 59 | 60 |
| Basal Inferior | 55 | 55 | 56 | 57 | 58 | 54 |
| Basal Inferolateral | 91 | 83 | 91 | 88 | 88 | 87 |
| Basal Anterolateral | 91 | 85 | 87 | 88 | 90 | 87 |
| Mid Anterior | 91 | 94 | 91 | 91 | 89 | 89 |
| Mid Anteroseptal | 78 | 73 | 71 | 72 | 70 | 70 |
| Mid Inferoseptal | 71 | 73 | 70 | 73 | 69 | 68 |
| Mid Inferior | 39 | 33 | 42 | 38 | 40 | 35 |
| Mid Inferolateral | 82 | 78 | 88 | 83 | 82 | 77 |
| Mid Anterolateral | 91 | 89 | 93 | 90 | 90 | 90 |
| Apical Anterior | 80 | 80 | 81 | 84 | 79 | 80 |
| Apical Septal | 73 | 74 | 70 | 74 | 67 | 77 |
| Apical Inferior | 75 | 70 | 78 | 72 | 73 | 74 |
| Apical Lateral | 85 | 83 | 85 | 83 | 82 | 80 |
| Apex | 76 | 74 | 75 | 73 | 75 | 79 |

# 4.8 | Comparison between SPECT and MyoSPECT Healthy heart with activities for ultra-low dose, normal dose and high dose protocol

## 4.8.1 | Qualitative Comparison

To further investigate the objective of comparing the SPECT with MyoSPECT the healthy heart was also imaged with both machines. This time however through the doses one would deliver under three different types of protocols. Thus, the Ultra low dose, the normal dose and the high dose. Hence with 2, 4 and 6 MBq respectively. Again, the polar maps and different views of the heart are compared in figures 4.15 to 4.19.

## 4.8.2 | Quantitative Comparison

Table 4.10: Comparison between SPECT and MyoSPECT at different doses

| Segments | 200 MBq | | 400 MBq | | 600 MBq | |
|---|---|---|---|---|---|---|
| | SPECT | MyoSPECT | SPECT | MyoSPECT | SPECT | MyoSPECT |
| Basal Anterior | 85 | 85 | 84 | 88 | 82 | 91 |
| Basal Anteroseptal | 70 | 70 | 66 | 70 | 61 | 71 |
| Basal Inferoseptal | 71 | 71 | 68 | 67 | 62 | 70 |
| Basal Inferior | 80 | 80 | 83 | 80 | 77 | 82 |
| Basal Inferolateral | 89 | 89 | 88 | 85 | 84 | 88 |
| Basal Anterolateral | 81 | 81 | 89 | 87 | 86 | 90 |
| Mid Anterior | 86 | 86 | 87 | 93 | 87 | 94 |
| Mid Anteroseptal | 80 | 80 | 76 | 72 | 75 | 79 |
| Mid Inferoseptal | 73 | 73 | 76 | 75 | 75 | 79 |
| Mid Inferior | 84 | 84 | 90 | 82 | 88 | 86 |
| Mid Inferolateral | 89 | 89 | 89 | 84 | 88 | 89 |
| Mid Anterolateral | 86 | 86 | 87 | 86 | 84 | 90 |
| Apical Anterior | 78 | 77 | 80 | 80 | 78 | 81 |
| Apical Septal | 77 | 76 | 76 | 74 | 74 | 76 |
| Apical Inferior | 83 | 82 | 88 | 79 | 83 | 84 |
| Apical Lateral | 86 | 85 | 83 | 82 | 83 | 87 |
| Apex | 76 | 76 | 76 | 73 | 73 | 77 |

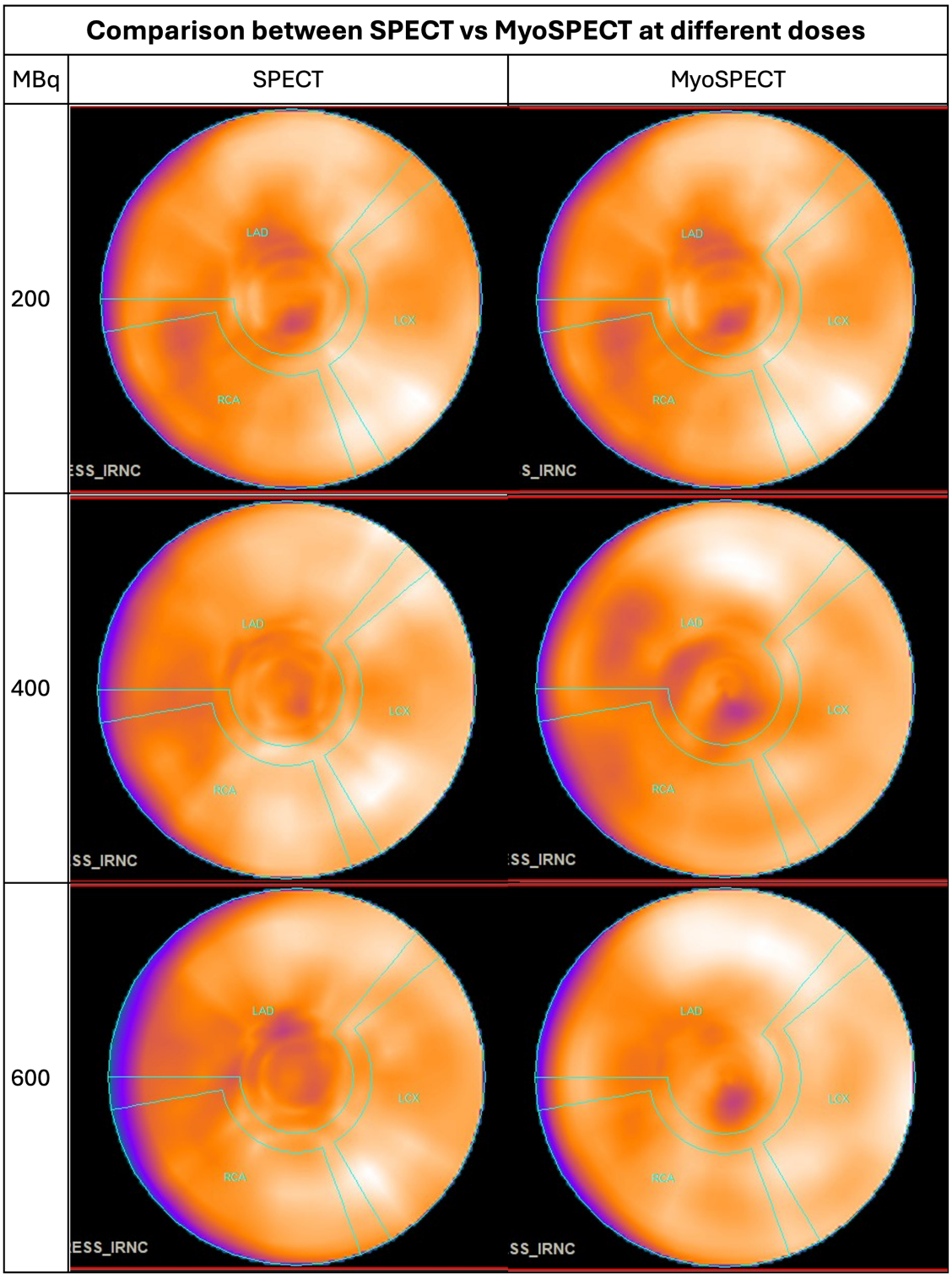


Figure 4.15: Comparison of SPECT and MyoSPECT through polar maps of the vessels

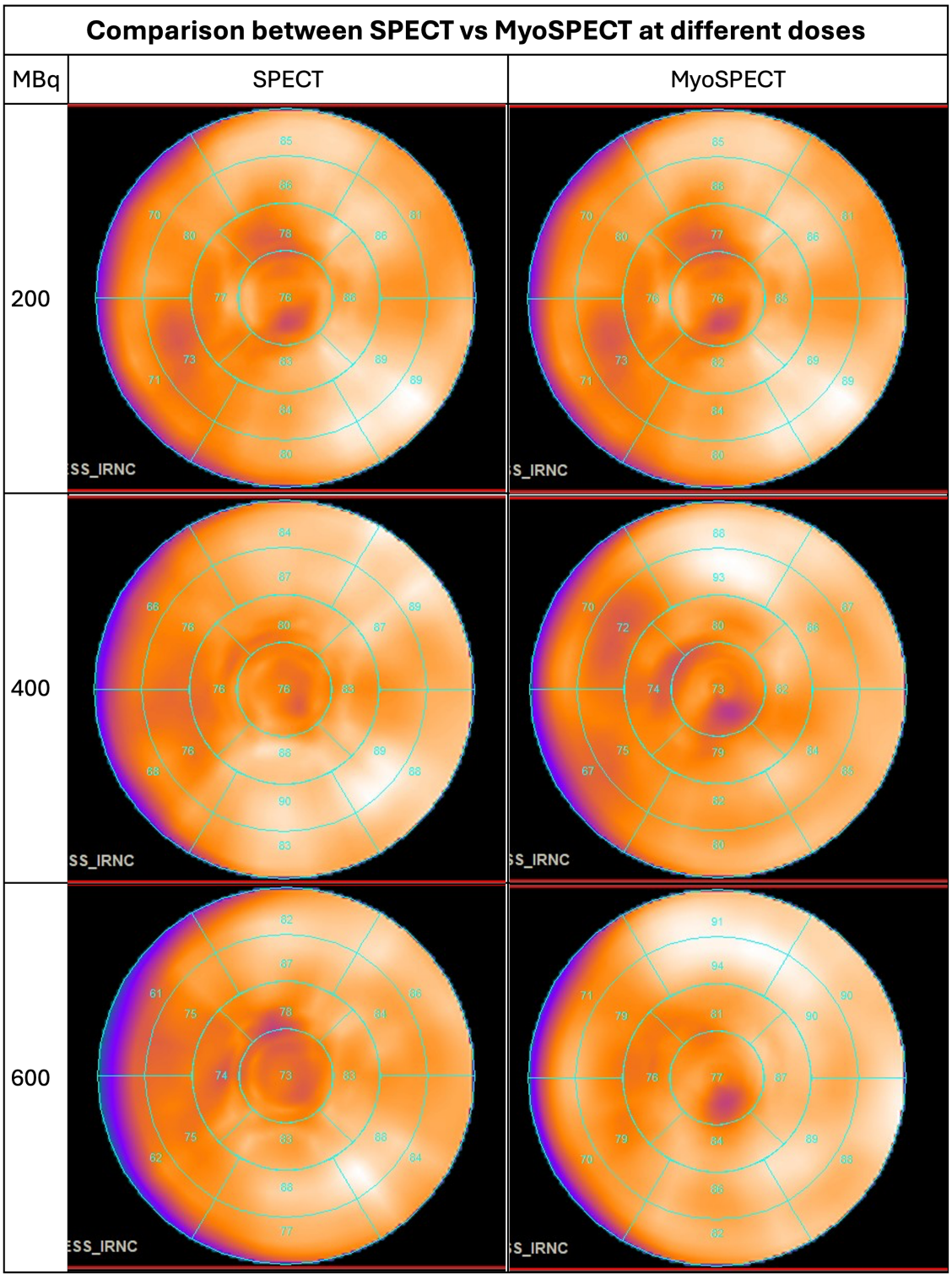


Figure 4.16: Comparison of SPECT and MyoSPECT through polar maps of the segments

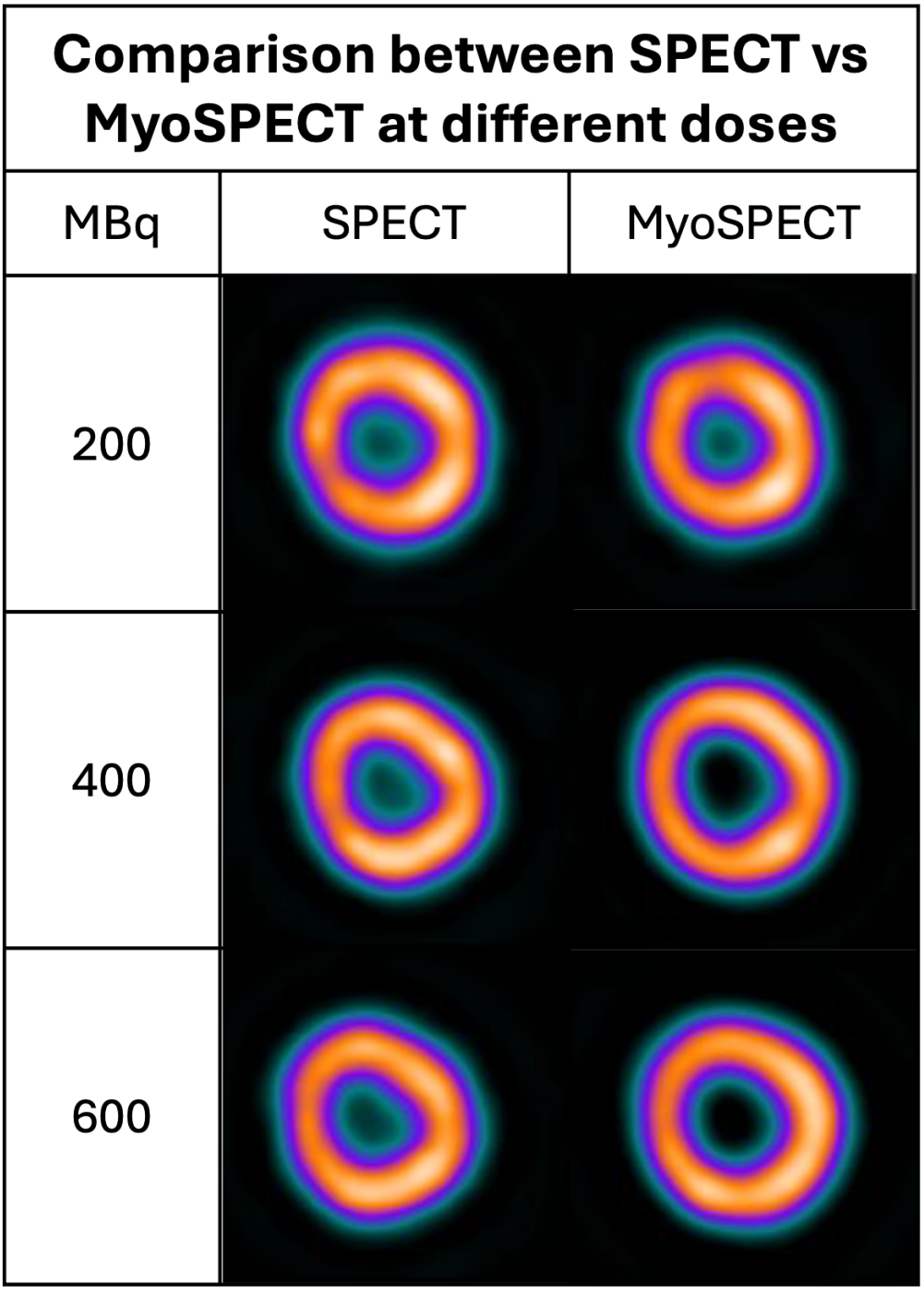


Figure 4.17: Comparison of SPECT and MyoSPECT through the SA view

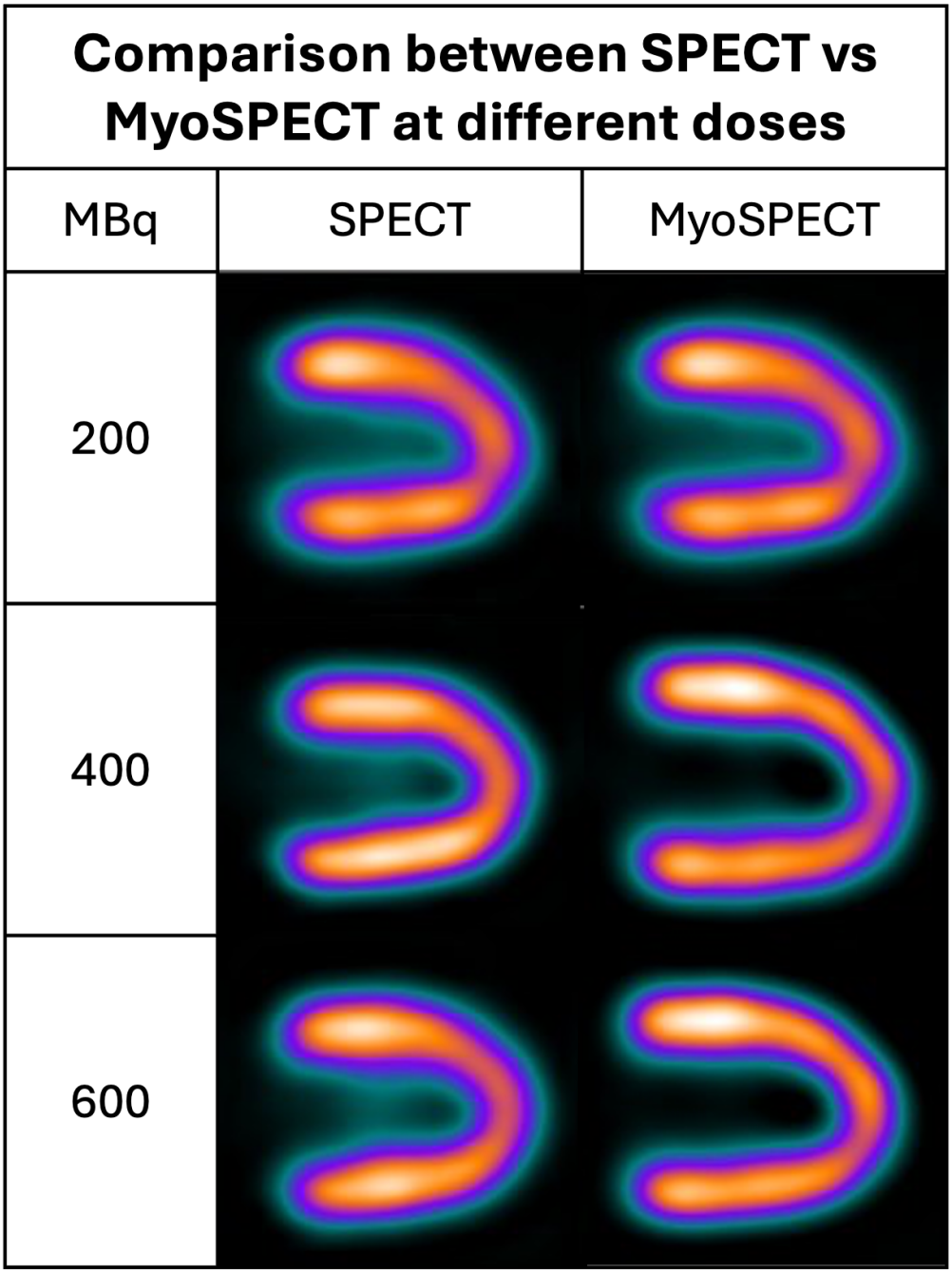


Figure 4.18: Comparison of SPECT and MyoSPECT through the VLA view

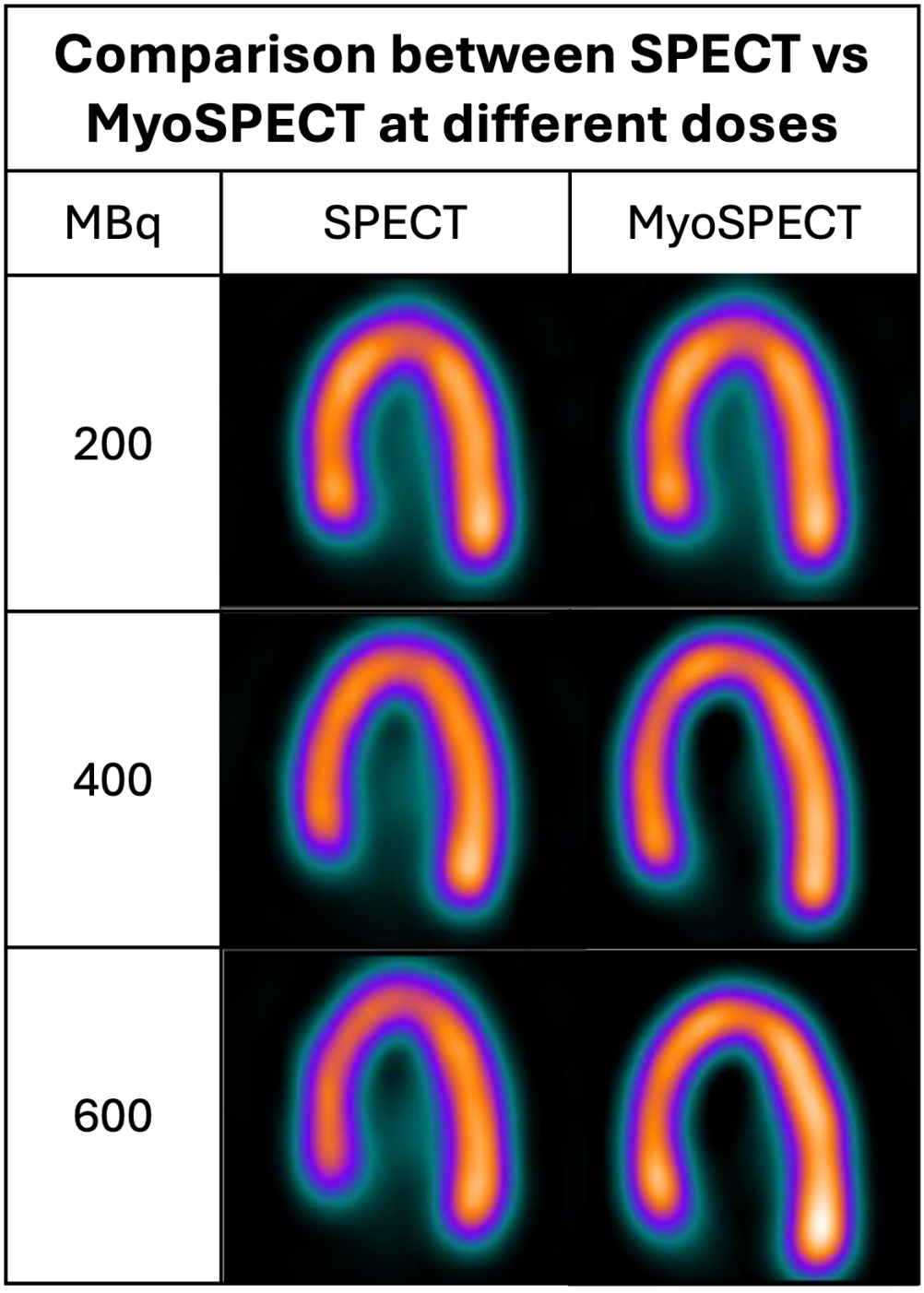


Figure 4.19: Comparison of SPECT and MyoSPECT through the HLA view

# 4.9 | Data analysis and results

## 4.9.1 | Statistical analysis of results

To properly compare the imaging quality and the differences between the SPECT and MyoSPECT a comprehensive statistical analysis was required. The mean, standard deviation and paired t-test were conducted for the segment values at the different levels of activity present in the phantoms.

### 4.9.1.1 | Statistical analysis of the results of the heart with the defect at different levels of activity

The mean and standard deviation of each segment's uptake values across the different doses for both the SPECT and the MyoSPECT were both computed. Their values can be found in tables 4.11 and 4.13.

Table 4.11: Mean and standard deviation of uptake values in the polar map segments of the phantoms with defect

| Segments | SPECT | | MyoSPECT | |
|---|---|---|---|---|
| | Mean | Std Dev | Mean | Std Dev |
| Basal Anterior | 75 | 10 | 77 | 9 |
| Basal Anteroseptal | 65 | 4 | 6 | 4 |
| Basal Inferoseptal | 63 | 6 | 64 | 6 |
| Basal Inferior | 57 | 7 | 57 | 7 |
| Basal Inferolateral | 89 | 2 | 89 | 2 |
| Basal Anterolateral | 85 | 5 | 86 | 4 |
| Mid Anterior | 86 | 3 | 86 | 3 |
| Mid Anteroseptal | 73 | 3 | 74 | 3 |
| Mid Inferoseptal | 72 | 4 | 73 | 3 |
| Mid Inferior | 52 | 4 | 52 | 4 |
| Mid Inferolateral | 79 | 4 | 80 | 3 |
| Mid Anterolateral | 86 | 4 | 86 | 4 |
| Apical Anterior | 81 | 2 | 80 | 2 |
| Apical Septal | 76 | 3 | 76 | 3 |
| Apical Inferior | 75 | 4 | 74 | 4 |
| Apical Lateral | 82 | 4 | 81 | 4 |
| Apex | 75 | 4 | 75 | 4 |

Then the paired t-test was performed to assess if there were statistically significant differences between the SPECT and MyoSPECT values. To conduct the paired t-test the difference between the paired measurements (SPECT and MyoSPECT values) for each segment was computed. Then, the mean of these differences was calculated. The standard deviation of the differences was also found and finally, the paired t-test equation was used.

$$t = \frac{\text{Mean Difference}}{\frac{\text{Standard Deviation of Differences}}{\sqrt{n}}} \tag{4.1}$$

where $n$ is the number of paired measurements.

Table 4.12: Paired t-test results of polar map values of phantom with defect

| **Segments** | **p-value** |
|---|---|
| Basal Anterior | 0.08 |
| Basal Anteroseptal | 0.20 |
| Basal Inferoseptal | 0.10 |
| Basal Inferior | 0.15 |
| Basal Inferolateral | 0.07 |
| Basal Anterolateral | 0.05 |
| Mid Anterior | 0.22 |
| Mid Anteroseptal | 0.30 |
| Mid Inferoseptal | 0.18 |
| Mid Inferior | 0.14 |
| Mid Inferolateral | 0.13 |
| Mid Anterolateral | 0.25 |
| Apical Anterior | 0.12 |
| Apical Septal | 0.11 |
| Apical Inferior | 0.17 |
| Apical Lateral | 0.09 |
| Apex | 1.00 |

For a result to be considered statistically significant, the p-value must be less than 0.05.

#### 4.9.1.2 | Statistical analysis of the results of the healthy heart at the three different levels of activity

The same process was conducted for these results too. Allowing for a better comparison of the performance of the two machines. Thus, the mean and standard deviation of the results are found in table 4.13.

Table 4.13: Mean and standard deviation of uptake values in the polar map segments of the healthy heart phantoms

| **Segments** | **SPECT** | | **MyoSPECT** | |
|---|---|---|---|---|
| | **Mean** | **Std Dev** | **Mean** | **Std Dev** |
| Basal Anterior | 84 | 2 | 87 | 5 |
| Basal Anteroseptal | 66 | 4 | 69 | 5 |
| Basal Inferoseptal | 68 | 5 | 66 | 4 |
| Basal Inferior | 80 | 2 | 80 | 1 |
| Basal Inferolateral | 86 | 3 | 86 | 2 |
| Basal Anterolateral | 85 | 2 | 86 | 2 |
| Mid Anterior | 87 | 2 | 91 | 4 |
| Mid Anteroseptal | 76 | 3 | 74 | 3 |
| Mid Inferoseptal | 75 | 3 | 74 | 3 |
| Mid Inferior | 76 | 2 | 80 | 2 |
| Mid Inferolateral | 87 | 2 | 87 | 2 |
| Mid Anterolateral | 86 | 1 | 88 | 2 |
| Apical Anterior | 79 | 1 | 78 | 1 |
| Apical Septal | 75 | 1 | 75 | 2 |
| Apical Inferior | 83 | 2 | 82 | 2 |
| Apical Lateral | 83 | 3 | 84 | 1 |
| Apex | 74 | 3 | 75 | 2 |

Table 4.14: Paired t-test Results - for healthy heart phantom

| **Segments** | **p-value** |
|---|---|
| Basal Anterior | 0.11 |
| Basal Anteroseptal | 0.05 |
| Basal Inferoseptal | 0.15 |
| Basal Inferior | 1.00 |
| Basal Inferolateral | 0.75 |
| Basal Anterolateral | 0.70 |
| Mid Anterior | 0.06 |
| Mid Anteroseptal | 0.10 |
| Mid Inferoseptal | 0.15 |
| Mid Inferior | 0.02 |
| Mid Inferolateral | 0.85 |
| Mid Anterolateral | 0.12 |
| Apical Anterior | 0.50 |
| Apical Septal | 1.00 |
| Apical Inferior | 0.30 |
| Apical Lateral | 0.30 |
| Apex | 0.70 |

## 4.10 | Conclusion

This chapter has presented the results obtained from the experiments and analyses conducted, effectively mapping them to the objectives outlined in this study. These results provide a comprehensive overview of the performance and effectiveness of the 3D-printed phantoms. The subsequent chapter will offer a thorough discussion of these findings, interpreting the results in the context of the study's objectives and exploring their implications for future research and clinical practice.

# 5

# Discussion

## 5.1 | Introduction

This discussion section focuses on evaluating the findings of the study in relation to the objectives set forth, highlighting the implications for medical physics and nuclear medicine practices. The study explored various aspects of FDM based 3D printing technology for fabricating a reliable, waterproof cardiac phantom, examining both material properties and imaging performance.

Methodological challenges, such as ensuring watertightness and optimizing imaging protocols, were also addressed. Additionally, this section compares the effectiveness of different imaging systems, the SPECT and MyoSPECT, in capturing accurate myocardial perfusion patterns. Through this comprehensive evaluation, the discussion emphasizes the practical applications of these findings, the limitations encountered, and the potential for future research to expand on these innovations. The degree to which the study's objectives have been met is critically analyzed, providing a detailed understanding of the results in the context of existing literature and clinical practice.

## 5.2 | Discussion

### 5.2.1 | Materials, parameters and configurations to 3D-print the cardiac phantom

To effectively address the first and second objectives of the study, the research utilised insights from both Romero et al. (2021) and Castaneda (2017). The extensive literature review and pilot study were crucial in identifying the optimal 3D-printing parameters for creating a waterproof nuclear medicine cardiac phantom. The initial methodology for testing these parameters was guided by the work of Romero et al. (2021). A significant breakthrough occurred when techniques from a different field, specifically the 3D printing of microfluidic structures as developed by Castaneda (2017) were applied. This led to the production of watertight prints without the need for additional post-processing.

The use of Ultimaker's transparent PETG filament, combined with specific adjustments—such as increasing the extrusion multiplier to 103%, reducing the layer height to 0.05 mm, increasing the number of perimeters to 8, slowing the print speed to 30 mm/s, and randomly orienting the seam position—resulted in phantoms that were not only watertight but also fully transparent. The transparency of the phantom is essential, as it facilitates the detection of air gaps during the filling process, ensuring a consistent internal fill.

This study stands out from others in the field, as it achieved waterproof FDM printed prints without the need for post-processing steps like applying acrylic spray. Additionally, a novel post-processing technique using Dichtol AM Hydro was evaluated. Unlike traditional methods, this chemical solution penetrates the microscopic gaps between layers, effectively sealing the print from the inside out. Submerging the phantom in Dichtol AM Hydro for at least 10 minutes provided a more robust waterproofing solution and prevented leakage.

Another advantage of this post-processing technique over the other "traditional" technique is that

it prevents any radioactive atoms from becoming trapped in the microscopic gaps between the layers. Which could otherwise remain radioactive even after the phantom is emptied. As a result, the phantom can be safely reused without waiting for prolonged decay periods.

As Kočí (2024) highlighted through their experience in trying to make prints waterproof, the main challenge in waterproofing the phantom arose from its openings. Screws were initially used to seal the openings. This approach worked well when the phantom was in the hot lab and the MyoSPECT system room; both of which had similar temperatures. However, when the phantom was moved to the SPECT/CT system room, where the temperature was significantly lower, the screws contracted. In turn, this created small gaps that allowed radioactive fluid to leak. The SPECT/CT room is kept colder due to the presence of heavier machinery and the need to reduce humidity, which is necessary to protect the hygroscopic NaI(TI) crystals.

To prevent leakage due to the fluid naturally flowing downward, the phantom had to be repositioned. This meant placing the phantom in an unnatural position that did not accurately represent the orientation of the left ventricle in a patient. To address this issue, the heart's orientation was adjusted during image processing on the Xeleris system. This, however, inadvertently introduced this limitation to the study.

Using rubber or silicone plugs or stoppers would have been a more effective solution for sealing the openings, as they would adapt better to temperature changes while maintaining the functionality of the hole. Additionally, combining these plugs with a snap-fit cap would ensure complete water retention and ease of use.

Ultimately, this comprehensive approach successfully achieved the study's first and second objective, which was to identify the best 3D-printing parameters and post-processing required for creating a reliable and watertight cardiac phantom.

### 5.2.2 | Collaborating with another 3D-printing project

The third objective of this study was to collaborate with another member of the 3D-printing research group, whose project focused on fabricating an obese thoracic phantom. As shown in Figure 4.2, the cardiac phantom was effectively integrated within the larger 3D-printed thoracic phantom. It was positioned and oriented to accurately replicate the location of the left ventricle in a patient, effectively mimicking the anatomical placement of the heart.

This collaboration highlights the effectiveness and versatility of 3D printing within the medical physics profession. The technology can be used to create a wide range of phantoms, allowing medical physicists to enhance patient care in innovative ways. By enabling the testing and refinement of specific treatment and diagnostic strategies before patient application, 3D printing makes the role of medical physicists even more critical in delivering high-quality healthcare services.

## 5.3 | Evaluating the performance of the 3D-printed phantom

To further assess the effectiveness of the 3D-printed phantom its performance was compared to the Data Spectrum Phantom. Both qualitative and quantitative comparisons were made between the two phantoms.

The qualitative evaluation, illustrated in Figures 4.3 to 4.6, reveals notable differences. When examining figure 4.3, which displays the polar maps obtained from both phantoms using the SPECT, it is immediately apparent that the Data Spectrum Phantom shows significantly less uptake in the basal segments of the heart. This pattern is clinically unrealistic, underscoring the importance of using an anthropomorphic phantom for such studies.

The same comparison was conducted with images obtained from the MyoSPECT. Here, it becomes evident that the MyoSPECT, with its advanced pinhole collimator system and OSEM reconstruction technique, captures more accurate uptake patterns compared to the SPECT. Unlike the SPECT, the MyoSPECT does not show a decline in uptake in the basal segments of the phan-

tom. This effectiveness in accurately reconstructing the phantom's structure through its uptake is further demonstrated when comparing figure 4.5 with figure 4.6. The MyoSPECT captures the perfectly cylindrical structure of the Data Spectrum Phantom much better than the SPECT.

A more detailed analysis of the differences and performance of the 3D-printed phantom was conducted through a quantitative comparison, where the polar map values of the 17 segments captured by both imaging modalities were compared. This comparison highlights significant differences, particularly in the LAD and RCA regions. The 3D-printed phantom, designed to be more anthropomorphic, shows lower perfusion values in segments like the basal anteroseptal and mid-anteroseptal (70% and 72%, respectively) compared to the Data Spectrum Phantom (80% and 81%). Similarly, in the RCA region, segments like the basal inferoseptal and mid-inferoseptal exhibit notable differences, with the 3D-printed phantom displaying values of 67% and 75%, in contrast to 83% and 85% in the Data Spectrum Phantom.

One thing to comment on however is that ideally, this comparison should have been conducted with similar levels of activity, targeting 4 MBq in both phantoms. This activity level mimics a 1% uptake, as recommended by Boschi et al. (2022), during a typical procedure with 400 MBq of activity. However, extracting such a small amount of activity from the generator proved challenging. As a result, the 3D-printed phantom contained 3.06 MBq and 3.01 MBq of activity when imaged with the MyoSPECT and SPECT, respectively. In contrast, the Data Spectrum Phantom had 3.73 MBq and 3.46 MBq of activity when imaged with the MyoSPECT and SPECT, respectively. This discrepancy introduced a limitation, creating a variation in activity levels between the two phantoms. Ultimately affecting the comparison of uptake patterns.

With that aside, however, the differences are likely due to the more realistic geometry of the 3D-printed phantom, which better simulates the complex shapes found in human anatomy. This supports the conclusion that the 3D-printed phantom provides a more accurate representation of human anatomy, as clearly visible when comparing the SA, VLA, and HLA views of the heart in figure 4.6. Furthermore, the consistency in these uptake patterns across different imaging modal-

ities, even at lower doses, suggests that the 3D-printed phantom can effectively replicate clinical scenarios, offering a reliable tool for imaging studies.

In addition, the cross-sectional views (SA, VLA, HLA) reinforce the superior performance of the MyoSPECT over the SPECT. Even at a lower dose protocol, the MyoSPECT provided images that were comparable in quality to those from the SPECT at higher doses. This demonstrates the MyoSPECT's potential to achieve high-quality imaging even with reduced activity levels, which can be particularly advantageous in situations where the availability of radioactive material is limited.

## 5.4 | Comparison between Kiss et al. (2022)'s phantom and the 3D-printed cardiac phantom

One of the study's goals was to compare the performance of the 3D-printed phantom against the original model developed by Kiss et al. (2022). Both phantoms share identical structural designs, thereby requiring the 3D-printed version to replicate the uptake patterns previously documented by Kiss et al. (2022). Furthermore, this comparative analysis serves to confirm whether the modifications introduced affect the phantom's structure and shape. Structural comparisons were visualised through the CT scans in figure 4.7. This figure shows that aside from different orientations of the heart models, all structural features appear identical.

### 5.4.1 | Healthy heart comparison

The comparative analysis between the healthy heart phantom by Kiss et al. (2022) and the 3D-printed phantom demonstrated similar myocardial perfusion patterns, confirming the functional equivalence of both phantoms.

The only notable differences in absolute uptake values are attributable to the different activity levels used during the scans. Kiss et al. (2022) employed 13.83 MBq in the healthy heart phantom

and 11.39 MBq in the defective heart phantom. Whilst, there were only 3-4 MBq in the 3D-printed phantom.

The lower activity in this study reflects more clinically realistic uptake values, thereby ensuring that the findings are more representative of typical clinical scenarios. The use of higher activity levels by Kiss et al. (2022) enhances image quality but does not mimic standard clinical practices, which could have led to exaggerated perfusion patterns and uptake values.

### 5.4.2 | Defective heart comparison

In the defective heart models, the most prominent difference lies in the defect's position due to the variation that needed to be introduced when scanning as a result of the leak. The defect in the 3D-printed phantom is located closer to the LCX region, differing slightly from its position in Kiss et al. (2022)'s model. Despite these differences, the distribution of radioactivity remains consistent, with higher uptake near the LCX and reduced uptake in the LAD and RCA regions, accurately simulating the physiological effects of coronary obstruction in that region. Figure 4.8 illustrates that while the defect's position varies, its representation aligns with that observed in Kiss et al. (2022)'s research.

This confirms the study's success in not only replicating the original phantom but also in enhancing its design to ensure waterproofing without the need for extensive post-processing, achieving the intended improvements.

## 5.5 | Comparison between SPECT and MyoSPECT - Defective heart scenario

This section compares the SPECT and MyoSPECT machines based on the mean and standard deviation of uptake values in different heart segments across varying activity doses. Detailed results

are presented in table 4.11.

A paired t-test was conducted to evaluate statistically significant differences between the SPECT and MyoSPECT measurements, following the methodology outlined in the previous section. For a result to be considered statistically significant, the p-value must be less than 0.05. The results indicated no significant differences in most segments, as most p-values exceeded 0.05. However, the Basal Anterolateral segment showed a significant difference with a p-value below 0.05, suggesting a distinct variation in uptake measurements between the two devices in this segment. This might imply limited advantages of MyoSPECT over SPECT if evaluated solely based on statistical significance across multiple segments.

Despite the statistical analysis, visual inspection of different views i.e the SA, VLA and HLA views reveals crucial insights. For instance, as shown in figure 4.13, the defect definition is notably clearer in MyoSPECT images across all activity levels. Furthermore, a 200 MBq MyoSPECT scan delineates the defect as effectively as a 600 MBq SPECT scan, proving MyoSPECT's superior imaging capabilities in certain views.

The results also suggest the feasibility of using lower doses with MyoSPECT. Making it beneficial in scenarios like delivery delays or shortages of technetium-99m generators. A scenario which occurs once or twice a year in Malta's NM department. In regions dependent on external radiopharmaceutical supplies, such as Malta, MyoSPECT could maintain diagnostic schedules even with reduced isotope availability. This capability ensures timely and efficient patient care, crucial for managing conditions such as cardiac ischemia, where prompt diagnosis is essential for effective treatment.

Overall, while the polar maps show limited differences, the cross-sectional views provided by MyoSPECT demonstrate its potential to enhance clinical outcomes through lower radiation doses and improved image clarity.

## 5.6 | Comparison between SPECT and MyoSPECT - Healthy Heart Scenario

The performance of SPECT and MyoSPECT was also evaluated using a healthy heart phantom, applying ultra-low (200 MBq), normal (400 MBq), and high dose (600 MBq) protocols. The mean and standard deviations of the uptake values are detailed in table 4.13, and the results of the paired t-tests are presented in table 4.14.

The analysis of mean and standard deviation across different heart segments indicates that both systems perform similarly, with minor differences in uptake values, suggesting comparable efficacy.

However, the paired t-test results reveal that certain segments, specifically Basal Anteroseptal and Mid Inferior, exhibit p-values of 0.05 and 0.02, respectively. These findings imply statistically significant differences in these segments, indicating that the discrepancies in uptake values are not due to chance but reflect a real variance in performance between SPECT and MyoSPECT. Further investigations and possibly additional data collection are recommended to validate these results and determine their clinical implications.

The comprehensive evaluation across both defective and healthy phantoms at varying activity levels suggests that the optimal dosage for patient administration should be between 300 MBq and 500 MBq. These dosages demonstrate consistent uptake and maintain image quality, supporting the current practice in Malta of administering up to 400 MBq for two-day tests and 600 MBq for one-day tests. It is important to note that no attenuation correction was simulated in the phantoms, which constitutes a limitation of this study. Future research should address this gap to reinforce the findings discussed in this section. Ultimately, this provides valuable insight into the optimal dose for patients, aiming to maximize image quality while minimizing radiation exposure.

## 5.7 | Conclusion

In conclusion, this discussion has examined the study's objectives, findings, and methodological considerations. The research successfully demonstrated the feasibility of using 3D printing technology to create a waterproof nuclear medicine cardiac phantom, which met the study's objectives of replicating anatomical accuracy and improving imaging performance. Comparisons between different phantoms and imaging modalities revealed significant insights into optimizing imaging techniques and materials for better clinical outcomes. The findings suggest that using MyoSPECT, especially with lower radiation doses, can maintain image quality, making it a viable alternative in scenarios with limited radiopharmaceutical availability. Overall, the study highlights the potential for further innovation in phantom development and imaging practices, underscoring the importance of continued research and collaboration in the field of medical physics. Future work should focus on addressing identified limitations and exploring new materials and technologies to enhance the utility and effectiveness of 3D-printed phantoms in nuclear medicine.

# 6

# Conclusions and Recommendations

## 6.1 | Introduction

This chapter summarizes the key findings of the study, outlines practical recommendations for professionals in medical physics and radiation protection, and suggests avenues for future research. By reflecting on the study's conclusions, this chapter aims to provide insights into how the research can be applied in clinical practice to enhance patient care and safety. Additionally, it offers guidance for further investigation to build on the advancements achieved in this work and explore new possibilities within the field of nuclear medicine and 3D printing technology.

## 6.2 | Summary of Conclusions from the Study

The study yielded several key conclusions, which are summarized as follows:

- For FDM based 3D printers, PETG was identified as the most suitable material for creating phantoms. The optimal 3D-printing parameters to produce watertight structures with thin walls were established and are detailed in Table 4.1. These parameters successfully generated waterproof prints without requiring any post-processing steps.
- A new post-processing technique using impregnation technology was explored, proving more effective than the traditional method of applying multiple layers of acrylic paint. This

method ensures that not only the outer surface of the print becomes watertight but also every internal layer, effectively sealing the phantom from the inside out.

- The study successfully collaborated with another project, demonstrating the versatility of 3D-printing technology in performing complex, tailored tests that medical physicists can use to enhance patient care.
- The comparison between SPECT and MyoSPECT systems demonstrated the superior imaging capabilities of the MyoSPECT, particularly at lower doses. This finding supports the potential use of MyoSPECT in situations where radiopharmaceutical availability is limited. Supporting its need in the NM department.
- Various activity doses were evaluated to determine the optimal range for patient administration. The results suggest that doses between 300 MBq and 500 MBq provide sufficient image quality on both machines while minimizing radiation exposure, which is consistent with current practices in Malta.

## 6.3 | Recommendations for Professional Practice

Based on the study findings, the following recommendations are suggested for professionals in medical physics, radiation protection, and radiography practice:

- Printing with FDM based printers should be conducted in a controlled environment, as fluctuations in temperature and humidity can significantly impact the printing process, particularly during the extended print times required for these phantoms, which were over 18 hours in all cases. To mitigate these environmental effects, it is recommended to use an air management attachment or enclosure for each printer. Different manufacturers offer various accessories for this purpose. Based on extensive research, Ultimaker's air management system, which is a simple overhead attachment for their semi-enclosed printer, is suggested as an effective solution.

- It is crucial to thoroughly dry all 3D-printing materials before printing, especially PETG, to prevent moisture from affecting the print quality. Manufacturers typically provide dedicated drying systems, and some offer material management systems designed to keep materials dry for longer periods.
- During the study, it was found that Ultimaker's glass build plate became chipped in two prints due to the printing parameters and extended print duration. It is recommended to further investigate methods to prevent such damage, ensuring the longevity of the build plate and maintaining print quality.
- Medical physics departments should consider integrating 3D printing technology to develop custom phantoms tailored to specific clinical needs. This can enhance diagnostic accuracy and treatment planning by providing anatomically accurate models.
- Based on the study's findings, it is recommended that healthcare providers standardize the use of activity doses between 300 MBq and 500 MBq for cardiac imaging to balance image quality and patient safety. Both the SPECT and MyoSPECT systems maintained very similar image quality at these dose levels.

## 6.4 | Recommendation for Future Research

Suggestions for future research include:

- Conduct the same study using an anthropomorphic thoracic phantom to better simulate actual clinical attenuation conditions. This approach would provide more clinically relevant data on the performance of the SPECT and MyoSPECT systems under realistic conditions.
- Conduct the same study using an anthropomorphic thoracic phantom which mimics the uptake in other organs too. To investigate the effect of their uptake on MPI.
- Future research should explore the use of phantoms with smaller defects to determine the minimum detectable defect size for both SPECT and MyoSPECT systems. This would offer valuable insights into each machine's sensitivity and accuracy in detecting small defects,

allowing for a direct comparison of their performance in identifying minimal anatomical abnormalities.

- Investigate the use of resin-based printers to produce the same phantom used in this study. These printers, which have finer layers, may produce phantoms of higher quality than those produced by FDM-based printers, potentially offering improved resolution and wall transparency.
- The study's findings on watertight 3D-printing parameters open up possibilities in the field of microfluidic systems within healthcare and nuclear applications. Potential applications include:
  - Creating microfluidic chips with superior liquid volume flow and control, enhancing the precision of pharmaceutical dosing.
  - Developing 3D-printed microfluidic systems to replace animal testing by using microscopic cell cultures that replicate human organs. This method allows for pharmaceuticals to be tested in a more human-relevant model, improving safety and reducing the reliance on animal testing.
  - Producing micro-spherical capsules to contain nuclear fusion fuel, such as deuterium, tritium, or helium, to facilitate and sustain nuclear fusion reactions.
  - Fabricating small capsules containing protocells or artificial cells for studying membrane-protein interactions.
  - Encapsulating stem cells in microscopic capsules for potential use in repairing spinal cord damage.
- By shifting focus to resin-based printers or using softer FDM materials, the techniques learnt from this study could be applied to 3D-print artificial breast replacements for breast cancer survivors, artificial ears, potentially incorporating the patient's own tissue cells, and customised orthopaedic casts to improve the comfort and functionality of recovery and immobilisation devices.

- Collaboration with biomedical engineering teams could enable the development of advanced, functional prosthetic limbs with live and haptic feedback. Combined with rapid advancements in machine learning, this technology could significantly enhance the accessibility and quality of life for patients requiring prosthetic devices.

## 6.5 | Conclusion

In conclusion, this research successfully fulfilled its primary objectives. The study identified optimal printing parameters and materials to fabricate watertight cardiac phantoms, even with thin walls, without requiring extensive post-processing. This significant finding demonstrates the potential for improving clinical practice by providing durable, customizable, and anatomically accurate phantoms tailored to specific diagnostic and therapeutic needs.

The comparison between the SPECT and MyoSPECT systems confirmed MyoSPECT's superior imaging capabilities, especially at lower doses, thereby supporting its use in scenarios with limited radiopharmaceutical availability. Additionally, the research highlighted the versatility of 3D printing in creating various phantoms for medical applications, emphasizing its role in enhancing diagnostic accuracy and patient care.

By exploring new materials and methodologies, this study also opens the door for future research into microfluidic systems and advanced prosthetics, broadening the scope of 3D printing in medical physics. The collaborative nature of this project and its interdisciplinary approach underscore the importance of innovation and teamwork in advancing medical technologies. This foundation will continue to drive future research, ultimately improving patient outcomes and healthcare services.

# A

# Full scan reconstructions of all the tests conducted

# A.1 | Data Spectrum Phantom - MyoSPECT

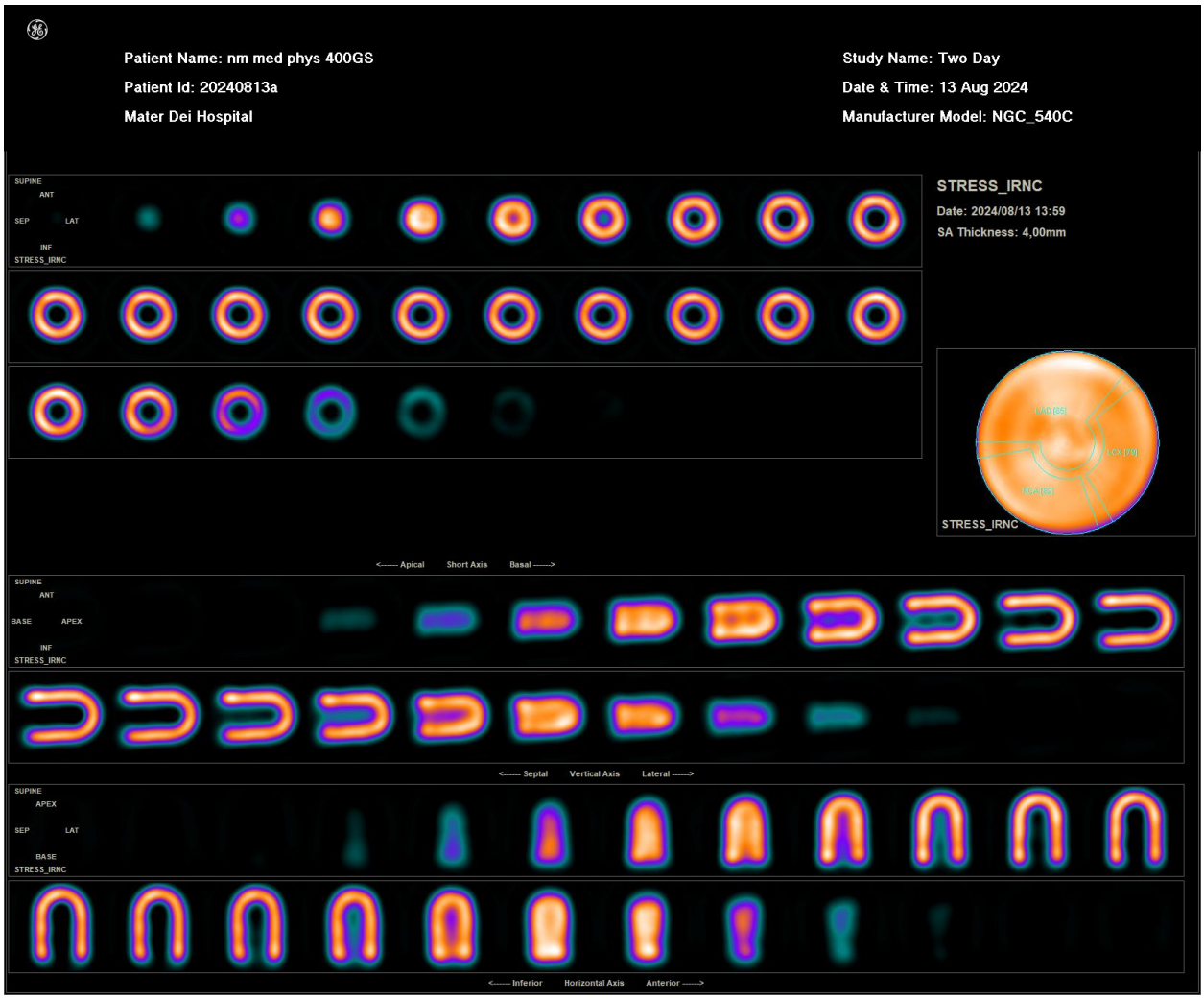

# A.2 | Data Spectrum Phantom - SPECT

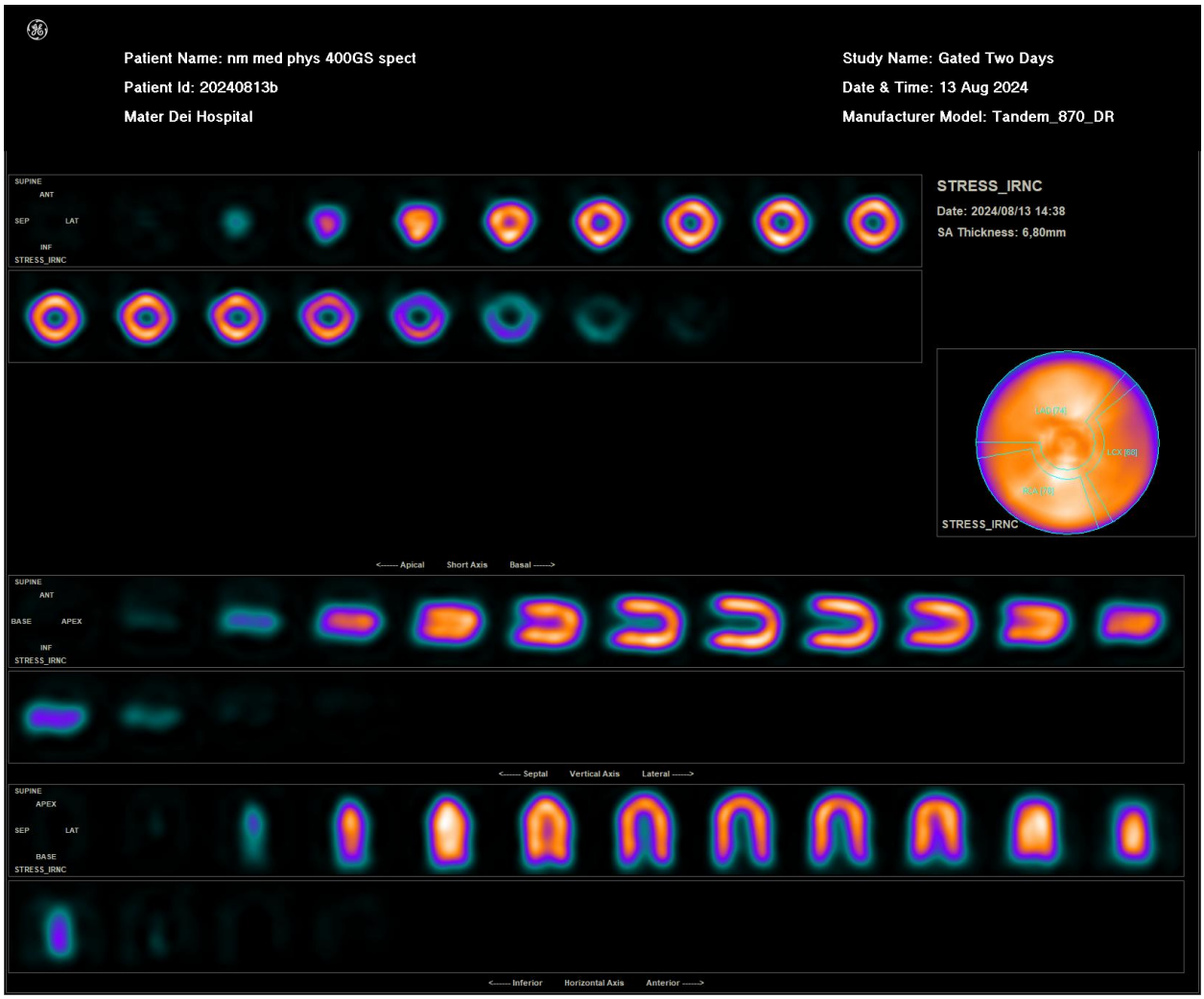

# A.3 | 3D-printed phantom - 200 MBq - MyoPECT

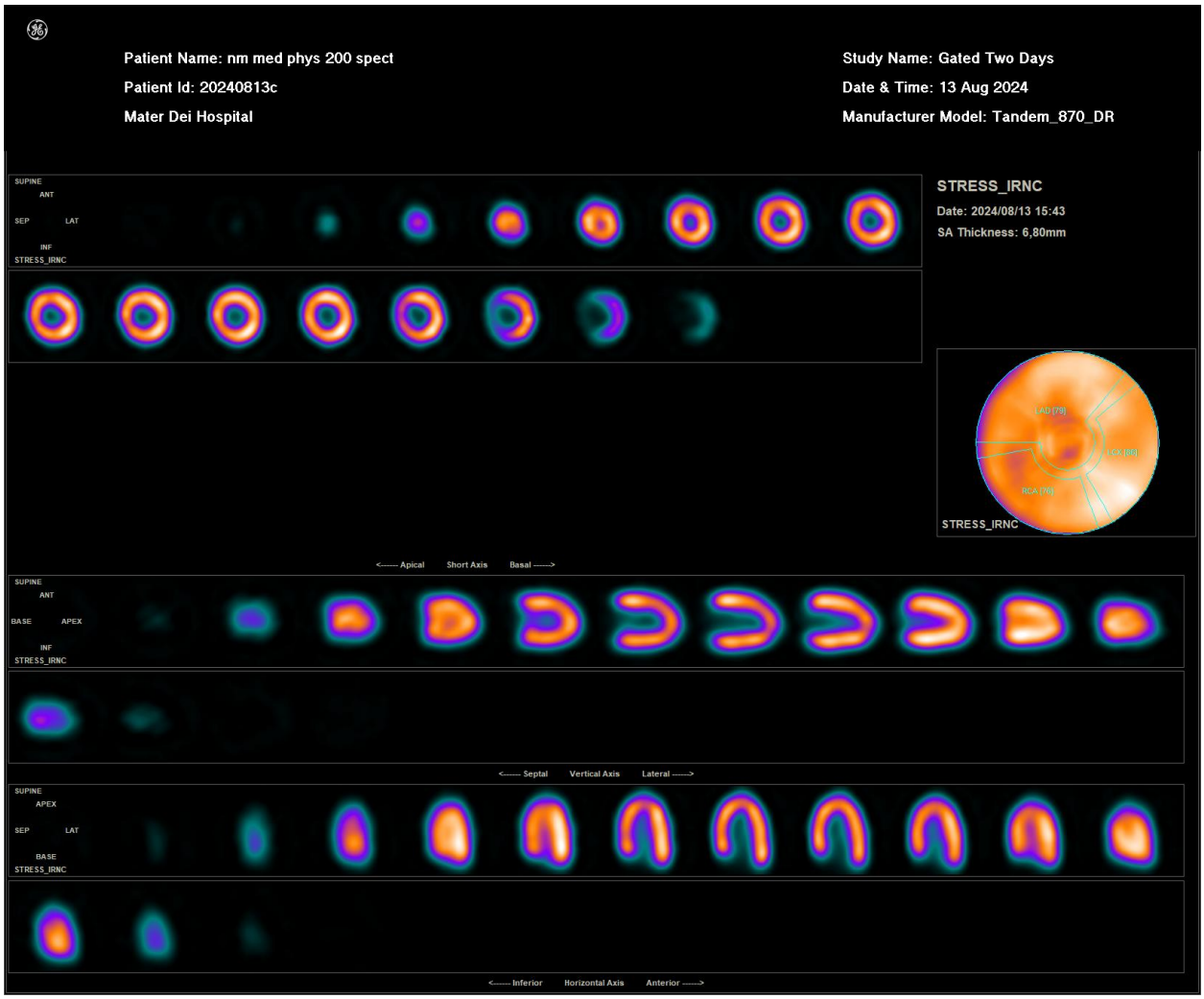

# A.4 | 3D-printed phantom - 200 MBq - SPECT

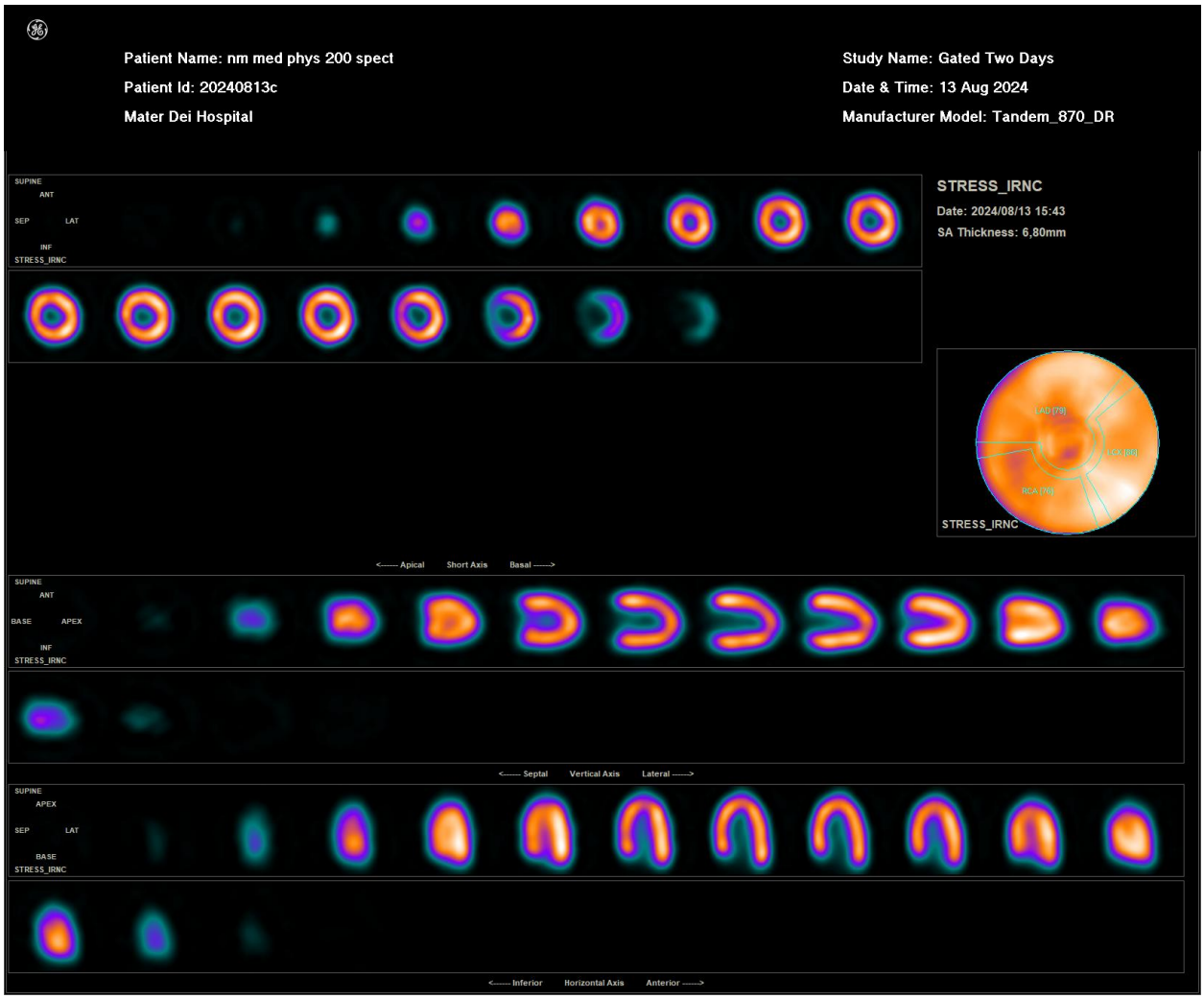

# A.5 | 3D-printed phantom - 400 MBq - MyoPECT

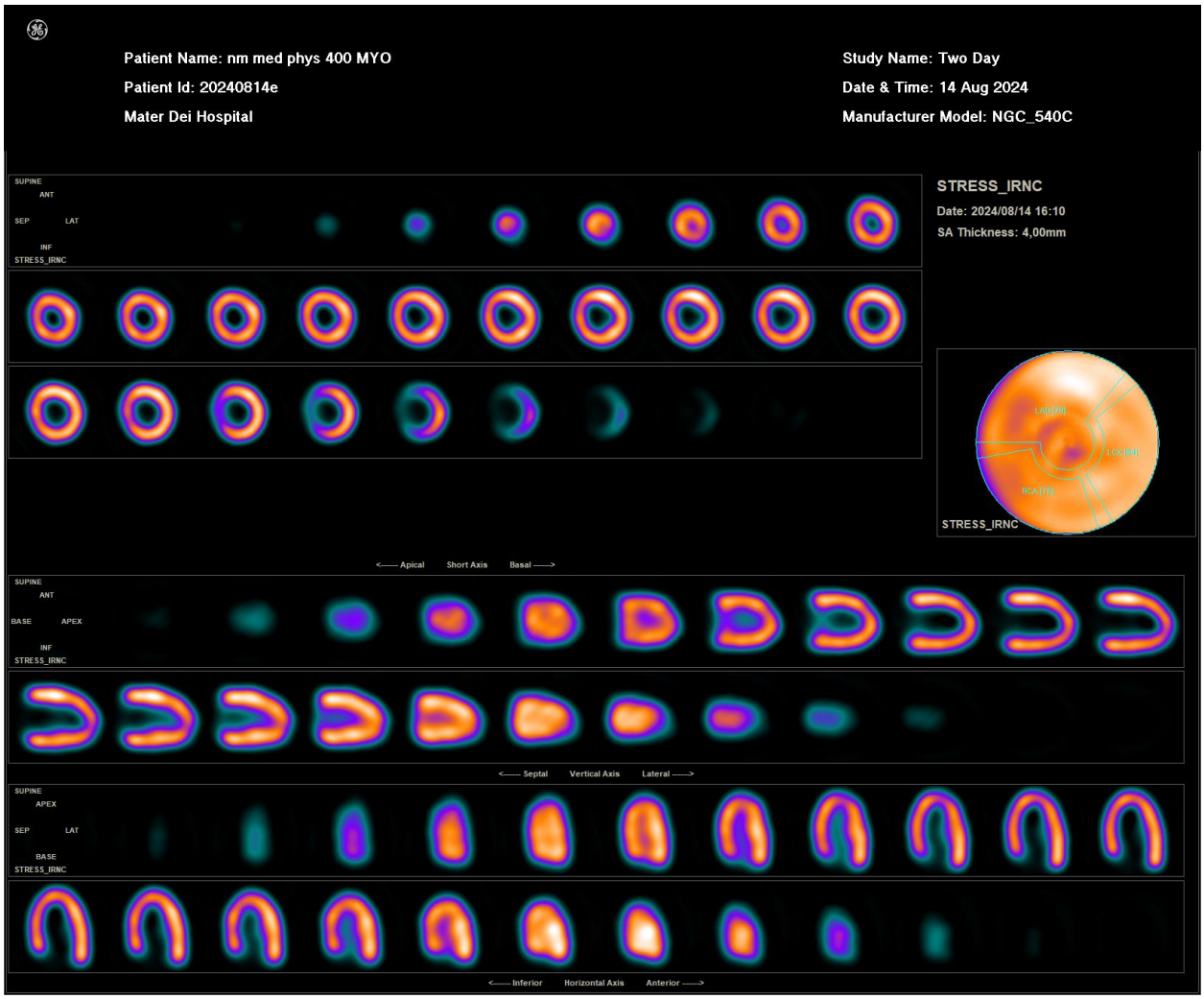

# A.6 | 3D-printed phantom - 400 MBq - SPECT

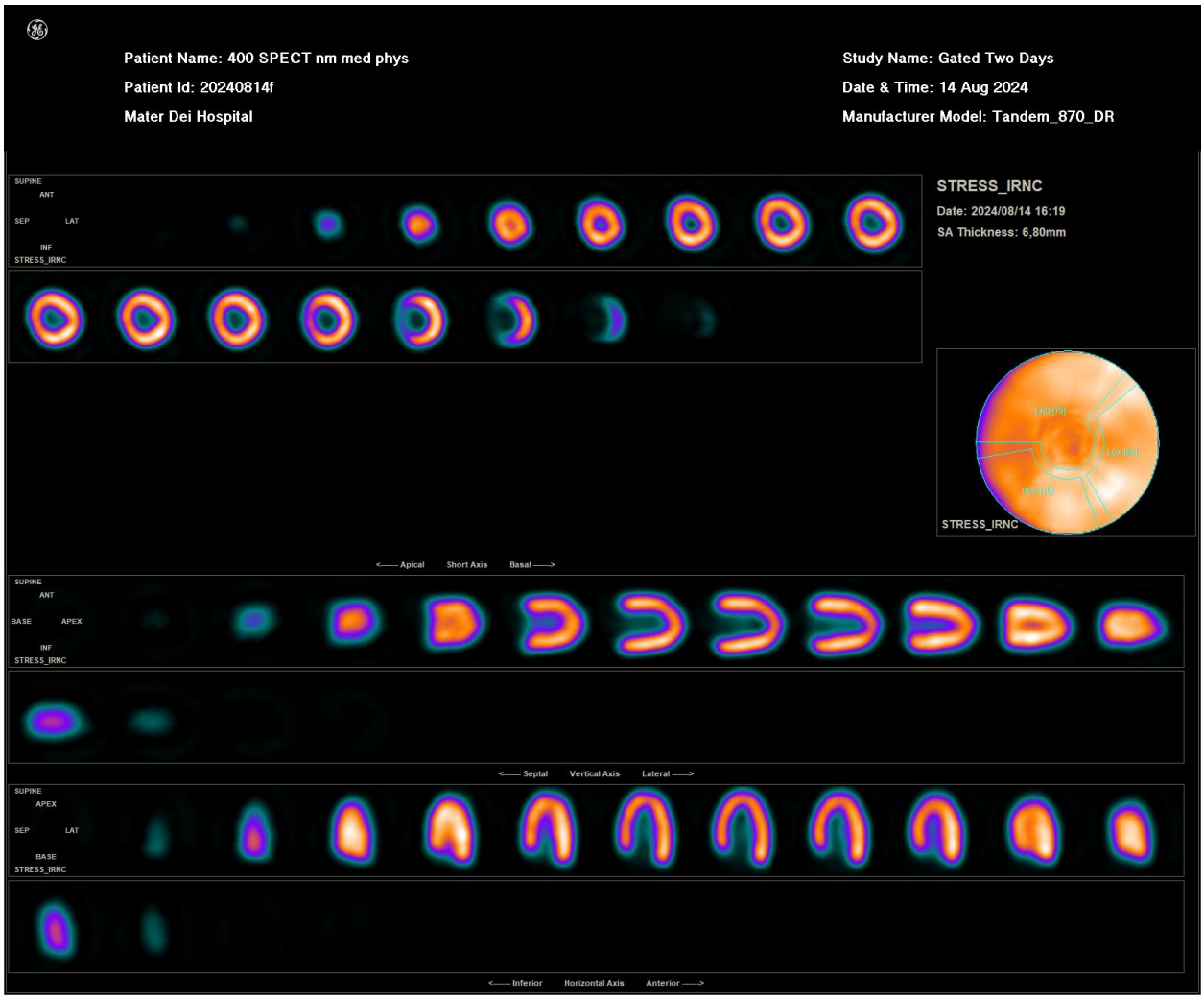

# A.7 | 3D-printed phantom - 600 MBq - MyoPECT

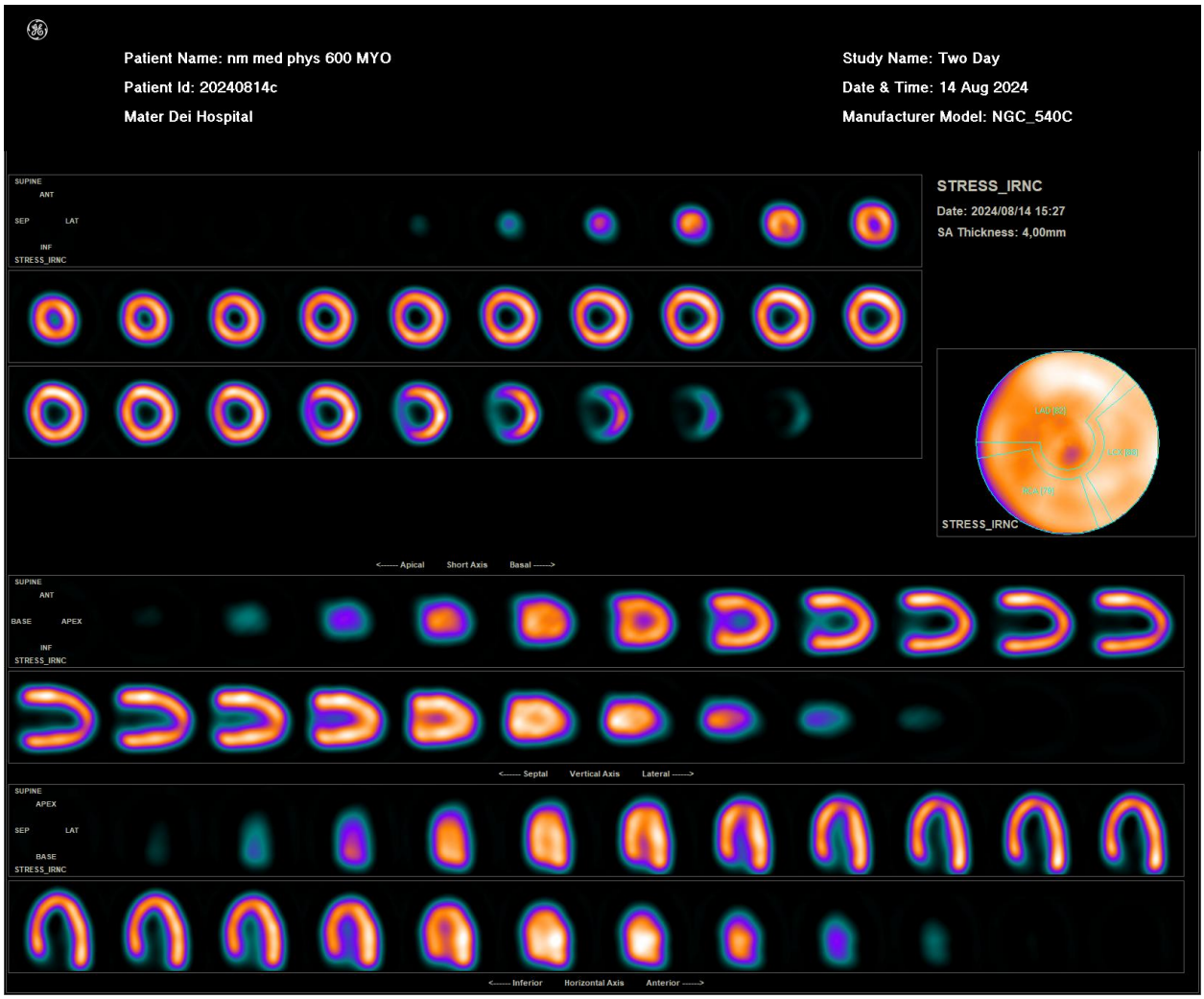

# A.8 | 3D-printed phantom - 600 MBq - SPECT

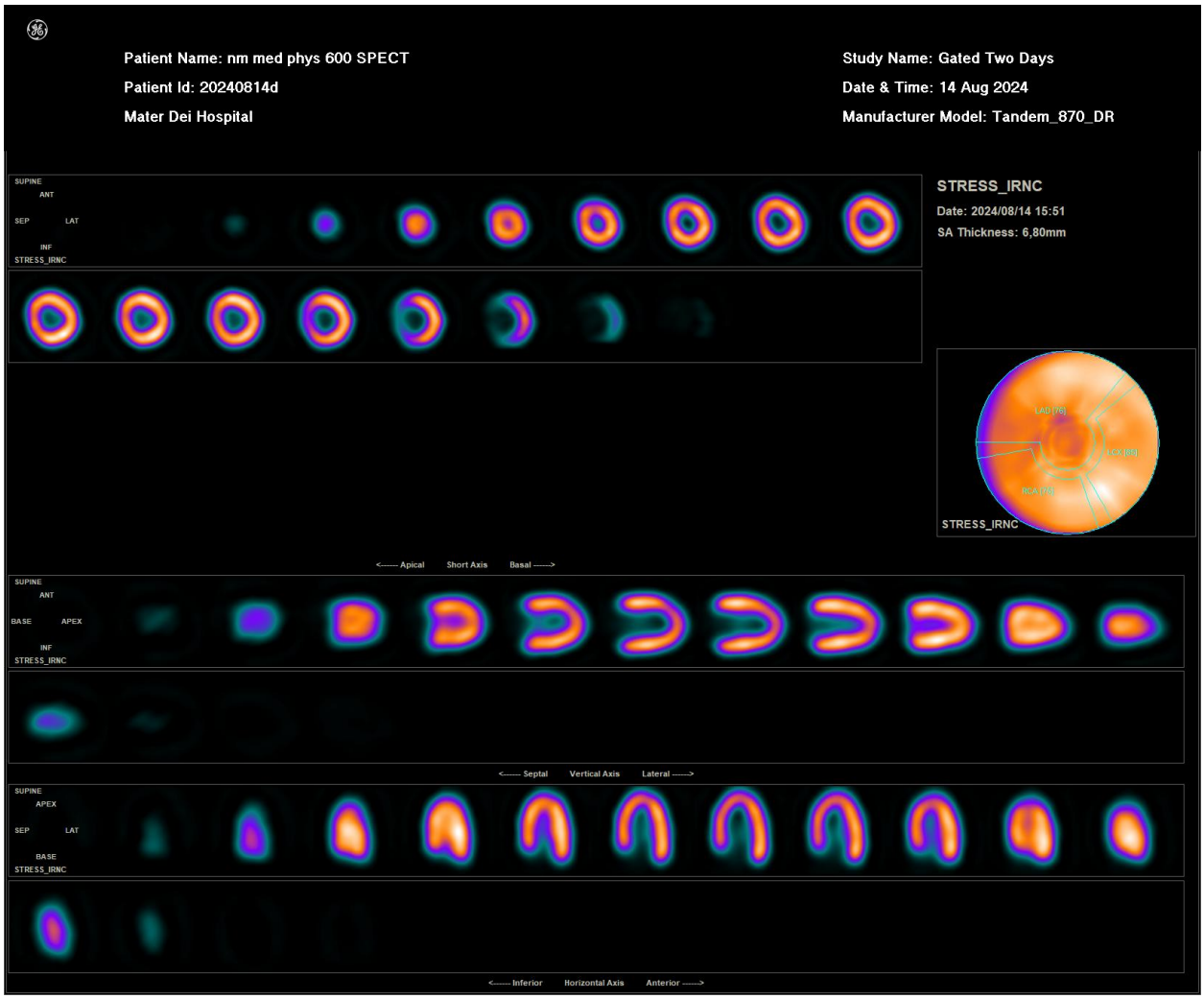

# A.9 | Defective heart imaged on MyoSPECt - 2 MBq

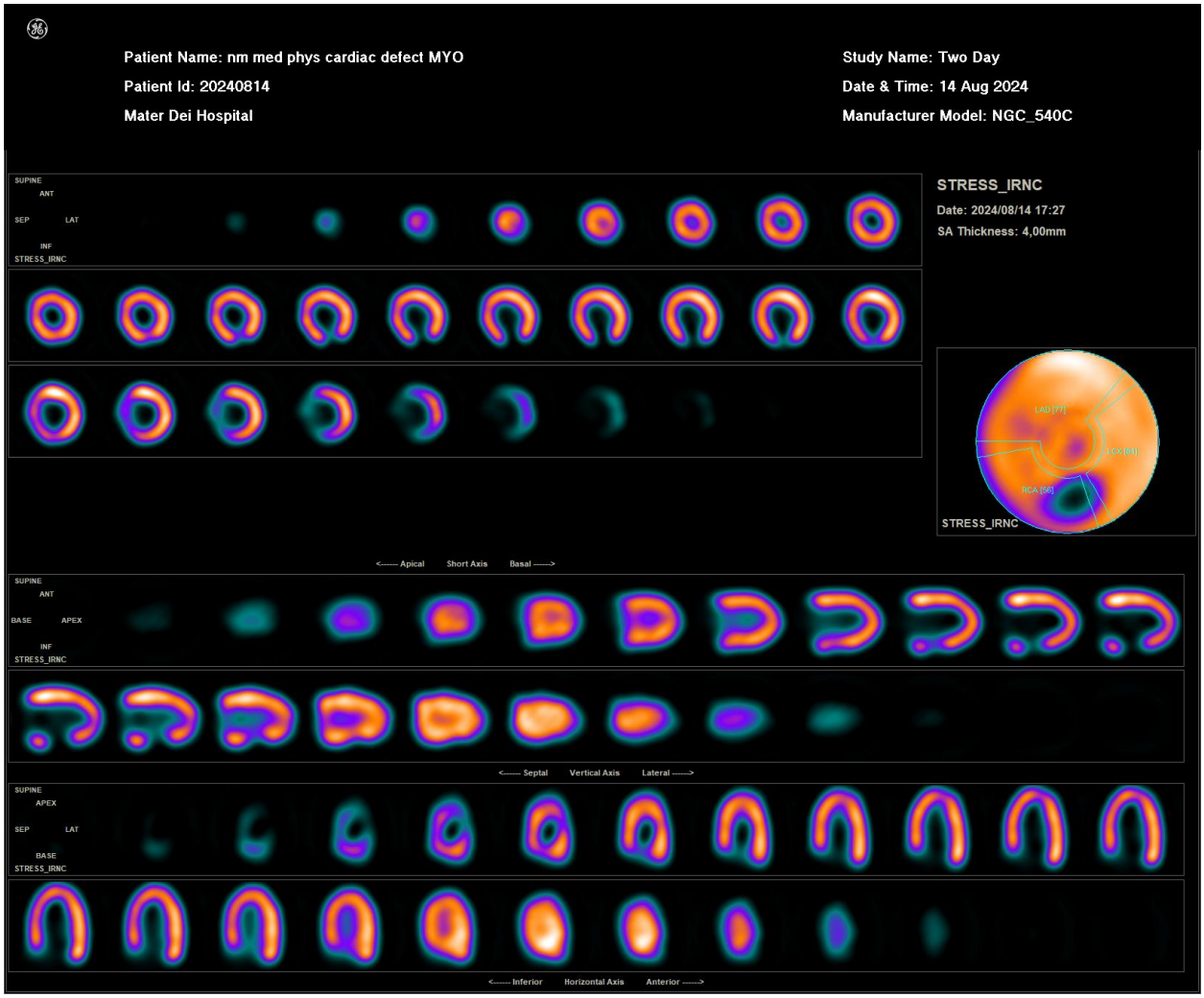

# A.10 | Defective heart imaged on MyoSPECt - 3 MBq

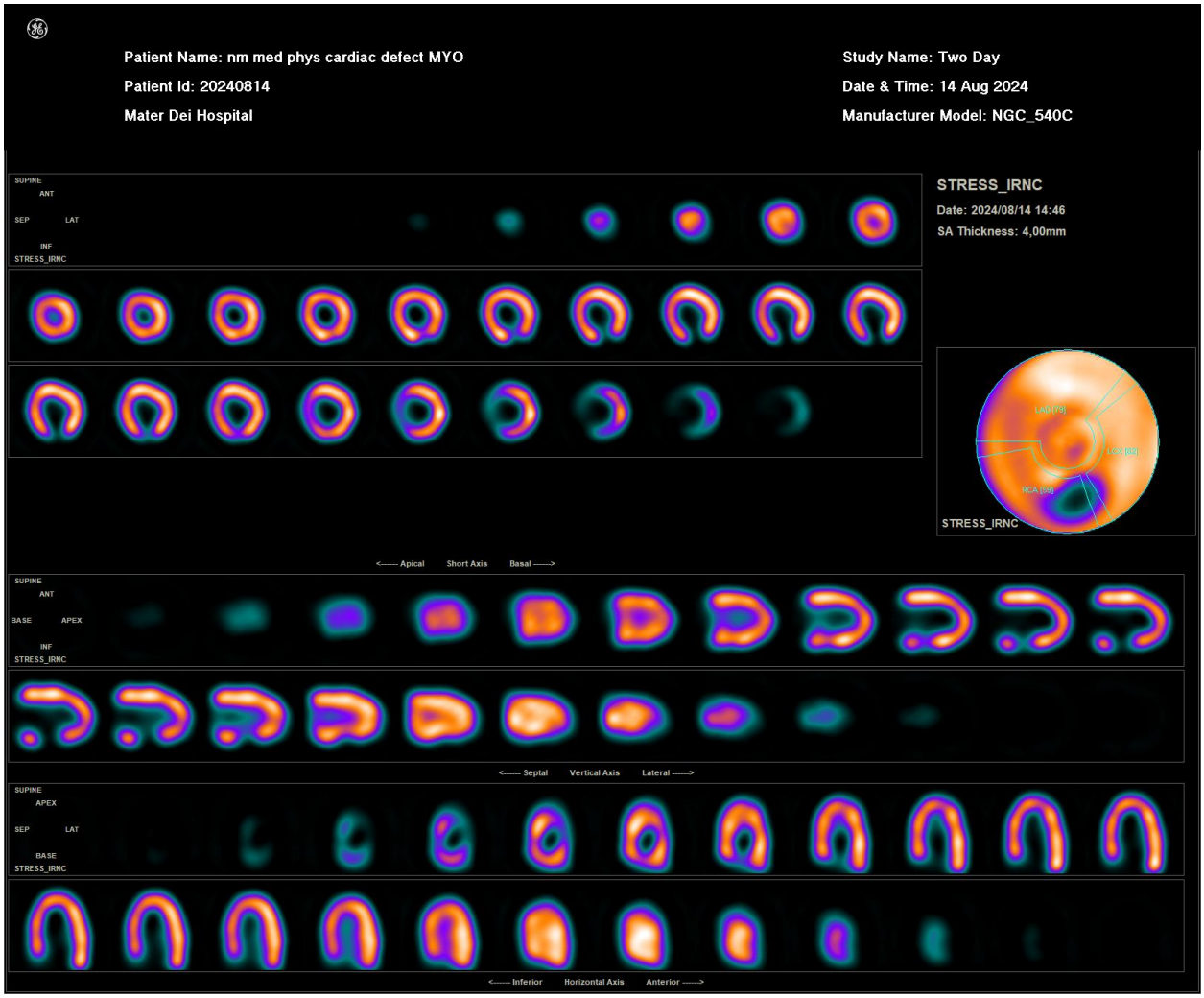

# A.11 | Defective heart imaged on MyoSPECt - 4 MBq

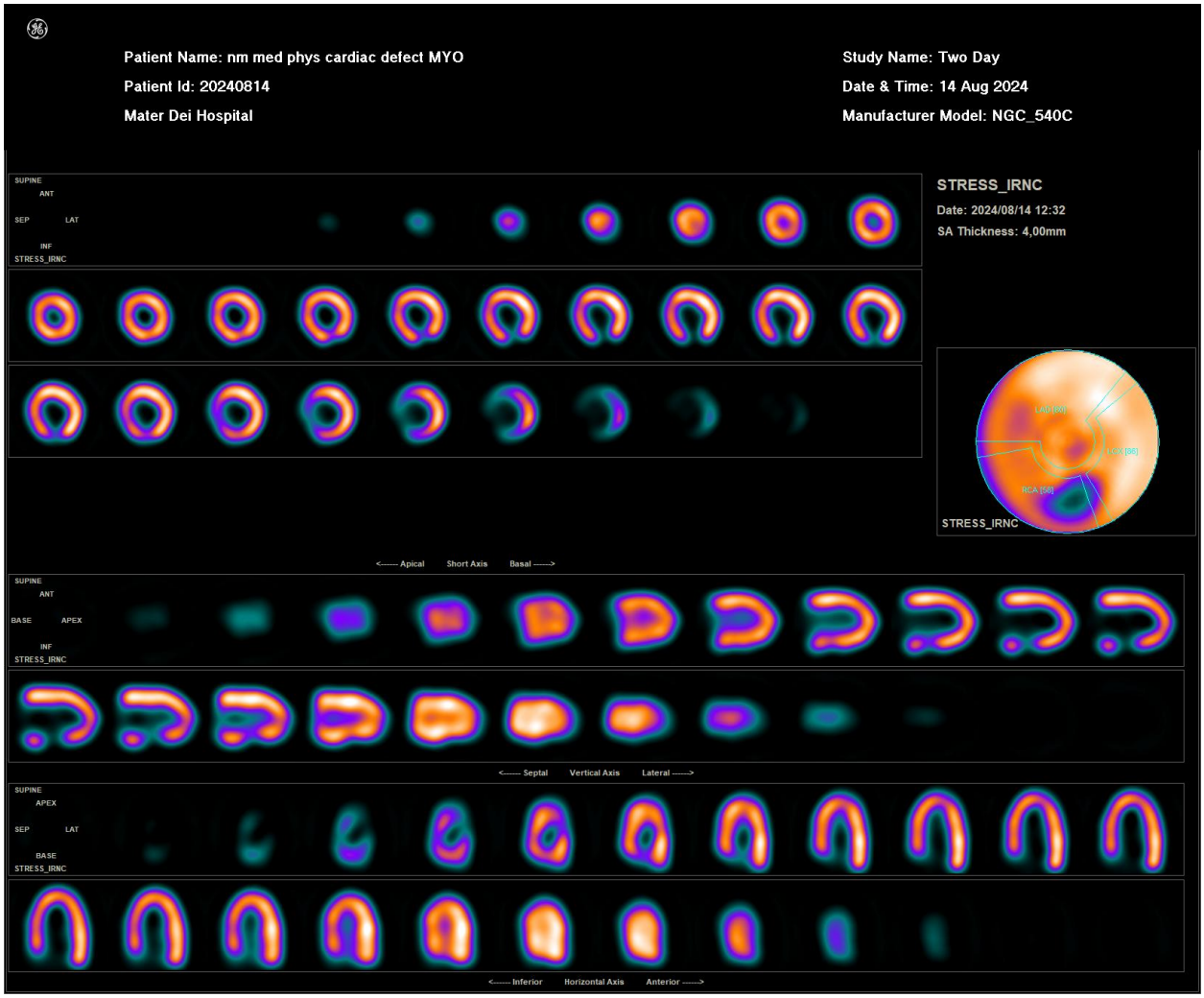

# A.12 | Defective heart imaged on MyoSPECt - 5 MBq

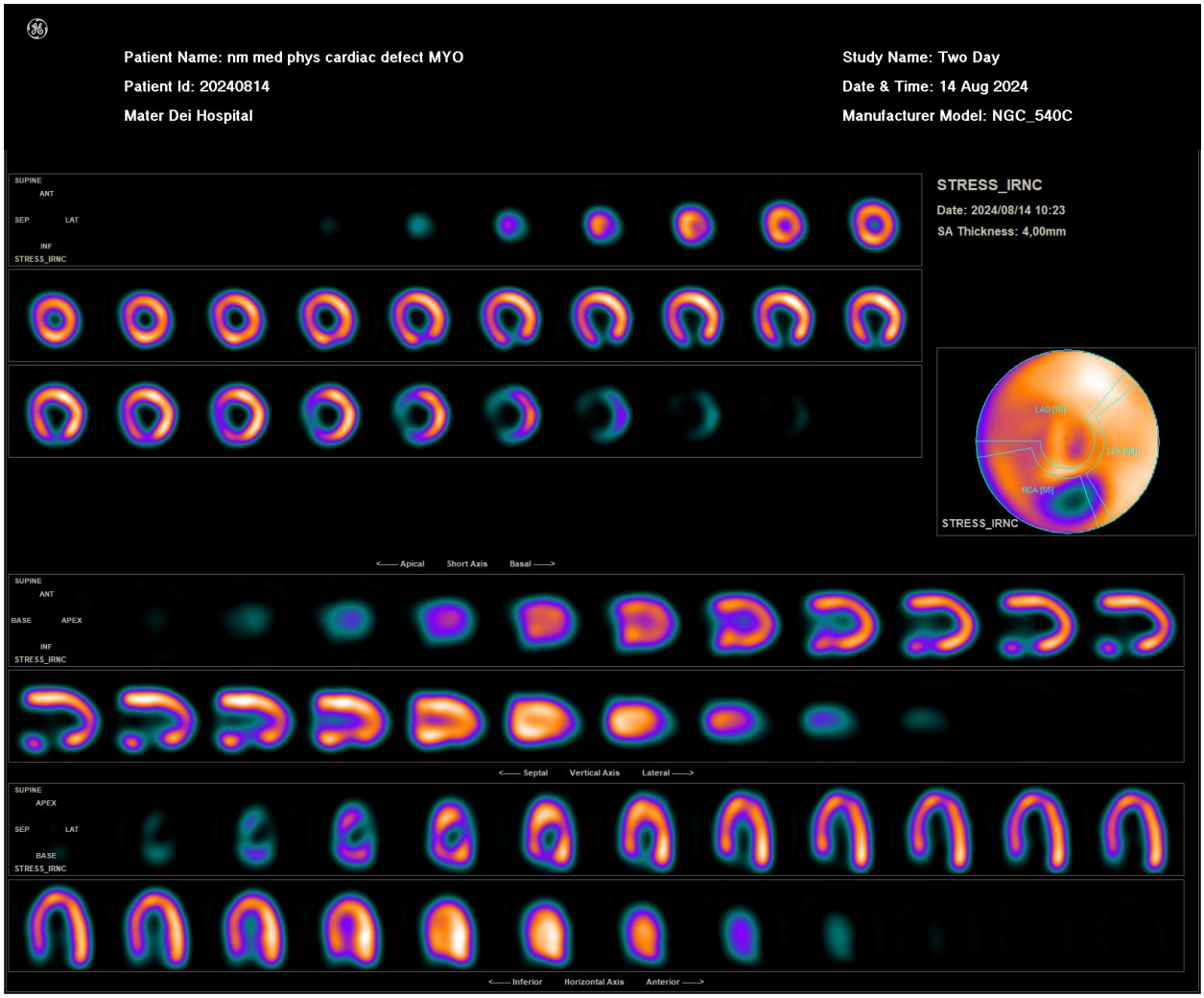

# A.13 | Defective heart imaged on MyoSPECt - 6 MBq

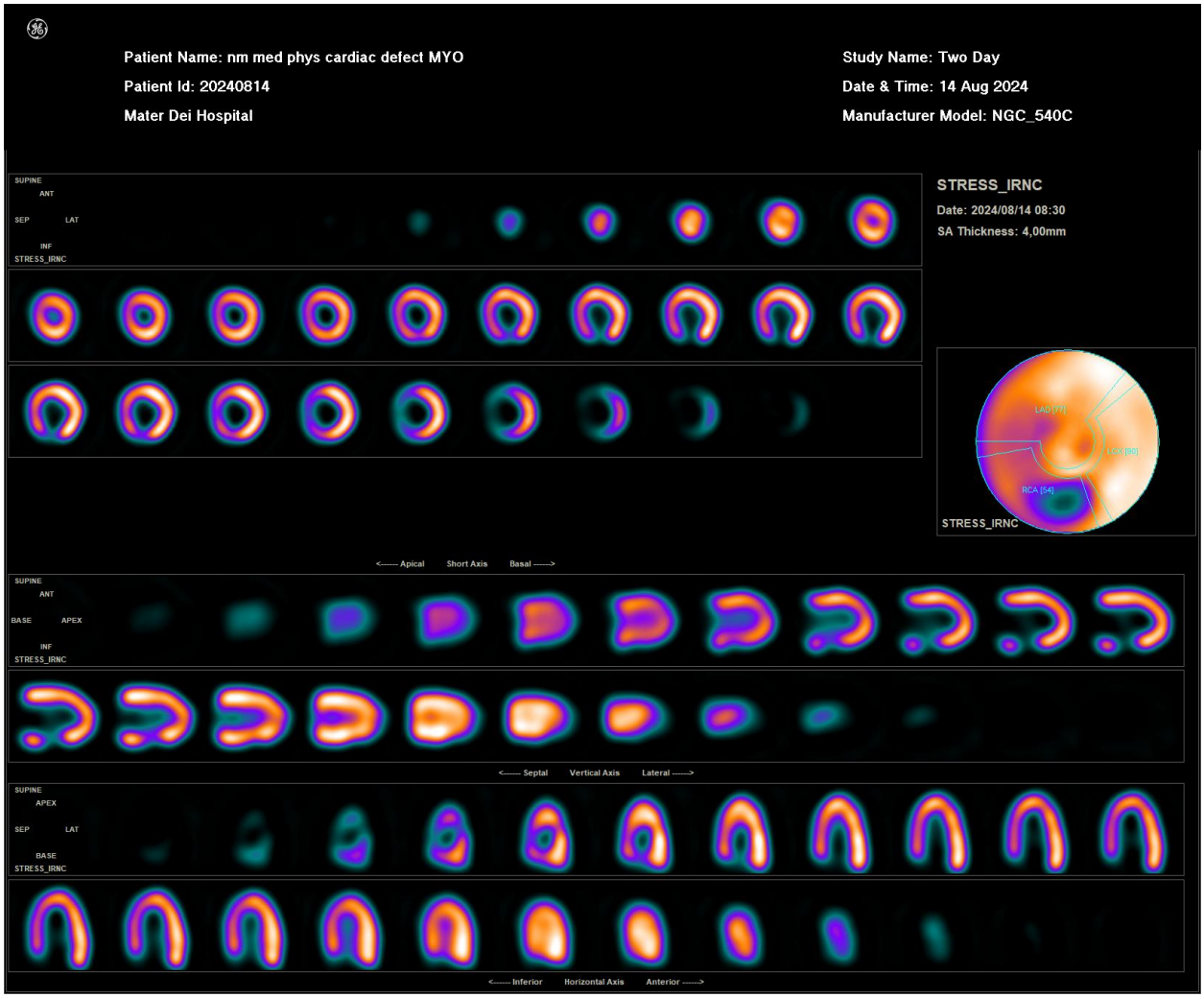

# A.14 | Defective heart imaged on SPECt - 2 MBq

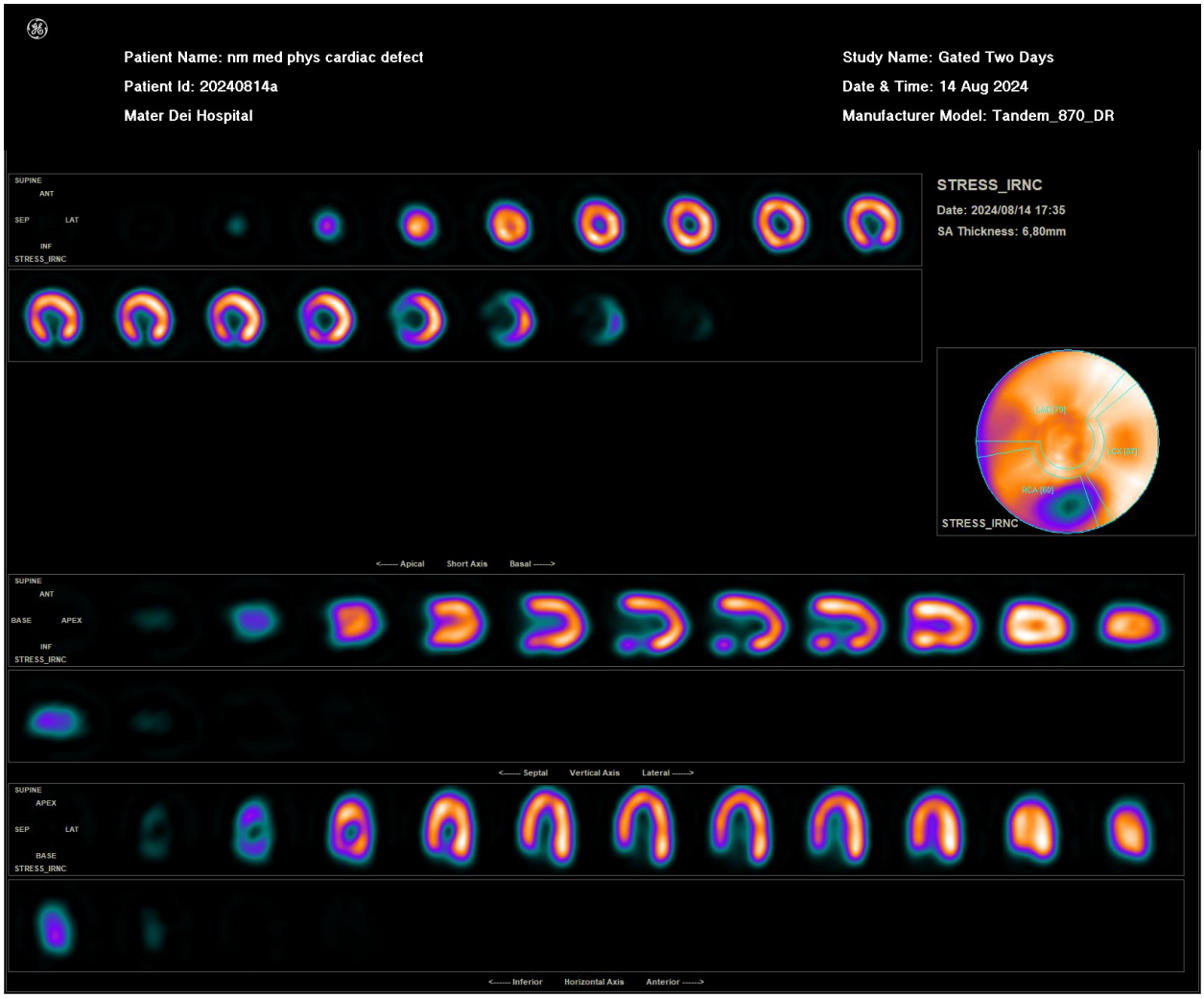

# A.15 | Defective heart imaged on SPECt - 3 MBq

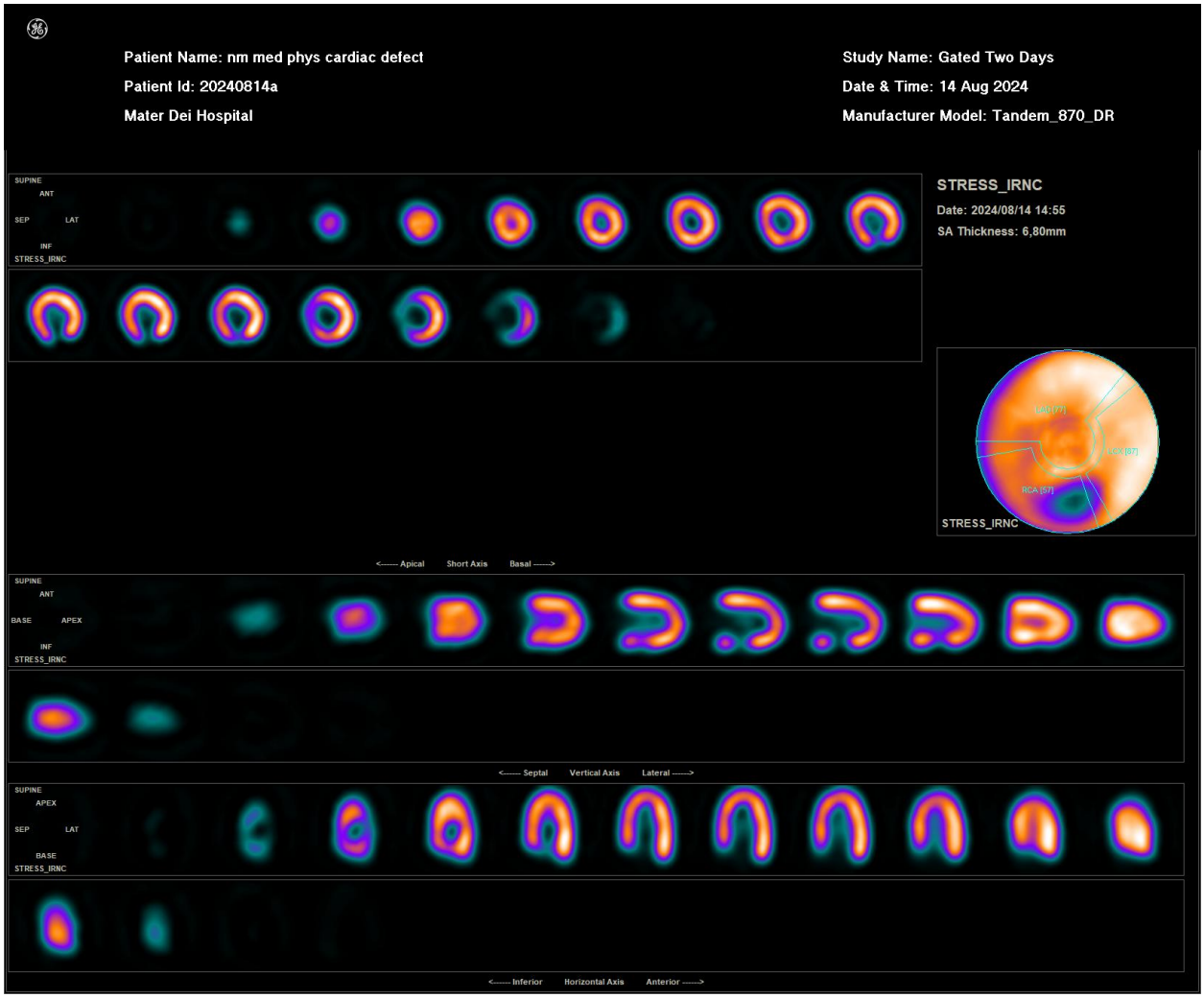

# A.16 | Defective heart imaged on SPECt - 4 MBq

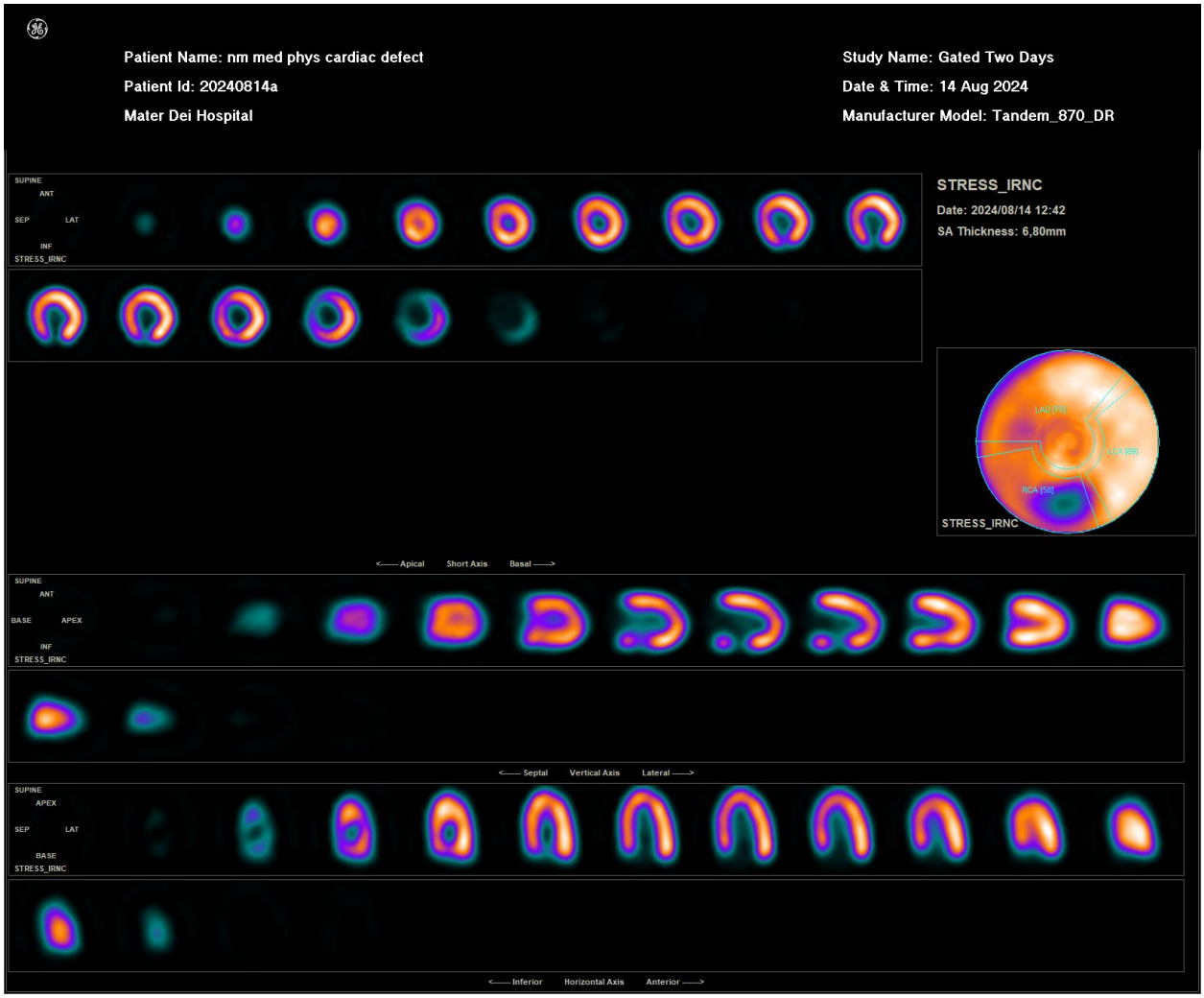

# A.17 | Defective heart imaged on SPECt - 5 MBq

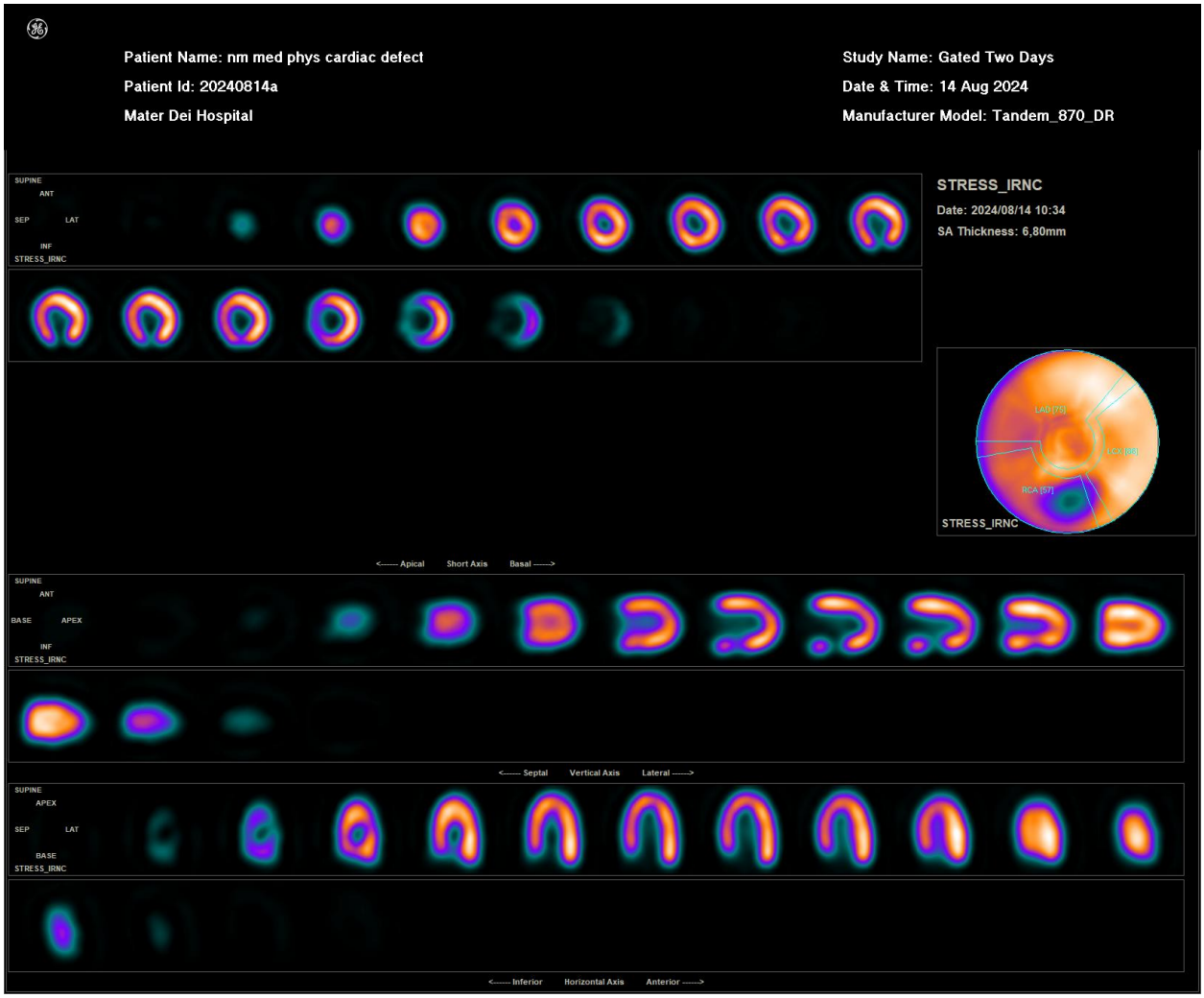

# A.18 | Defective heart imaged on SPECt - 6 MBq

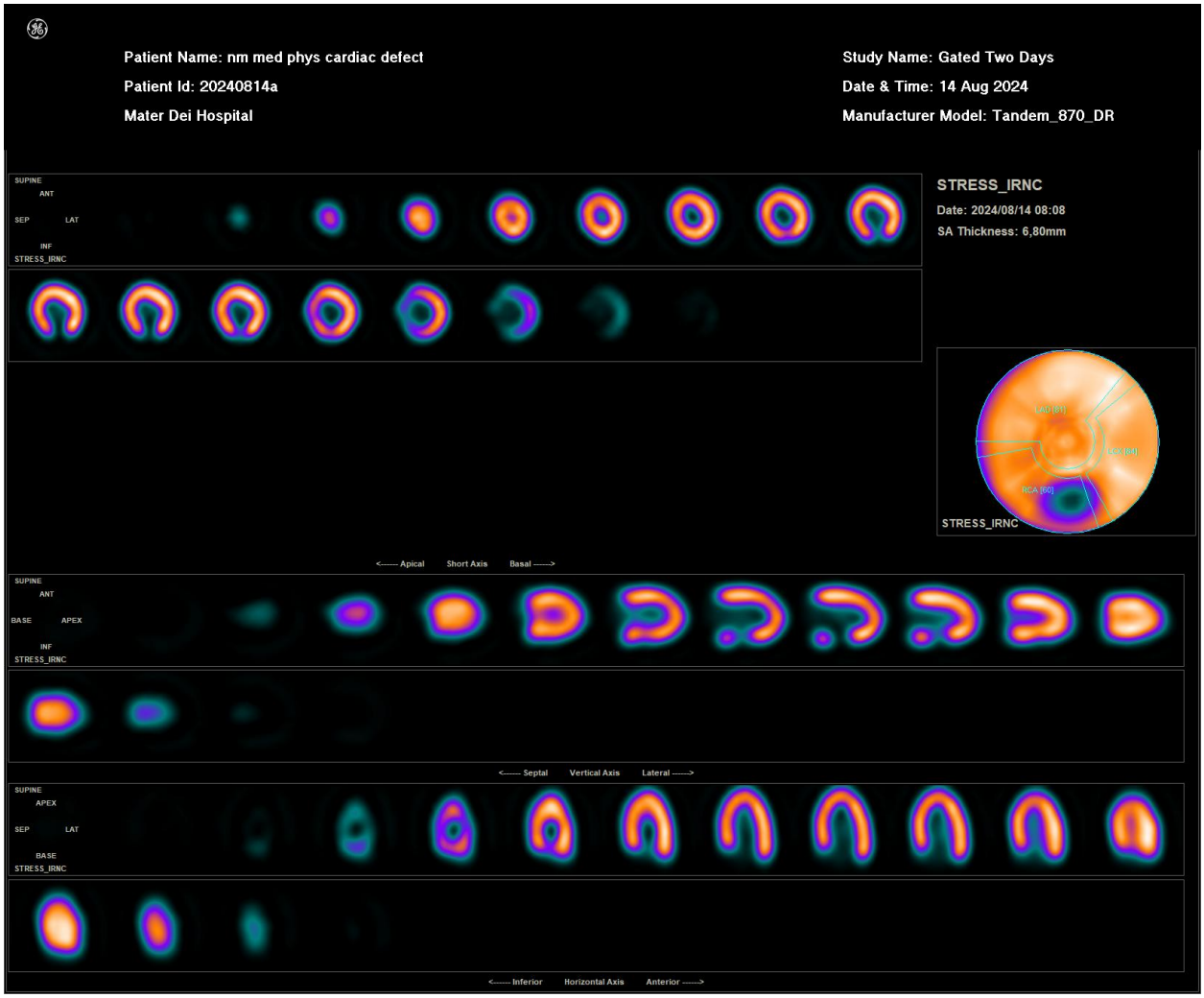

# References


Denis Agostini, Pierre-yves Marie, Simona Ben-haim, François Rouzet, Bernard Songy, Alessandro Giordano, Alessia Gimelli, Fabien Hyafil, Roberto Sciagrà, Jan Bucerius, Hein J. Verberne, Riemer H. Slart, J, A, and Oliver Lindner. Performance of cardiac cadmium-zinc-telluride gamma camera imaging in coronary artery disease: a review from the cardiovascular committee of the european association of nuclear medicine (eanm). *European Journal of Nuclear Medicine and Molecular Imaging*, 43(13):2423–2432, December 2016a. ISSN 16197070. doi: 10.1007/s00259-016-3467-5.

Denis Agostini, Pierre-yves Marie, Simona Ben-haim, François Rouzet, Bernard Songy, Alessandro Giordano, Alessia Gimelli, Fabien Hyafil, Roberto Sciagrà, Jan Bucerius, Hein J. Verberne, Riemer H. Slart, J, A, and Oliver Lindner. Performance of cardiac cadmium-zinc-telluride gamma camera imaging in coronary artery disease: a review from the cardiovascular committee of the european association of nuclear medicine (eanm). *European Journal of Nuclear Medicine and Molecular Imaging*, 43(13):2423–2432, December 2016b. ISSN 16197070. doi: 10.1007/s00259-016-3467-5.

American Heart Association Writing Group on Myocardial Segmentation AHA, Registration for Cardiac Imaging:, Manuel D. Cerqueira, Neil J. Weissman, Vasken Dilsizian, Alice K. Jacobs, Sanjiv Kaul, Warren K. Laskey, Dudley J. Pennell, John A. Rumberger, Thomas Ryan, and Mario S. Verani. Standardized myocardial segmentation and nomenclature for tomographic imaging of the heart. *Circulation*, 105(4):539–542, January 2002. doi: 10.1161/hc0402.102975.

C Anagnostopoulos, M Harbinson, A Kelion, K Kundley, C Loong, A Notghi, E Reyes, W Tindale, and S Underwood. Procedure guidelines for radionuclide myocardial perfusion imaging. *Heart*, 90(Suppl 1):i1–i10, January 2004. ISSN 1355-6037. doi: 10.1136/heart.90.suppl_1.i1.

Moshe Bocher, Ira M. Blevis, Leonid Tsukerman, Yigal Shrem, Gil Kovalski, and Lana Volokh. A fast cardiac gamma camera with dynamic spect capabilities: design, system validation and future potential. *European Journal of Nuclear Medicine and Molecular Imaging*, 37(10):1887–1902, October 2010. ISSN 1619-7089. doi: 10.1007/s00259-010-1488-z.

Robert O. Bonow, Douglas L. Mann, Douglas P. Zipes, and Peter Libby. *Braunwald's Heart Disease: A Textbook of Cardiovascular Medicine*. Elsevier Health Sciences, 9 edition, 2011.

Maura Borrego, Elliot P Douglas, and Catherine T Amelink. Quantitative, qualitative, and mixed research methods in engineering education. *Journal of Engineering education*, 98(1):53–66, 2009.

Alessandra Boschi, Licia Uccelli, Lorenza Marvelli, Corrado Cittanti, Melchiore Giganti, and Petra Martini. Technetium-99m radiopharmaceuticals for ideal myocardial perfusion imaging: Lost and found opportunities. *Molecules*, 27(4): 1188, February 2022. ISSN 1420-3049. doi: 10.3390/molecules27041188.

Felipe Castaneda. Cardiff university: Accessible 3d printed microfluidic devices, March 2017. URL `https://ultimaker.com/learn/cardiff-university-accessible-3d-printed-microfluidic-devices/`.

Xiongchao Chen, Bo Zhou, Xueqi Guo, Huidong Xie, Qiong Liu, James S. Duncan, Albert J. Sinusas, and Chi Liu. Dudocfnet: Dual-domain coarse-to-fine progressive network for simultaneous denoising, limited-view reconstruction, and attenuation correction of cardiac spect. *IEEE Transactions on Medical Imaging*, page 1–1, 2024a. ISSN 1558-254X. doi: 10.1109/TMI.2024.3385650.

Zi-An Chen, Jia-Jia Lin, Hou-Ting Yang, Hsin-Ning Wang, and Jing-Ren Tseng. Assessment of left ventricular ejection fraction in patients with small hearts using gated myocardial perfusion spect: A comparison between conventional spect and myospec. 37(1):12–20, March 2024b. doi: 10.6332/ANMMI.202403_37(1).0002.

F. Costa. Evaluation of the d-spect system: region centric acquisition and tracer kinetics. 2012. URL `https://www.semanticscholar.org/paper/Evaluation-of-the-D-Spect-system%3A-region-centric-Costa/f1cb63ad619c086a6500756efff306736fac92f4`.

Andrew Crean, David Dutka, and Richard Coulden. Cardiac imaging using nuclear medicine and positron emission tomography. *Radiologic Clinics*, 42(3):619–634, May 2004. ISSN 0033-8389, 1557-8275. doi: 10.1016/j.rcl.2004.03.002.

E. Gordon DePuey. Traditional gamma cameras are preferred. *Journal of Nuclear Cardiology*, 23(4):795–802, August 2016. ISSN 1532-6551. doi: 10.1007/s12350-016-0460-0.

Sharmila Dorbala. Standard myocardial perfusion and cardiac fdg pet protocols and associated patient radiation doses. 2012.

W. Lane Duvall, Krista A. Guma, Jacob Kamen, Lori B. Croft, Michael Parides, Titus George, and Milena J. Henzlova. Reduction in occupational and patient radiation exposure from myocardial perfusion imaging: Impact of stress-only imaging and high-efficiency spect camera technology. *Journal of Nuclear Medicine*, 54(8):1251–1257, August 2013. ISSN 0161-5505, 2159-662X. doi: 10.2967/jnumed.112.112680.

Kjell Erlandsson, Krzysztof Kacperski, Dean van Gramberg, and Brian F. Hutton. Performance evaluation of d-spect: a novel spect system for nuclear cardiology. *Physics in Medicine Biology*, 54(9):2635, April 2009. ISSN 0031-9155. doi: 10.1088/0031-9155/54/9/003.

Michael Fiechter, Catherine Gebhard, Tobias Fuchs, Jelena Ghadri, Julia Stehli, Egle Kazakauskaite, Bernhard Herzog, Aju Pazhenkottil, Oliver Gaemperli, and Philipp Kaufmann. Cadmium-zinc-telluride myocardial perfusion imaging in obese patients. *Journal of nuclear medicine: official publication, Society of Nuclear Medicine*, 53:1401–6, June 2012. doi: 10.2967/jnumed.111.102434.

Stephan D Fihn, James C Blankenship, Karen P Alexander, John A Bittl, John G Byrne, Benjamin J Fletcher, Gregg C Fonarow, Richard A Lange, Glenn N Levine, Thomas M Maddox, et al. 2014 acc/aha/aats/pcna/scai/sts focused update of the guideline for the diagnosis and management of patients with stable ischemic heart disease. *Journal of the American College of Cardiology*, 64(18):1929–1949, 2014.

Sanjiv S. Gambhir, Daniel S. Berman, Jack Ziffer, Michael Nagler, Martin Sandler, Jim Patton, Brian Hutton, Tali Sharir, Shlomo Ben Haim, and Simona Ben Haim. A novel high-sensitivity rapid-acquisition single-photon cardiac imaging camera. *Journal of Nuclear Medicine*, 50(4):635–643, April 2009. ISSN 0161-5505, 2159-662X. doi: 10.2967/jnumed.108.060020.

Ernest V. Garcia, Tracy L. Faber, and Fabio P. Esteves. Cardiac dedicated ultrafast spect cameras: New designs and clinical implications. *Journal of Nuclear Medicine*, 52(2):210–217, February 2011. ISSN 0161-5505, 2159-662X. doi: 10.2967/jnumed.110.081323.

GE-HealthCare. Nuclear medicine nm / ct 870 dr, 2021. URL `https://www.gehealthcare.com/products/molecular-imaging/nuclear-medicine/nm-ct-870-dr`.

Samantha Green and Jared Grice. Technical note: 3d-printed phantom for dedicated cardiac protocols and geometries in nuclear medicine. *Medical Physics*, 49(2):943–951, 2022. ISSN 2473-4209. doi: 10.1002/mp.15406.

GE HealthCare. Cardiac imaging for molecular imaging | ge healthcare (united states). URL `https://www.gehealthcare.com/products/molecular-imaging/nuclear-medicine/cardiac-imaging`.

Fabien Hyafil, Alessia Gimelli, Riemer H. J. A. Slart, Panagiotis Georgoulias, Christoph Rischpler, Mark Lubberink, Roberto Sciagra, Jan Bucerius, Denis Agostini, and Hein J. Verberne. Eanm procedural guidelines for myocardial perfusion scintigraphy using cardiac-centered gamma cameras. *European Journal of Hybrid Imaging*, 3:11, July 2019. ISSN 2510-3636. doi: 10.1186/s41824-019-0058-2.

Ami E. Iskandrian and Ernest V. Garcia. *Nuclear Cardiac Imaging: Principles and Applications*. Oxford University Press, 2012.

F. Jacobs, H. Thierens, A. Piepsz, K. Bacher, C. Van de Wiele, H. Ham, R. A. Dierckx, and European Association of Nuclear Medicine. Optimised tracer-dependent dosage cards to obtain weight-independent effective doses. *European Journal of Nuclear Medicine and Molecular Imaging*, 32(5):581–588, May 2005. ISSN 1619-7070. doi: 10.1007/s00259-004-1708-5.

S. Jan, G. Santin, D. Strul, S. Staelens, K. Assié, D. Autret, S. Avner, R. Barbier, M. Bardiès, P. M. Bloomfield, D. Brasse, V. Breton, P. Bruyndonckx, I. Buvat, A. F. Chatziioannou, Y. Choi, Y. H. Chung, C. Comtat, D. Donnarieix, L. Ferrer, S. J. Glick, C. J. Groiselle, D. Guez, P.-F. Honore, S. Kerhoas-Cavata, A. S. Kirov, V. Kohli, M. Koole, M. Krieguer, D. J. van der Laan, F. Lamare, G. Largeron, C. Lartizien, D. Lazaro, M. C. Maas, L. Maigne, F. Mayet, F. Melot, C. Merheb, E. Pennacchio, J. Perez, U. Pietrzyk, F. R. Rannou, M. Rey, D. R. Schaart, C. R. Schmidtlein, L. Simon, T. Y. Song, J.-M. Vieira, D. Visvikis, R. Van de Walle, E. Wieërs, and C. Morel. Gate - geant4 application for tomographic emission: a simulation toolkit for pet and spect. *Physics in Medicine and Biology*, 49(19):4543–4561, October 2004. ISSN 0031-9155.

Lisa Jasmat. *A 3D Printed Cardiac Phantom for Nuclear Medicine Imaging*. PhD thesis, The University of Manchester, 2022.

Shiwpursad Jasveer and Xue Jianbin. Comparison of different types of 3d printing technologies. *International Journal of Scientific and Research Publications (IJSRP)*, 8(4), April 2018. ISSN 2250-3153. doi: 10.29322/IJSRP.8.4.2018.p7602.

Kwan Hyeong Jo and Won Jun Kang. Recent progress in myocardial perfusion imaging techniques. *Nuclear Medicine and Molecular Imaging*, March 2024. ISSN 1869-3482. doi: 10.1007/s13139-024-00852-7.

Janos Kiss, Laszlo Balkay, Kornel Kukuts, Marton Miko, Attila Forgacs, Gyorgy Trencsenyi, and Aron K. Krizsan. 3d printed anthropomorphic left ventricular myocardial phantom for nuclear medicine imaging applications. *EJNMMI Physics*, 9(1):34, December 2022. ISSN 2197-7364. doi: 10.1186/s40658-022-00461-3.

Jakub Kočí. Watertight 3d printing pt1: Vases, cups and other open models, April 2021. URL `https://blog.prusa3d.com/watertight-3d-printing-pt1-vases-cups-and-other-open-models_48949/`.

Jakub Kočí. Watertight 3d printing part 2: Airtight closable models (updated 2024), January 2024. URL `https://blog.prusa3d.com/watertight-3d-printing-part-2_53638/`.

M. Lassmann and S. T. Treves. Pediatric radiopharmaceutical administration: Harmonization of the 2007 eanm paediatric dosage card (version 1.5.2008) and the 2010 north america consensus guideline. *Eur J Nucl Med Mol Imaging*, 2014. doi: 10.1007/s00259-014-2731-9.

M. Lassmann, L. Biassoni, M. Monsieurs, C. Franzius, EANM Dosimetry, and Paediatrics Committees. The new eanm paediatric dosage card: additional notes with respect to f-18. *Eur J Nucl Med Mol Imaging*, 35(9):1666–1668, September 2008. doi: 10.1007/s00259-008-0799-9. Erratum in: Eur J Nucl Med Mol Imaging. 2008 Nov;35(11):2141.

Mohamed Mouden, Jorik R. Timmer, Jan Paul Ottervanger, Stoffer Reiffers, Ad H. J. Oostdijk, Siert Knollema, and Pieter L. Jager. Impact of a new ultrafast czt spect camera for myocardial perfusion imaging: fewer equivocal results and lower radiation dose. *European Journal of Nuclear Medicine and Molecular Imaging*, 39(6):1048–1055, June 2012a. ISSN 1619-7089. doi: 10.1007/s00259-012-2086-z.

Mohamed Mouden, Jorik R. Timmer, Jan Paul Ottervanger, Stoffer Reiffers, Ad H. J. Oostdijk, Siert Knollema, and Pieter L. Jager. Impact of a new ultrafast czt spect camera for myocardial perfusion imaging: fewer equivocal results

and lower radiation dose. *European Journal of Nuclear Medicine and Molecular Imaging*, 39(6):1048–1055, June 2012b. ISSN 1619-7089. doi: 10.1007/s00259-012-2086-z.

Jackson O, Connell. How to make waterproof 3d prints, September 2023. URL `https://all3dp.com/2/waterproof-3d-print-pla/`.

Jenny Oddstig, Elin Martinsson, Jonas Jögi, Henrik Engblom, and Cecilia Hindorf. Differences in attenuation pattern in myocardial spect between czt and conventional gamma cameras. *Journal of Nuclear Cardiology*, 26(6):1984–1991, December 2019. ISSN 1532-6551. doi: 10.1007/s12350-018-1296-6.

OpenGATE. Gate - geant4 application for tomographic emission, 2022. URL `http://www.opengatecollaboration.org/`.

Pablo E. Romero, Antonio Agulló, and Esther Molero. *Manufacturing of Watertight Housing for Electronic Equipment by Fused Deposition Modeling*, page 363–376. April 2021. ISBN 978-3-030-68023-7. doi: 10.1007/978-3-030-68024-4_19.

Radiation Protection Commission (RPC). Commission for the protection from ionising and non-ionising radiation. January 2022.

David Sarrut, Mateusz Bała, Manuel Bardiès, Julien Bert, Maxime Chauvin, Konstantinos Chatzipapas, Mathieu Dupont, Ane Etxebeste, Louise M Fanchon, Sébastien Jan, Gunjan Kayal, Assen S Kirov, Paweł Kowalski, Wojciech Krzemien, Joey Labour, Mirjam Lenz, George Loudos, Brahim Mehadji, Laurent Ménard, Christian Morel, Panagiotis Papadimitroulas, Magdalena Rafecas, Julien Salvadori, Daniel Seiter, Mariele Stockhoff, Etienne Testa, Carlotta Trigila, Uwe Pietrzyk, Stefaan Vandenberghe, Marc-Antoine Verdier, Dimitris Visvikis, Karl Ziemons, Milan Zvolský, and Emilie Roncali. Advanced monte carlo simulations of emission tomography imaging systems with gate. *Physics in Medicine and Biology*, 66(10), May 2021. ISSN 1361-6560. doi: 10.1088/1361-6560/abf276.

Takayuki Shibutani, Masahisa Onoguchi, Yuka Naoi, Hiroto Yoneyama, Takahiro Konishi, Ringo Tatami, and Kenichi Nakajima. The usefulness of swiftscan technology for bone scintigraphy using a novel anthropomorphic phantom. *Scientific Reports*, 11(1):2644, 2021.

Piotr Slomka, Guang-Uei Hung, Guido Germano, and Daniel S. Berman. Novel spect technologies and approaches in cardiac imaging. *Cardiovascular innovations and applications*, 2(1):31–46, December 2016. ISSN 2009-8618. doi: 10.15212/CVIA.2016.0052.

Piotr J. Slomka, Daniel S. Berman, and Guido Germano. New cardiac cameras: Single-photon emission ct and pet. *Seminars in Nuclear Medicine*, 44(4):232–251, July 2014. ISSN 0001-2998. doi: 10.1053/j.semnuclmed.2014.04.003.

F Thibault, M Bailly, G Le Rouzic, and G Metrard. Clinical evaluation of general electric new swiftscan solution in bone scintigraphy on nai-camera: a head to head comparison with siemens symbia. *PLoS One*, 14(9):e0222490, 2019.

Hein J. Verberne, Wanda Acampa, Constantinos Anagnostopoulos, Jim Ballinger, Frank Bengel, Pieter De Bondt, Ronny R. Buechel, Alberto Cuocolo, Berthe L. van Eck-Smit, F, Albert Flotats, Marcus Hacker, Cecilia Hindorf, Philip A. Kaufmann, Oliver Lindner, Michael Ljungberg, Markus Lonsdale, Alain Manrique, David Minarik, Arthur J. Scholte, H, A, Riemer H. Slart, J, A, Elin Trägårdh, Tim C. de Wit, and Birger Hesse. Eanm procedural guidelines for radionuclide myocardial perfusion imaging with spect and spect/ct: 2015 revision. *European Journal of Nuclear Medicine and Molecular Imaging*, 42(12):1929–1940, November 2015. ISSN 16197070. doi: 10.1007/s00259-015-3139-x.

Jing Wu and Chi Liu. Recent advances in cardiac spect instrumentation and imaging methods. *Physics in Medicine Biology*, 64(6):06TR01, March 2019. ISSN 0031-9155. doi: 10.1088/1361-6560/ab04de.

Barry L. Zaret and George A. Beller. *Clinical Nuclear Cardiology: State of the Art and Future Directions*. Mosby, 2005.